Exploring Exoplanets' Spectroscopic Secrets: Clues on the Migration and Formation of Hot Jupiters

Thesis by
Danielle Piskorz

In Partial Fulfillment of the Requirements for the
degree of
Doctor of Philosophy

CALIFORNIA INSTITUTE OF TECHNOLOGY
Pasadena, California

2018
Defended 5 September 2017

Danielle Piskorz
ORCID: 0000-0003-4451-2342

ACKNOWLEDGEMENTS

Thanks to my committee members, Professors Heather Knutson, Geoffrey Blake, Yuk Yung, and Lynne Hillenbrand, for their constant mentoring and advice the past five years. Professor Knutson encouraged me to foray into the field of exoplanets as a young graduate student. Professor Blake gave me the opportunity to perform extensive observations on the Keck Telescope and has always been an enthusiastic mentor and scientist. Professors Yung and Hillenbrand have constantly improved my research with their curious questioning. In addition, Professor Michael Line at ASU was a critical collaborator in the final project presented in this dissertation and I thank him for his devotion to planetary science and his support.

None of this research would have been possible without the access to the telescopes on Mauna Kea in Hawaii. The summit of Mauna Kea has always had a very significant cultural role and reverence within the indigenous Hawaiian community. I and countless other astronomers are lucky to have the opportunity to conduct observations from this mountain.

Thanks to everyone who participated in the data collection that made these projects possible. These people (to my knowledge) include Phil Muirhead, Sasha Hinkley, Henry Ngo, Geoff Blake, Alex Lockwood, Masha Kleshcheva, Nate Crockett, Bjorn Benneke, Katherine Kaufman, Ke Zhang, Cam Buzard, and Olivia Wilkins.

Thanks to Professor Lindy Elkins-Tanton, Dr. Suzanne Smrekar, and Professor David Stevenson for nurturing me during my early days as a planetary scientist. The ongoing accomplishments of these three scientists have provided me with inspiration and motivation each and every day.

Thanks to my parents for fostering my love for math and science and encouraging me to look to the stars. Thanks to my fellow graduate students, my kind officemates, and my friends, near and far, for keeping my feet on the ground.

ABSTRACT

Before the mid-90's, scientists' theories for planet formation were finely-tuned to explain the existence of our own Solar System. These theories were thrown into disarray when astronomers began to discover exoplanets, or planets in other solar systems. Forced to reconcile theory with observation, astronomers and planetary scientists have worked together for the past twenty years to solve the puzzles created by these thousands of exoplanets. One particularly intriguing group of newly-discovered planets were the hot Jupiters, planets the size of our Jupiter orbiting their host star every few days. This thesis details two observational campaigns that attempt to illuminate the origin and composition of hot Jupiters. Each project is powered by the NIRSPEC (Near-Infrared SPECtrometer) instrument located at Mauna Kea in Hawaii. The first project aims to determine the stellar multiplicity rate of hot Jupiter host stars. Such a metric can inform the migration histories of these planets. The second project treats a hot Jupiter and its host star as a spectroscopic binary. This treatment reveals the orbital elements and atmospheric composition of the hot Jupiter. The spectroscopic methods described in this thesis are small steps in the study of hot Jupiters and ultimately potentially habitable exoplanets.

PUBLISHED CONTENT AND CONTRIBUTIONS

Piskorz, D., B. Benneke, N. Crockett, et al. (2017a). *The Astronomical Journal* **154**.2, 78–86. DOI: 10.3847/1538-3881/aa7dd8.
D.P, B.B., N.R.C., A.C.L., and G.A.B. participated in the data collection. D.P. led the data reduction and analysis and wrote the manuscript. B.B. provided atmospheric models.

Piskorz, D., M. Line, H. Knutson, et al. (2017b). *Submitted to The Astronomical Journal*.
D.P, B.B., and G.A.B. participated in the NIRSPEC data collection. D.P. led the NIRSPEC data reduction, analyzed all the data, and wrote the manuscript. M.R.L provided atmospheric models. H.K. reduced the eclipse data procured by D.D.'s Spitzer program.

Piskorz, D., B. Benneke, N. Crockett, et al. (2016). *The Astrophysical Journal* **832**.2, 131–139. DOI: 0004-637X/832/2/131.
D.P., B.B., N.R.C, A.C.L, and G.A.B were involved in the data acquisition for this project. D.P. led the data reduction and analysis and wrote the manuscript. B.B. and T.S.B. provided atmospheric models. N.R.C. contributed to the initial code base. M.B. analyzed the radial velocity data.

Piskorz, D., H. Knutson, H. Ngo, et al. (2015). *The Astrophysical Journal* **814**.2, 148–161. DOI: 10.1088/0004-637X/814/2/148.
D.P and P.S.M were involved in the data acquisition. D.P. led the data reduction and analysis and wrote the manuscript. H.A.K. conceived the project.

TABLE OF CONTENTS

LIST OF ILLUSTRATIONS

Number *Page*

LIST OF TABLES

Chapter 1

INTRODUCTION

1.1 Introduction to Hot Jupiters

Before the mid-90's, scientists' theories for planet formation were finely-tuned to explain the existence of our own solar system. Our solar system consists of rocky planets, gas giants, and ice giants, all on nearly circular orbits in roughly the same plane. Over time, the theories developed to explain planet formation were tuned to predict the properties of our particular solar system. Planets form out of a protoplanetary disk consisting of gas and dust, leftovers from star formation. A core tenet of planet formation theories was that Jupiter must have formed far out in the protoplanetary disk. Whether the planet formed by core accretion (build a solid core first and then gather gas from the disk as in Rice & Armitage 2003) or by disk instability (the surface density of the gas in the disk is so high that the gas collapses into a planet under its own weight as in Boss 1997), only at large separations from the central star is there enough material for a gas giant to form.

These theories were thrown into disarray when astronomers began to discover exoplanets, or planets in other solar systems (Figure 1.1). Two of the most popular techniques for finding exoplanets are the transit and radial velocity techniques. The transit method detects a planet as it passes in front of its star and we observe an overall dimming of the star's light. This method provides information on the planet's size, period, and (with a few adjustments) atmospheric composition. The radial velocity method measures the gravitational tug of a planet on its host star. This method provides information on the planet's period and indicative mass ($M \sin i$). Other methods of exoplanet detection are microlensing and direct imaging.

One particularly intriguing group of newly-discovered planets is hot Jupiters, planets the size of our Jupiter orbiting their host star every few days. These planets are found orbiting approximately 1% of Sun-like stars (Wright et al. 2012) and have no direct analog in our solar system. Theories suggest that hot Jupiters may formed at their present locations (e.g., Batygin 2016), or they may have formed elsewhere in the protoplanetary disk and migrated inwards through a variety of mechanisms (e.g., Lin et al. 1996, Pollack et al. 1996, Goldreich & Tremaine 1980).

Forced to reconcile theory with observation, astronomers and planetary scientists

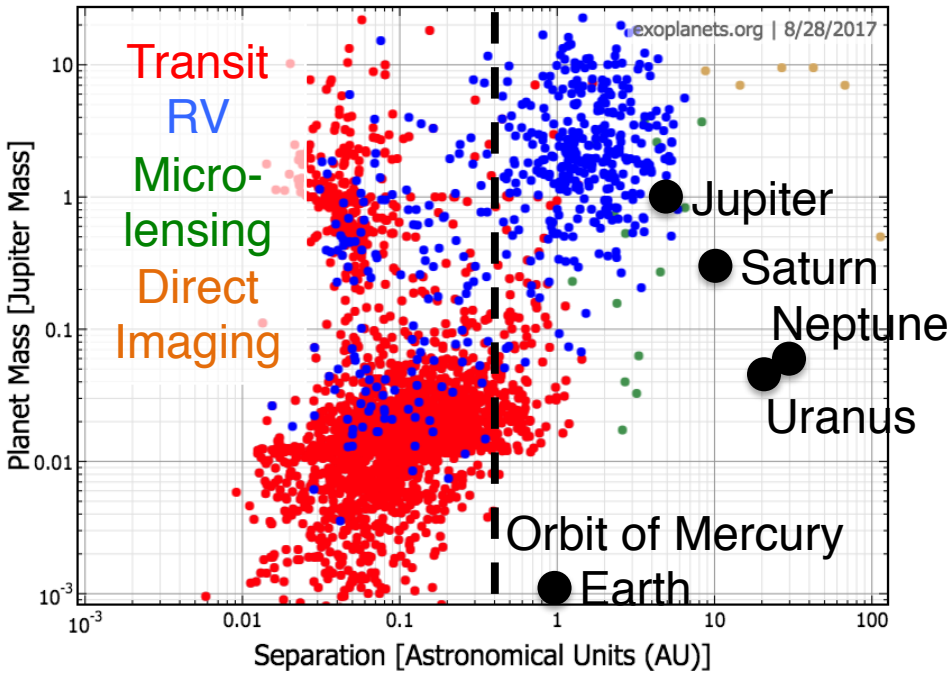

Figure 1.1: Plot of known exoplanets detected with four methods (Han et al. 2014). Solar system planets and the separation (i.e., semi-major axis) of Mercury's orbit are marked. Separation is the distance between the host star and the planet measured in astronomical units (1 AU is the distance from the Sun to the Earth).

have worked together for the past twenty years to answer the questions posed by the variety of exoplanetary systems. This thesis asks, "How did hot Jupiters migrate to their present locations?" and "Where in the protoplanetary disk do hot Jupiters form?" Two observational campaigns attempt to answer these questions and illuminate the origin and composition of hot Jupiters. The first question is addressed by the Friends of Hot Jupiters project described in Chapter 2. The second question is addressed by the Detect Detection program, described in Chapter 3 and applied to four exoplanet systems in Chapters 4, 5, and 6. Each project is powered by the NIRSPEC (Near-Infrared SPECtrometer) instrument located at Mauna Kea in Hawaii (McLean et al. 1990).

1.2 Investigation of Hot Jupiter Migration

The first project tries to respond to, "How did hot Jupiters migrate to their present locations?" by determining the stellar multiplicity rate for hot Jupiter host stars. Such a metric can inform the migration histories of these planets (e.g., a preference for three-body dynamics or planet-disk interactions). Surveys of nearby field stars indicate that stellar binaries are common, yet little is known about the effects that

these companions may have on planet formation and evolution. Notably, binary star systems are often excluded from the search for exoplanets. Therefore, a concerted effort to detect hidden binary companions to exoplanet host stars is critical.

The Friends of Hot Jupiters project uses three complementary techniques to search for stellar companions to known hot Jupiter-hosting stars: radial velocity monitoring (Knutson et al. 2014), adaptive optics imaging (Ngo et al. 2015), and near-infrared spectroscopy (Chapter 2). The radial velocity monitoring portion of the survey searched for long-term radial velocity trends in hot Jupiter systems, indicating the presence of a planetary or stellar mass companion out to 50 AU. The adaptive optics imaging portion of the survey produced images of hot Jupiter host stars and hidden stellar companions at separations between 50 and 2000 AU. This means there is a small gap in semi-major axis that is not surveyed. Radial velocity monitoring and adaptive optics imaging together are blind to hidden companions too distant to cause a radial velocity signature or too dim to be seen in adaptive optics images.

In Chapter 2, we use NIRESPEC to search for hidden companions where radial velocity monitoring and adaptive optics imaging cannot. Limited by NIRSPEC's slit width, we are sensitive to hidden companions within 200 AU of the hot Jupiter host star. We examine high-resolution K band infrared spectra of fifty stars hosting gas giant planets on short-period orbits. We use spectral fitting to search for blended lines due to the presence of cool stellar companions in the spectra of our target stars, where we are sensitive to companions with temperatures between 3500-5000 K. We identify eight systems with candidate low-mass companions, including one companion that was independently detected in our AO imaging survey. For systems with radial velocity accelerations, a spectroscopic non-detection rules out scenarios involving a stellar companion in a high inclination orbit.

We use these data to place an upper limit on the stellar binary fraction at small projected separations, and show that the observed population of candidate companions is consistent with that of field stars and also with the population of wide-separation companions detected in our previous AO survey. We find no evidence that spectroscopic stellar companions are preferentially located in systems with short-period gas giant planets on eccentric and/or misaligned orbits.

1.3 Investigation of Hot Jupiter Formation

The second project tackles the question, "Where in the protoplanetary disk do hot Jupiters form?" Measurements of the compositions of hot Jupiter atmospheres can

be used as probes of their formation histories. If hot Jupiters are formed via core accretion, whereby first a solid core forms, then gas accretes, and the core grows into a gas giant planet (Rice & Armitage, 2003), and if the C/O ratio of the protoplanetary disk varies with semi-major axis (Oberg et al., 2001), then a hot Jupiter's modern-day C/O ratio should be a rough indicator of where it originally formed in the protoplanetary disk. For this case, the C/O ratio of the hot Jupiter should be distinct from that of the host star. However, if solids were incorporated into the hot Jupiter's atmosphere later in planet formation, the C/O ratios of the hot Jupiter and the host star may be similar. Furthermore, a measurement of C/O high in the atmosphere of a hot Jupiter should give a reliable measurement of bulk C/O.

As a community, astronomers have become extremely adept at detecting transiting planets and measuring their atmospheric compositions. However, by virtue of geometry, most planets do not transit. In fact, as the community searches for habitable zone planets orbit Sun-like stars at larger orbital separations, it becomes increasingly unlikely that these planets will transit.

Therefore, we target the thermal emission spectrum of the non-transiting gas giants with high-resolution near-infrared spectroscopy, by treating the planet and its host star as a spectroscopic binary. For sufficiently deep summed flux observations of the star and planet across multiple epochs, it is possible to resolve the signal of the hot gas giant's atmosphere compared to the brighter stellar spectrum, at a level consistent with the aggregate shot noise of the full data set. To do this, we first perform a principal component analysis to remove the contribution of the Earth's atmosphere to the observed spectra. Then, we use a cross-correlation analysis to tease out the spectra of the host star and the hot Jupiter. In this way, we determine the hot Jupiters orbit and identify key sources of atmospheric opacity. The details of our methods are given in Chapter 3.

Based on an analysis of the maximum likelihood curves calculated from the multi-epoch cross correlation of the full data set with atmospheric models, we report the radial projection of their Keplerian orbital velocities, their true masses, their inclinations, and atmospheric opacities in the infrared for four hot Jupiters.

First, we reproduce the direct detection of tau Boo b's atmosphere reported in Lockwood et al. 2014 (and others) in Chapter 4. Next, we test the brightness limits of the technique and develop a more rigorous orbital model in Chapter 4 where we report the direct detection of HD 88133 b. In Chapter 5, we apply the direct detection method to hot Jupiter ups And b. ups And b is the innermost planet of a

multi-planetary system consisting of two other massive giant planets packed within 5 AU. Measurements of ups And b's orbital elements provides useful context for dynamicists wishing to elucidate the particular origin and evolution of this system. Finally, we detect the emission spectrum of a transiting exoplanet and compare our results to Spitzer secondary eclipse data (KELT-2Ab in Chapter 6). The KELT-2Ab analysis again confirms the effectiveness of the direct detection method and highlights its ability to provide useful information on the composition of a hot Jupiter's atmosphere.

By developing a new observational method of determining the orbital elements and atmospheric compositions of non-transiting hot Jupiters, we may one day be able to precisely measure the C/O ratio of hot Jupiter atmospheres and learn where in the protoplanetary disk they formed.

1.4 The NIRSPEC Instrument

NIRSPEC has been the main workhorse of this thesis, and will continue to contribute to these research avenues after it is upgraded in 2018 (McLean et al., 1998; Martin et al. 2014). Incoming starlight captured by the 10-m telescope aperture is focused onto a 0.432"x24" slit. A rotator maintains that star's position on the slit as the telescope tracks the target star through the night sky. The collimated starlight is then directed to an echelle grating having a steep blaze angle and high blaze density. The echelle produces high dispersion, but presents a serious order overlap problem. As a solution, the light is directed to a cross-disperser which separates the echelle spectrogram in a direction perpendicular to the echelle direction. With a specific choice of echelle and cross-disperser parameters, a large wavelength range can be recorded onto the detector at high resolution: R=25,000 in the L band (3.0 - 3.4 μm) and R=30,000 in the K band (2.0 - 2.4 μm).

1.5 References

Batygin, K., Bodenheimer, P.H., & Laughlin, G.P. 2016, ApJ, 829, 2

Boss, A.P. 1997, Science, 276, 5320

Goldreich, P., & Tremaine, S. 1980, ApJ, 241, 425

Han, E., Wang, S.X., Wright, J.T. et al. 2014, PASP, 126, 943

Knutson, H. A., B. J. Fulton, B. T. Montet et al. 2014, ApJ, 785, 126

Lin, D. N. C., Bodenheimer, P., & Richardson, D. C. 1996, Nature, 380, 606

Lockwood, A.C., Johnson, J.A., Bender, C.F., et al. 2014, ApJ, 783, L29

Martin, E.C., Fitzgerald, M.P., McLean, I.S. et al. 2014, Proc. SPIE 9147

McLean, I. S., Becklin, E. E., Bendiksen, O., et al. 1998, Proc. SPIE 3354, 566

Ngo H., H. A. Knutson, S. Hinkley, et al. 2015, ApJ, 800, 138

Oberg, K.I., Murray-Clay, R., & Bergin, E.A. 2011, ApJ, 678, 498

Pollack, J. , B., O. Hubickyk, P. Bodenheimer, et al. 1996, Icarus, 124, 1.

Rice & Armitage. 2003, ApJ, 598, 1

Wright, J.T., Marcy, G.W., Howard, A.W. et al. 2012, ApJ, 753, 2

Chapter 2

FRIENDS OF HOT JUPITERS: A NEAR-INFRARED SPECTROSCOPIC SURVEY

This chapter is adapted from work previously published as

Piskorz, D., H. Knutson, H. Ngo, et al. (2015). *The Astrophysical Journal* **814**.2, 148–161. DOI: 10.1088/0004-637X/814/2/148.

2.1 Introduction

Approximately 1% of nearby Sun-like stars host short-period gas giant planets, known as “hot Jupiters" (Wright et al. 2012). Standard models of planet formation suggest that hot Jupiters are unlikely to have formed in situ, but must have formed beyond the ice line and migrated inward (Lin et al. 1996, Pollack et al. 1996). In this scenario, proposed migration models include both planet-disk (type II) interactions (Goldreich & Tremaine 1980; Kley & Nelson 2012) and dynamical models including Kozai migration (Malmberg et al. 2007; Fabrycky & Tremaine 2007; Naoz et al. 2011), planet-planet scattering (Nagasawa et al. 2008; Beauge & Nesvorny 2012), and secular chaos (Wu & Lithwick 2010). While disk-driven migration is controlled primarily by local interactions, dynamical migration processes can be strongly affected by the presence of distant massive companions. In particular, the simplest variant of Kozai migration requires a perturbing star (Wu & Murray 2003), while planet-planet scattering can in principle be triggered by external perturbations (Batygin et al. 2011). By studying the present-day properties of hot Jupiter systems, we can distinguish between competing formation and migration channels.

We generally expect that in isolation disk migration should produce hot Jupiters on circular and well-aligned orbits, while dynamical migration simulations frequently result in planets with orbits that are eccentric and/or misaligned with respect to the star’s spin axis. Surveys of hot Jupiter spin-orbit alignments indicate that approximately half of all hot Jupiter systems are misaligned (Winn et al. 2010; Triaud et al. 2010, Albrecht et al. 2012), suggesting that three-body dynamics may play an important role in these systems. On the other hand, the apparent paucity of high eccentricity gas giant planets at intermediate orbital periods suggest that less than half of all hot Jupiters could have migrated via the star-planet Kozai-

Lidov mechanism (Dawson et al. 2013). Alternatively, the presence of a stellar companion can also tilt the protoplanetary disk with respect to the stellar rotation axis, causing spin-orbit misalignments before planets have even formed (Batygin 2012; Spalding & Batygin 2014). Regardless of whether it is the disk or the planet orbit being tilted, both scenarios require the presence of a massive outer companion on a non-coplanar orbit (albeit in different epochs) in order to explain the present-day spin-orbit misalignments observed in a significant fraction of hot Jupiter systems.

Although a majority of the extrasolar planets detected to date appear to orbit single stars, this is somewhat surprising as surveys of field stars indicate that approximately half of all Sun-like stars in the solar neighborhood are found in binaries (Duquennoy & Mayor 1991; Raghavan et al. 2010). It is unclear exactly what role a binary companion might play in the process of planet formation and migration. It has been suggested that wide separation binaries may warp or even truncate the outer edges of the protoplanetary disk and reduce average disk lifetimes (e.g., Terquem & Bertout 1993; Pichardo et al. 2005; Kraus et al. 2012; Cheetham et al. 2015). Dynamical interactions with a distant companion may increase turbulent velocities in the protoplanetary disk, thereby preventing materials from condensing (Mayer et al. 2015). By searching for stellar companions to known planetary systems we can constrain their potential effects on these planetary systems, albeit with the caveat that close encounters between stars forming in crowded cluster environments may have similar effects (e.g., Bonnell et al. 2001; Spurzem et al. 2009; Hao et al. 2013; Zheng et al. 2015).

Previous surveys have identified a number of stellar companions in known planetary systems (Eggenberger et al. 2007; Raghavan et al. 2010; Wang et al. 2014a), but only a handful are close binaries with hot Jupiters orbiting the primary star. The *Kepler* mission has detected approximately a dozen circumbinary planets to date (e.g., Doyle et al. 2011; Welsh et al. 2012) and a number of adaptive optics (AO) surveys have proven to be effective at detecting more widely separated stellar companions (Wang et al. 2015; Woellert et al. 2015; Woellert & Brandner 2015; see Ngo et al. 2015 for a complete review of surveys prior to 2015). The Friends of Hot Jupiters (FOHJ) project systematically tests the validity of dynamical models of hot Jupiter migration and performs a dedicated inquest on the stellar multiplicity rate of hot Jupiter systems. We focus on a sample of nearby transiting hot Jupiters with well-characterized spin-orbit alignments and orbital eccentricities, divided into a control group with circular, well-aligned orbits, and an experimental group with

eccentric and/or misaligned orbits. Our approach differs from that of most previous surveys, which typically focused on either non-transiting planets or transiting planet candidates in the *Kepler* sample, of which the vast majority are too small or too faint to detect the Rossiter-McLaughlin effect and measure their corresponding spin-orbit misalignments (e.g., Lillo-Box 2012; Adams et al. 2012).

In Knutson et al. (2014) we searched for long-term radial velocity accelerations due to distant planetary or stellar companions in these systems, and found that 51±10% of the stars in our sample hosted planetary mass companions with orbits between 1-20 AU. In Bechter et al. (2014) and Ngo et al. (2015) we performed a complementary *K* band AO imaging search for stellar companions on relatively wide orbits, and found a binary rate of 48±9% for stellar companions with projected separations between 50-2000 AU. This rate is approximately twice that of field stars having companions in this semi-major axis range (Raghavan et al. 2010), suggesting that stellar companions may play a role in the formation of these systems. Although previous imaging studies hinted at a high stellar multiplicity rate for transiting planet host stars (see Ngo et al. 2015 for a complete review), our study was the first to confirm that the imaged companions were gravitationally bound and to derive a completeness-corrected multiplicity rate for hot Jupiter host stars. In both surveys there was no indication that eccentric or misaligned systems were more likely to have a massive outer companion than their circular and well-aligned counterparts.

In this study, we use Keck NIRSPEC (Near InfraRed Echelle SPECtrograph; McLean et al. 1998) to search for stellar companions that might have gone undetected in our AO and radial velocity observations. We use high-resolution *K* band spectroscopy to search for blended lines from cool stellar companions, exploiting the deep CO molecular absorption features present in cool stars and distinct from the lines of the hotter primaries. We expect that these companions will have relatively small projected separations and/or high orbital inclinations, in order to be consistent with our previous radial velocity and AO observations of these systems. For systems in which we detect companions, we can estimate their effective temperatures and place an upper limit on their projected separations from the primary.

A number of previous studies have used high-resolution spectroscopy to locate hidden binary companions. Bardalez Gagliuffi et al. (2014) analyzed a sample of 815 M and L dwarf spectra taken with IRTF SpeX in order to locate blended stellar companions with relatively low effective temperatures (also see Burgasser et al. 2010a). Guenther et al. (2013) used VLT CRIRES to identify approximately

twenty planet-hosting stars in the *CoRoT* sample with blended spectra from close stellar companions. Kolbl et al. (2015) observed planet-hosting stars from the *Kepler* survey with optical Keck HIRES spectroscopy in order to search for binary companions having relative radial velocities greater than 10 km/s such that the secondary absorption lines are Doppler shifted. A similar technique is used to probe absorption lines in the atmospheres of hot Jupiters, which exhibit rapidly varying velocity offsets (Snellen et al. 2010; de Mooij et al. 2012; Birkby et al. 2013; Lockwood et al. 2014). For cases where the hidden companion has a significantly different effective temperature than the target star, Kolbl et al. (2015) were also able to detect companions with smaller radial velocity offsets. Of the 1160 *Kepler* stars with candidate transiting planets, sixty-three showed spectroscopic evidence for a companion star. We use a similar approach in our survey, but observe in the infrared in order to increase our sensitivity to relatively cool stellar companions.

In Section 2 we present a description of our observations and subsequent model fitting, and in Section 3 we discuss the resulting spectroscopic detections. In Section 4 we compare our results to those of the adaptive optics and radial velocity portions of the Friends of Hot Jupiters survey. In Section 5 we compute the companion fraction for our sample.

2.2 Observations and Data Analysis

We observed fifty short-period transiting gas giant planetary systems on four separate nights (UT August 27 2012, January 28 2013, March 2 2013, and July 4 2013) using NIRSPEC at the W.M. Keck Observatory on Mauna Kea, which has a resolution R = 30,000 in the K band (2.0-2.4 microns). See Knutson et al. (2014) for details on the sample selection. We extract one-dimensional spectra from the raw images using an IDL (Interactive Data Language) pipeline that flat fields and dark subtracts the images as well as removes any bad pixels following the methods described in Boogert et al. (2002). We correct for telluric absorption by dividing the science target spectrum by that of a calibrator star with an intrinsically flat spectrum, usually a nearby rapidly-rotating A-star, at a similar air mass on the same night, where we have empirically shifted the calibrator spectrum to match the wavelength solution of each target star. As an example, the telluric-corrected and wavelength-calibrated spectrum for WASP-2 taken on UT July 4 2013 is shown in Figure 2.1.

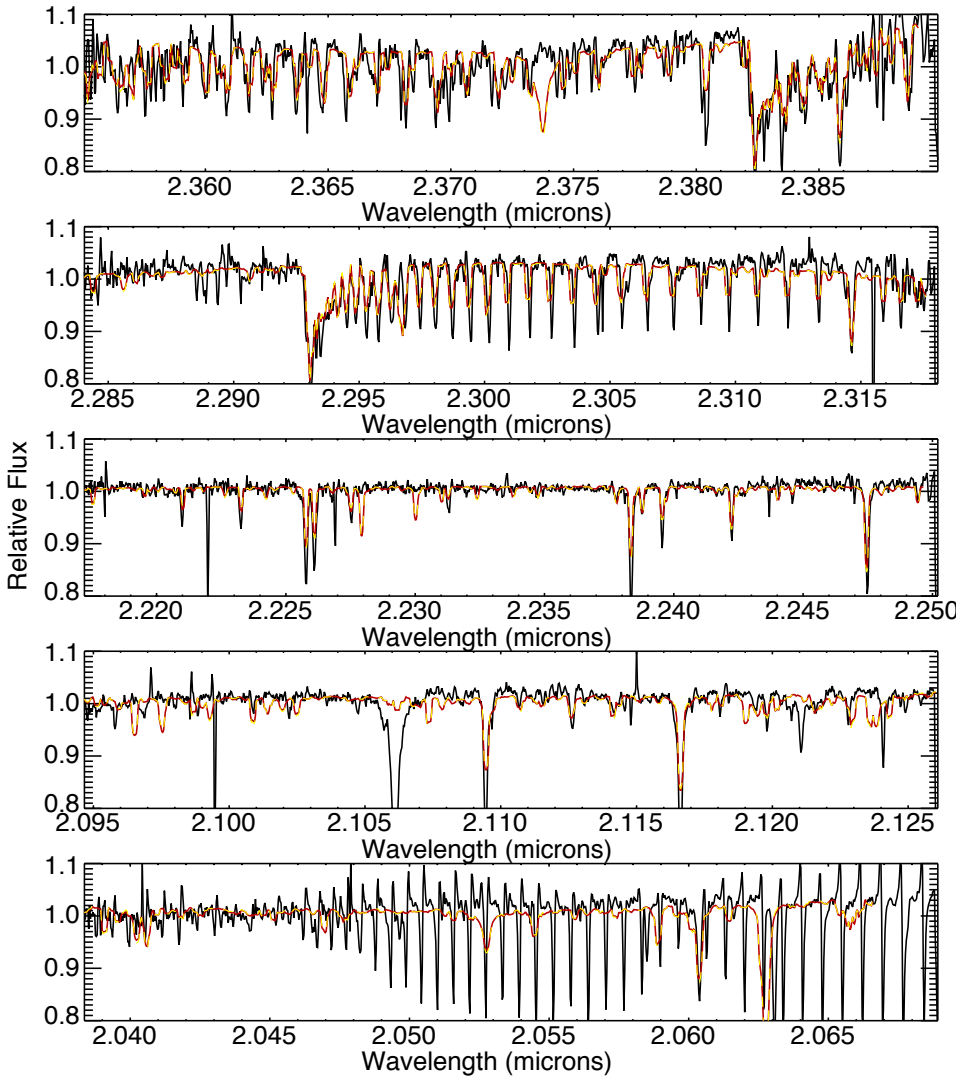

Figure 2.1: Telluric-corrected and wavelength-calibrated K band spectrum for WASP-2 taken with NIRSPEC on UT July 4 2013 shown in black with the best-fit one-star model overplotted with a yellow dashed line and the best-fit two-star model overplotted with a red solid line. “Chirps" in the data, especially from 2.040-2.065 μm, are due to incomplete telluric removal.

One-Star Model

We fit each K band spectrum with a PHOENIX stellar model (Husser et al. (2013) interpolated to match the published effective temperature $T_{\rm eff}$, surface gravity $\log(g)$, and metallicity [Fe/H] of the target star. See Table 2.1 for a list of targets and their stellar properties. In accordance with Gray (2005), the synthetic spectrum is

rotationally broadened by convolving it with the following kernel:

$$G(\Delta\lambda) = \frac{2(1-\epsilon)\left(1-\Delta\lambda^2\right)^{1/2} + \frac{1}{2}\pi\epsilon\left(1-\Delta\lambda^2\right)}{\pi c\left(1-\frac{\epsilon}{3}\right)}, \tag{2.1}$$

where $\Delta\lambda = \frac{\lambda v \sin i}{c}$, $v \sin i$ is the line-of-sight rotational velocity as listed in Table 2.1, and ϵ is the limb darkening coefficient of the target taken from Claret (2000).

Note that in Table 2.1, distances are estimated from stellar models. All ϵ values are from Claret (2000). All $\log R_{HK}$ values are from Knutson et al. (2010). WASP-12 was in the original Friends of Hot Jupiter sample, but eliminated from the NIRSPEC survey because of its low elevation at the time of observation.

Two-Star Model

We construct a two-star model by combining the rotationally-broadened PHOENIX model appropriate for the target star with another PHOENIX model corresponding to a faint cool companion in the system. For each target, we create 34 two-star models, each with a different companion effective temperature ranging from 2300 to 5500 K. We assume all our companion stars have $\log(g) = 5.00$. We also assume our companion stars have the same radial veolcities as the primary stars because companions in short-period orbits would already have been detected in our radial velocity observations of the primary star. For example, a K-dwarf companion to a typical star in our survey with a random orbital orientation must on average be located beyond 10 AU in order to avoid creating a detectable RV signal. At this separation, the companion star would have a RV offset of 6 km/s, corresponding to 0.4 pixels in our NIRSPEC observations. This choice represents a departure from traditional spectroscopic binary analyses (e.g., Zucker & Mazeh 1994), which allow for an arbitrary radial velocity offset between the two binary components. Although our decision to fix the radial velocity offset between the two stars to zero precludes us from detecting chance blends with unassociated background or foreground stars, we note that such blends would need to have a differential magnitude less than 5.0 in order to be detectable and a separation of less than 0.4" in order to fall within our slit. In our AO survey of these stars we found that all candidate stellar companions with a differential K band magnitude less than 6.0 located within 5" of the primary were in fact bound companions (see Fig. 4 in Ngo et al. 2015), and we therefore consider it unlikely that any chance blends would occur in our sample that meet the above criteria.

We set [Fe/H] = 0 for our companion stars as the primary stars in these systems all

Target Star	R ($R_\odot$)	$T_{\rm eff}$(K)	D (pc)	log$g$	[Fe/H]	$v \sin i$(km/s)	ϵ	$\log(R'_{\rm HK})$	Refs.
GJ 436	0.45	3416	10.14	4.83	-0.03	3.0	0.3063	-5.298	1, 2, 3, 4
HAT-P-2	1.64	6411	125.3	4.16	0.14	20.8	0.2828	-4.7	5, 6
HAT-P-4	1.46	5890	293.5	4.14	0.2	5.6	0.2697	-5.082	5, 7, 8
HAT-P-6	1.46	6687	277.8	4.22	-0.11	8.9	0.2556	-4.799	5, 9
HAT-P-7	1.90	6259	320	4.02	0.15	5	0.2900	-5.018	5, 10, 11
HAT-P-8	1.48	6223	230	4.19	-0.04	12.6	0.2917	-4.985	5, 12, 13
HAT-P-10	0.79	4974	121.7	4.56	0.25	1.9	0.3613	-4.823	5, 14
HAT-P-11	0.75	4792	38.0	4.59	0.33	0.8	0.3789	-4.567	5,15
HAT-P-12	0.70	4650	139.1	4.61	-0.29	0.5	0.3932	-5.104	16
HAT-P-13	1.76	5720	214	4.13	0.46	3.1	0.3117	-5.138	5, 14, 17
HAT-P-14	1.59	6671	205	4.25	0.07	9.0	0.2714	-4.855	5, 17, 18
HAT-P-15	1.08	5640	190	4.38	0.31	2.1	0.3229	-4.977	5, 19
HAT-P-16	1.24	6140	235	4.34	0.12	3.4	0.2958	-4.863	5, 20
HAT-P-17	0.84	5345	90	4.53	0.06	1.3	0.3349	-5.043	5, 21
HAT-P-18	0.75	4790	166	4.56	0.14	0.8	0.3789	-4.799	5, 22
HAT-P-20	0.70	4619	70	4.64	0.26	2.6	0.3932	-4.506	5, 23
HAT-P-22	1.04	5367	82	4.37	0.29	1.5	0.3349	-4.901	5, 23
HAT-P-24	1.32	6329	396	4.27	-0.21	11.4	0.2871	-4.955	5, 24
HAT-P-26	0.79	5142	134	4.56	0.1	1.4	0.3478	-5.008	5, 22
HAT-P-29	1.22	6086	322	4.34	0.14	4.4	0.2982	-5.096	5, 25
HAT-P-30	1.22	6304	193	4.36	0.13	2.2	0.2882	5.169	26
HAT-P-31	1.36	6065	354	4.26	0.15	0.5	0.2992	5.169	27
HAT-P-32	1.22	6207	283	4.33	-0.04	20.7	0.2927	-4.641	22
HAT-P-33	1.64	6446	387	4.15	0.07	13.7	0.2812	-4.87	22
HAT-P-34	1.56	6442	257	3.98	0.21	24.5	0.2814	-4.931	28
HD 149026	1.53	6103	80.8	4.27	0.24	6.3	0.2975	-5.03	5, 29
TrES-2	0.95	5850	220	4.47	-0.01	0.8	0.3114	-4.949	5, 30, 31
TrES-3	0.83	5514	258.5	4.57	-0.2	1.3	0.3229	-4.549	5, 32
TrES-4	1.83	6200	476	4.05	0.14	8.5	0.2928	-5.104	32
WASP-1	1.50	6160	380	4.21	0.14	1.7	0.2947	-5.114	5, 17
WASP-2	1.06	5255	140	4.52	0.06	1.9	0.3478	-5.054	5, 17, 33
WASP-3	1.21	6375	220	4.28	-0.06	15.4	0.2850	-4.872	5, 34, 35
WASP-4	0.90	5540	280.9	4.47	0	3.4	0.3229	-4.85	5, 36, 37
WASP-7	1.32	6520	140	4.32	0	18.1	0.2783	-4.8	37, 38
WASP-8	1.05	5570	87	4.40	0.17	2.7	0.3114	-4.709	37, 39
WASP-10	0.70	4735	90	4.51	0.05	2.9	0.3789	-4.704	5, 40, 41
WASP-14	1.67	6462	160	4.29	-0.13	3.5	0.2810	-4.923	5, 17, 42
WASP-15	1.52	6405	256	4.40	0	4.9	0.2836	-5.286	37, 43
WASP-16	1.09	5630	174	4.21	0.07	2.5	0.3233	-5.048	37, 43
WASP-17	1.58	6550	476	4.14	-0.02	9.8	0.2763	-5.331	5, 17, 37, 44
WASP-18	1.29	6368	122.6	4.37	0.11	10.9	0.2853	-5.43	5, 37, 38
WASP-19	1.02	5460	250	4.50	0.05	4.5	0.3349	-4.66	45
WASP-22	1.22	5958	300	4.50	0.05	4.5	0.3041	-5.065	45
WASP-24	1.33	6107	332.5	4.26	-0.02	6.1	0.2973	-5.139	5, 46
WASP-34	0.93	5700	120	4.50	-0.02	1.4	0.3114	-5.163	47
WASP-38	1.35	6187	110	4.25	-0.02	8.6	0.2936	-5.158	5, 48
XO-2	0.97	5377	156.0	4.45	0.35	1.0	0.3349	-4.988	5, 49
XO-3	1.38	6759	185.7	4.24	-0.05	20.3	0.2664	-4.595	5, 50, 51
XO-4	1.56	6297	308.2	4.17	-0.03	8.8	0.2882	-5.292	5, 52
XO-5	1.08	5370	260	4.31	0.05	0.7	0.3349	-5.147	11

Table 2.1: Target List and Stellar Properties

have near-solar or solar metallicities. The exact value of metallicity generally affects the depth of the absorption features. We evaluate the magnitude of this effect on our models by re-running our fits to the most metal-rich star in our sample (HAT-P-13, [Fe/H] = 0.46 ± 0.07), and find that our results are indistinguishable from those of stellar metallicity models. Since cool stars typically have $v \sin i$ values less than 5 km/s, instrumental broadening will dominate and we fix the rotational broadening to zero for our cool star companion models. PHOENIX models are given in units of flux per unit surface area, and we multiply the spectra of the primary and companion stars by their respective areas in order to convert to total flux. We take the value for the radius of the primary star from the published literature, and we calculate the radius of the companion as a function of its effective temperature using the stellar evolution models of Baraffe et al. (2003).

Fitting Procedure and Detection Metric

We first fit the one-star model to the calibrated data, assuming constant errors at each wavelength bin. The wavelength solution (described to third order as $\lambda = ax^2 + bx + c$ where x is pixel number and a, b, and c are free parameters) and the width of the instrumental broadening kernel are left as free parameters when fitting each individual spectrum. We allow the instrumental broadening to vary across all orders and find that it remains roughly consistent throughout (full-width half-maximum ~ 0.05 cm^{-1}). The instrumental broadening kernel is assumed to be Gaussian and represents the effect of poor seeing and the interaction of the starlight with the instrumental apparatus. The instrumental broadening varies from target to target according to the orientation of the telescope and the air mass of the observations. We find the best-fit model by minimizing χ^2 and check that we have found the correct global minimum by repeating the calculation with different initial guesses in the parameter space.

We then use the best-fit one-star model to determine empirical error bars for the data. These error bars are calculated as the standard deviation of each residual and its twenty nearest neighbors. This method of error calculation allows us to directly estimate the combined error due to the calibration, model fit, and photon noise contributions, many of which are difficult to predict a priori. We note that these empirically determined error values are only an approximation to the true error distribution; our use of the χ^2 metric implicitly assumes that each wavelength measurement is drawn from an independent Gaussian distribution with a width σ determined by our empirical estimates. This is fundamentally an approximation and

we therefore use the χ^2 values from our fits as a metric of relative goodness-of-fit rather than an absolute measurement of the probability of a given model. With these new error bars, we refit the best-fit one-star model at the best-fitting grid point. We use the final best-fit parameters for the one-star model as the initial guess for fitting the two-star model. Although we allow the instrumental broadening and wavelength solution to vary between the one and two-star models, we find consistent values between the two versions of the fit. We exclude the third order (2.155-2.185 μm) from our analysis, where we find that our telluric A star standards have a strong Brackett gamma absorption line that propagates into our target spectra when applying our telluric correction.

We plot the reduced chi-squared $\left(\chi^2_{red}\right)$ value for the two-star fit as a function of the stellar companion temperature and look for minima indicating the presence of a cool companion. The χ^2_{red} for the coolest stellar companions approaches that of the single-star fit, indicating that we are not sensitive to companions below a certain temperature, as shown in panels A-C of Figure 2.2.

We also compare the one- and two-star fits using the Bayesian Information Criterion (BIC), which is defined as

$$\mathrm{BIC} = \chi^2 + N\ln(n), \tag{2.2}$$

where χ^2 is the canonical chi-squared value, N is the number of free parameters, and n is the number of data points. For our purposes, N=4 for the one-star model, N=5 for the two-star model, and n = 4980. In order to be classified as a detection, there must be a significant improvement in the χ^2_{red} and in the BIC for the two-star model, and we must be able to verify the presence of absorption lines from the cool companion that are distinct from those of the primary (i.e., the code is not just improving the fit to a single star spectrum by overlaying a second nearly identical spectrum and better fitting to the measured line profiles). We find that in all cases the BIC gives results that are equivalent to the χ^2_{red} approach. For the systems where we detect candidate stellar companions, we list the effective temperature of the cool companion that produces the largest improvement in χ^2_{red} over the one-star model. In some cases there is a broad minimum in χ^2_{red} for the two-star model centered on the effective temperature of the primary, which can create a slope that extends out to relatively low companion temperatures. We correct for the effect of this slope in cases where we detect a candidate stellar companion at lower temperatures by interpolating the slope across the region spanned by the minimum due to the companion and subtracting the interpolated trend. The endpoints for this interpolated line are chosen by finding

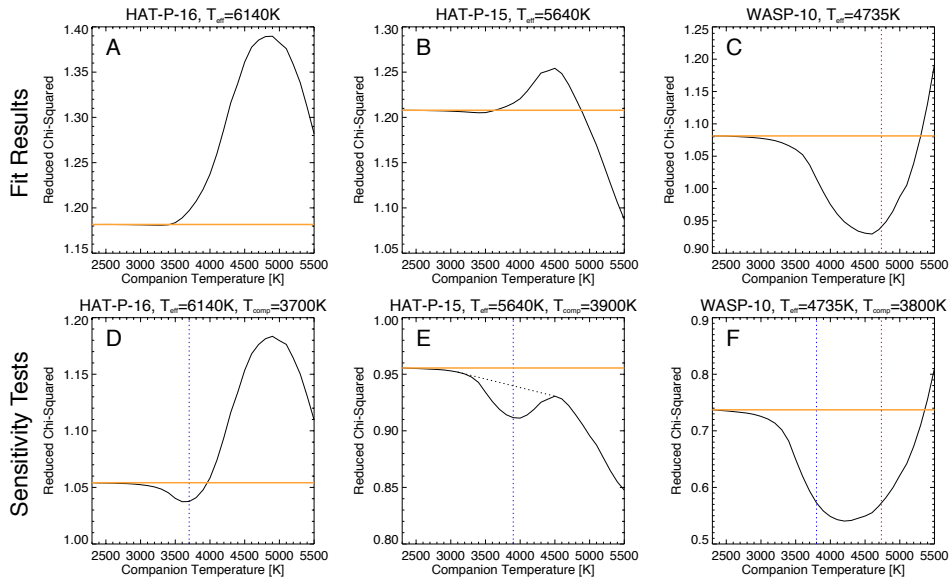

Figure 2.2: Fit results (panels A - C) and sensitivity tests (panels D - F) for HAT-P-16, HAT-P-15, and WASP-10. The solid orange and black lines represent the reduced chi-squared value of the one- and two-star models, respectively. The red dotted line represents the effective temperature of the host star and the blue dotted lines in panels D-F represent the effective temperature of the injected stellar companion. The dotted black line in panel E represents the expected slope of the χ^2 trend for a two-star fit in the case where no companion was present. These systems are classified as non-detections since there is no reliable reduction in χ^2 when a second star having an effective temperature distinct from that of the target star is added to the model fit. We are able to inject and successfully recover signals due to 3700 K and 3900 K companions in the HAT-P-16 and HAT-P-15 systems (panels D and E, respectively). We cannot recover the 3800 K signal injected into the WASP-10 system due to WASP-10's low effective temperature.

the locations on either side of the local reduced chi-squared minimum having slopes equal within 10%.

Our wavelength-dependent measurement errors are determined empirically from the data themselves and we expect them to be dominated by systematic errors due to imperfect corrections for telluric absorption and in our stellar models. As a result, there is no formal metric for determining whether or not a detection is statistically significant, and we therefore rank-order our detections from strongest to weakest according to the depth of the minimum in χ^2_{red}. Fitting our data with this same procedure, but with uniform error bars, gives the same final sets of detections and non-detections, with only slight variations in detection strengths and companion effective temperatures.

We estimate the uncertainties on the effective temperatures of the candidate stellar companions using two methods. We first calculated the range in effective temperature corresponding to a 1σ change in our best-fit χ^2 value, but found that this method produced unrealistically small error bars with a typical size of 120 K. We instead adopted a more conservative method in which we calculate the range in effective temperature corresponding to a change in χ^2_{red} equal to half the total difference between the one- and two-star models at the best-fit companion temperature. We find typical uncertainties of 250 K using this method, as shown in Table 2.3. Figure 2.1 shows the best-fit one-star and two-star models for WASP-2 in yellow and red, respectively.

Sensitivity Tests

We evaluate our sensitivity to cool stellar companions in individual systems with non-detections by injecting synthetic companions into our data and determining the lowest effective temperature for which we can reliably detect the injected companion. In doing so, we characterize our dispositive null detections, where our lack of detection implies that there is no companion in a specific temperature and semi-major axis range in that system. We create each synthetic companion spectrum by applying the previously calculated best-fit wavelength solution and instrumental broadening to a PHOENIX spectrum for a stellar companion at the desired temperature. We add this fake spectrum to the target data, scaled to the band-integrated flux of the primary star according to

$$F = \frac{R_p^2 \int_{\lambda_1}^{\lambda_2} I(T_p, \lambda)\, \mathrm{d}\lambda}{R_c^2 \int_{\lambda_1}^{\lambda_2} I(T_c, \lambda)\, \mathrm{d}\lambda}, \tag{2.3}$$

where R_p is the radius of the primary star, R_s is the radius of the companion star, λ_1 is the short-wavelength limit of the K band, λ_2 is the long-wavelength limit of the K band, $I(T, \lambda)$ is the surface brightness of the PHOENIX spectrum for each target star and each synthetic companion, T_p is the effective temperature of the primary star, and T_c is the effective temperature of the companion star. We run this composite spectrum through the fitting procedure described earlier in this section and calculate a corresponding lower limit on the temperature of the stellar companions that can be detected in our data. Note that the properties of the hot Jupiter host stars are known in advance from high-resolution optical spectroscopy, which will be minimally affected by contamination from an M dwarf companion. This precludes a scenario in which a G+M star spectrum is mistaken for a K star spectrum, as degeneracies

are only possible when the temperatures of both the primary and companion star are allowed to very as free parameters in the fits.

We carry out the procedure described above on the targets having $T_{\rm eff} \leq 5700$ K and report the dispositive null detections in Table 2.2. For targets having $T_{\rm eff} > 5700$ K (which all have chi-squared curves shaped similarly to Panel A of Figure 2.2), we find that the range of effective temperatures where the difference in χ^2_{red} between the one- and two- star models is greater than 0.005 is the same as the range of effective temperatures suggested by the full injection-and-recovery method. For these targets, we use this threshold in $\Delta\chi^2_{red}$ rather than running the full sensitivity test on each individual system, and report the range of companion temperatures corresponding to dispositive null detections in Table 2.2.

Note that Table 2.2 give the approximate maximum separation probed based on the size of the NIRSPEC slit (0.4") and the system's parallax as given in Table 2.1. In addition, HAT-P-15, TrES-2, WASP-4, WASP-16, WASP-34 have effective temperatures between 5500-5700 K, hindering our ability to detect companions by this method. We are only sensitive to companions with effective temperatures at least 500 K cooler than the primary.

2.3 Results

The results of our analysis are shown in Tables 2.2 and 2.3. Table 2.2 lists systems with non-detections as well as the range of companion temperatures that can be ruled out for systems with non-detections. Table 2.3 is organized according to the strength of the detection, which we define as the improvement in χ^2 for the two-star model as compared to the one-star model.

Note that Table 2.3 gives the approximate maximum projected separation based on the size of the NIRSPEC slit and the system's parallax as given in Table 2.1. In addition, the lower limit on $\Delta\chi^2_{red}$ for a detection was chosen using WASP-2 as a benchmark because we independently detect the companion in our AO images. (See Section 2.4.) These candidate companion detections in the HAT-P-10 and HAT-P-18 systems are likely due to star spots rather than the presence of a companion, as discussed in Section 2.4. This lower limit on $\Delta\chi^2_{red}$ for detections below the empirical threshold for significance was chosen as there is a relatively large gap (0.001 in $\Delta\chi^2_{red}$) between this detection and the next non-detection.

We classify systems with negligible improvements in χ^2 for the two-star fit as non-detections. An example is shown in panel A of Figure 2.2. As discussed in

Target Star	$T_{\rm eff}$ Range (K)	Max. Sep. (AU)
HAT-P-2	3900–5500	49
HAT-P-6	3400–5500	112
HAT-P-7	3500–5500	138
HAT-P-8	3600–5500	99
HAT-P-14	3700–5500	89
HAT-P-15	3400–4500	82
HAT-P-16	3600–5500	101
HAT-P-24	3600–5500	171
HAT-P-29	3600–5500	139
HAT-P-30	3800–5500	83
HAT-P-31	3900–5500	153
HAT-P-32	3500–5500	122
HAT-P-33	3800–5500	167
HD 149026	3800–5500	34
TrES-2	3600–5500	99
TrES-3	3600–5500	98
TrES-4	4000–5500	213
WASP-1	3800–5500	164
WASP-3	3800–5500	95
WASP-4	3700–4500	130
WASP-7	3400–5500	61
WASP-14	3500–5500	69
WASP-15	3500–5500	110
WASP-16	3300–4000	75
WASP-17	3600–5500	172
WASP-18	3900–5500	43
WASP-24	3700–5500	128
WASP-34	3300–3900	52
WASP-38	3800–5500	48
XO-3	3600–5500	80
XO-4	3600–5500	127

Table 2.2: NIRSPEC Sensitivity Limits for Systems with Dispositive Null Detections

Target Star	$\Delta\chi^2_{red}$	ΔBIC	$T_{\rm comp}(K)$	Max. Sep.(AU)
HAT-P-17	0.0162	72	3900^{+200}_{-300}	36
WASP-2	0.0109	46	3800^{+300}_{-350}	56
HAT-P-22	0.0105	44	4000^{+250}_{-400}	33
HAT-P-10	0.0099	41	4000^{+200}_{-200}	49
HAT-P-26	0.0091	37	4000^{+100}_{-350}	54
HAT-P-18	0.0085	34	4000^{+200}_{-200}	66
HAT-P-13	0.0073	28	3900^{+300}_{-350}	86
HAT-P-34	0.0073	28	3600^{+150}_{-250}	103
WASP-22	0.0063	23	3700^{+150}_{-300}	120
XO-5	0.0050	16	3500^{+250}_{-150}	104
HAT-P-4	0.0043	13	3900^{+450}_{-400}	125
WASP-8	0.0043	13	3600^{+350}_{-250}	35

Table 2.3: Systems with Candidate Companion Detections

Section 2.2, for targets having effective temperatures less than approximately 5500 K our two-star fit always finds a minimum corresponding to a fit where the primary and secondary stars have the same effective temperature. In practice this means that we are only sensitive to companions with effective temperatures at least 500 K cooler than that of the primary as illustrated in panels B and C of Figure 2.2.

Also shown in Figure 2.2 are the results of our sensitivity tests. Panels D and E shows the injection and recovery of 3700 K and 3900 K spectra in the HAT-P-16 and HAT-P-15 systems, respectively. There are 31 stars in our sample with similar sensitivity, for which we are sensitive to companions over the range of temperatures indicated in Table 2.2. Seven of the coolest stars in our sample (WASP-10, GJ436, HAT-P-11, HAT-P-12, HAT-P-20, WASP-19, and XO-2) have effective temperatures between 3400-5500 K. For these seven targets, we are unable to detect injected companions at any of the temperatures considered in this study. Panel F of Figure 2.2 shows our inability to recover a 3800 K spectrum injected into the WASP-10 system.

There are twelve targets which show a minimum in χ^2 that appears to be due to the presence of a cooler stellar companion. We show the results of the model fits for the twelve systems with candidate companions in order of detection strength in Figure 2.3, and list the corresponding companion temperatures in Table 2.3. The fit results for these twelve systems are shown in Figure 2.3 in order of detection strength. Table 2.3 gives the best-fit companion effective temperature and an upper limit on its projected separation based on the width of the NIRSPEC slit. In all cases, we find that the value of the BIC for the best-fit two-star model is lower than that of

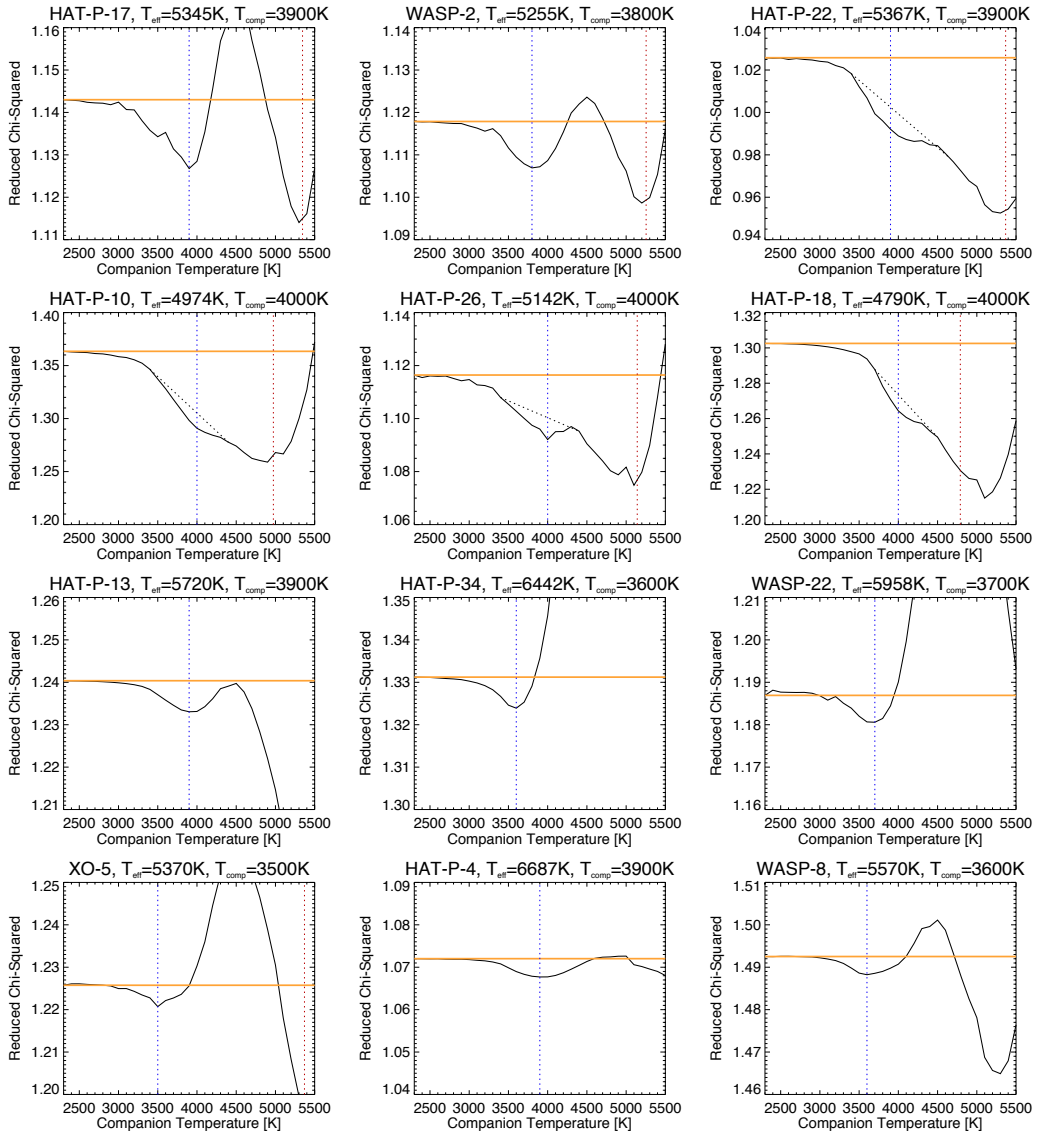

Figure 2.3: Twelve systems with cool candidate companions that pass our detection threshold as given in Table 2.3. See Fig. 2.2 caption for more information. We plot these systems in order of decreasing strength of detection, moving from left to right and top to bottom. HAT-P-17, WASP-2, and WASP-22 were observed twice, and we show the stronger of the two detections here (see Fig 2.4 for comparison). We independently resolve the companion to WASP-2 in our AO imaging, as discussed in Section 2.4. Where possible, the range of reduced chi-squared values plotted is 0.05. Elsewhere, the range is expanded to accommodate the strength of the detection.

the best-fit one-star model for all candidate companions listed in Table 2.3, thereby justifying the addition of the extra parameter (the temperature of the companion star) to the model.

We present our results in terms of the reduced chi-squared value in order to demonstrate the relative quality of our fits. The reduced chi-squared values are often slightly greater than 1 indicating that our errors are likely underestimated, despite our use of empirical estimates for the measurement errors at each individual wavelength as described in Section 2.2. In addition, the apparent small discontinuity at 5000 K in some of our reduced chi-squared plots is due to a change in the λ_{ref} used to calculate the optical depth grid in the PHOENIX models (Husser et al. 2013). Differences in the shape of the χ^2 curve for targets having similar effective temperatures are likely due to different observing conditions.

2.4 Discussion

Systems with No AO- or RV-Companion Detections

Here, we list the systems which have a candidate companion detected by the NIRSPEC survey alone.

HAT-P-17

As shown in Figure 2.3, the model fit is significantly improved by the presence of a 3900^{+200}_{-300} K companion in the HAT-P-17 system. According to the size of the NIRSPEC slit, this companion has a projected separation of less than about 36 AU. Our AO survey would only have detected a 3900 K companion if it were outside 60 AU. We also obtained a second spectrum of HAT-P-17 (Fig. 2.4) on a different night in order to make sure that the candidate companion was reliably detected in both data sets. We find consistent results from both nights albeit with varying significance, and report the stronger of the two detections in Table 2.3. If the projected separation of the companion is comparable to that of the NIRSPEC slit width, the strength of the detection will vary depending on the slit orientation relative to the position angle of the binary.

HAT-P-26

For HAT-P-26, we are careful to calculate the improvement in $\Delta\chi^2_{red}$ due to the presence of the cooler companion after subtracting off the residual slope due to the primary star, as shown by the dotted line in Figure 2.3. We detect a candidate

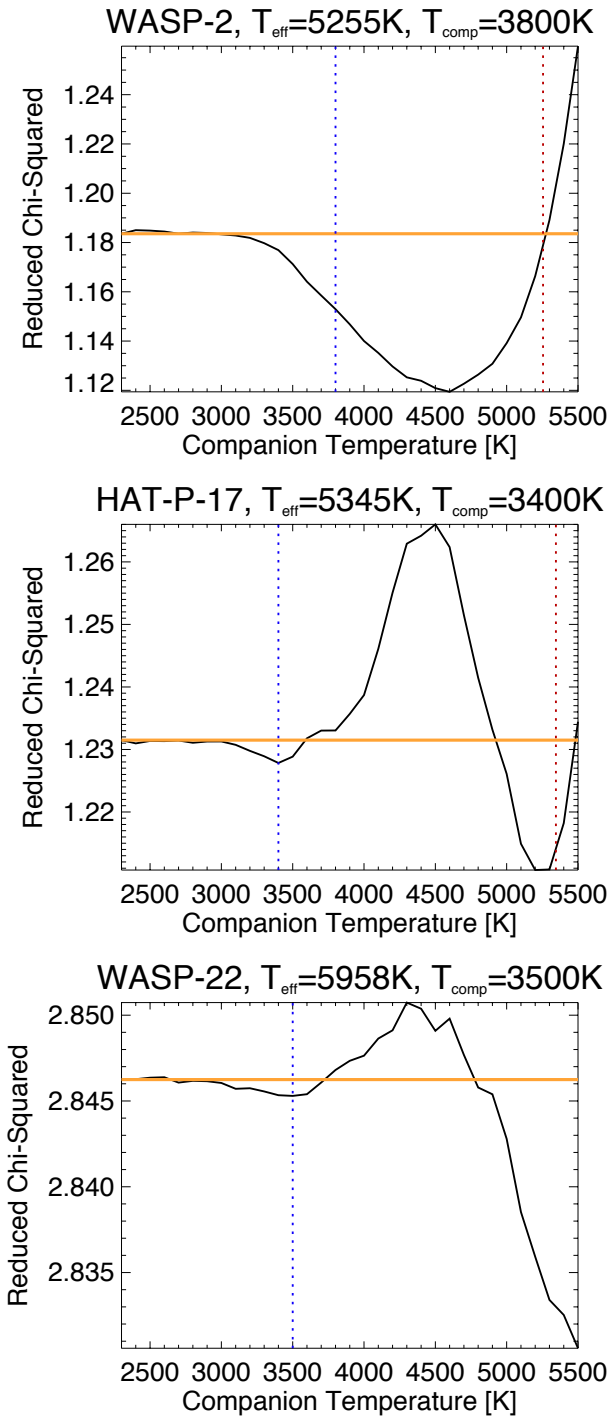

Figure 2.4: A second epoch of data for WASP-2, HAT-P-17, and WASP-22 (see Figure 2.3 caption for more information). For HAT-P-17 and WASP-22 the blue dotted line represents the effective temperature of the best-fit two-star model. For WASP-2, the blue dotted line shows the best-fit two-star model effective temperature suggested by the analysis of the July 2013 data. The companion in this system is resolved in our AO images and has a projected separation of 0.73", thus it will only be detected in cases where the slit is effectively parallel to the position angle of the two stars. This changing slit orientation may also explain the varying detection strengths for HAT-P-17 and WASP-2.

companion in this system having an effective temperature of 4000^{+100}_{-350} K and a projected separation less than 54 AU. A companion having this temperature would not have been detectable by our AO survey. The shape of our χ^2_{red} curve for this star is analogous to that of the non-detection HAT-P-15 with a 4000 K companion injected into its spectrum as shown in Fig. 2.2.

HAT-P-18

For the HAT-P-18 system, we detect a candidate companion with an effective temperature of 4000^{+200}_{-200} K and projected separation less than about 66 AU. Our AO survey would only have been sensitive to a 4000 K companion if it were outside 140 AU.

We note that this star is relatively active with $\log(R'_{\rm HK})$=-4.799 (Knutson et al. 2010), and it is therefore likely that the observed minimum is due to spots on the visible face of the star. Previous studies (Frasca et al. 2005; Pont et al. 2008; Sing et al. 2011) have shown that these star spots typically have temperatures 500-1000 K cooler than that of the primary star, in good agreement with the temperature difference observed in this system.

HAT-P-34

In the HAT-P-34 system, we find a 3600^{+150}_{-250} K candidate companion with a projected separation less than about 103 AU. Such a companion would have been undetectable in our AO survey.

XO-5

We detect a candidate companion in the XO-5 system having an effective temperature of 3500^{+250}_{-150} K and a projected separation less than about 104 AU. Our AO survey was unable to detect such a cool companion.

Systems with AO-Detected Companions

We check to see if any of our spectroscopically detected candidate companions are detected independently in the AO imaging survey presented in Ngo et al. (2015). We obtained our data in parallel with the AO survey, and so did not have any prior knowledge of the positions of resolved stellar companions in these systems that could have been used to determine the optimal slit position angle in the sky. Because NIRSPEC has a slit width of 0.4", we expect that we are only sensitive to

companions with projected separations smaller than 0.2-0.4" unless they happened to be aligned along the slit in our NIRSPEC observations. We identify three systems with both resolved AO companions and candidate spectroscopic companions, and discuss them each individually below.

WASP-2

An AO companion to WASP-2 was detected first on July 27 2012 and June 22 2013 with an average $T_{\rm eff}$=3513±28 K and separation of 0.73"±0.0015" (Ngo et al. 2015). Although this projected separation is larger that the NIRSPEC slit width of 0.4", we expect the companion would still be detectable if it happened to fall along the direction of the slit in our NIRSPEC observations. This appears to be the case, as we detect a stellar companion with $T_{\rm eff}$=3800^{+300}_{-350} K in our UT 27 August 2012 observation. We also obtained a second spectrum of WASP-2 (Fig. 2.4) on a different night and list the stronger of the two detections in Table 2.3. Since the projected separation is known to be greater than the size of the NIRSPEC slit, it is likely that varying amounts of companion starlight were gathered on the two nights, producing model fits of differing qualities.

This is the only system in which we independently detect the companion using both spectroscopy and AO imaging, and we therefore use this system to determine an empirical threshold for spectroscopic detections. The $\Delta\chi^2_{red}$ for the companion in the system is 0.01, and we therefore adopt a cutoff of 0.005 for determining our list of candidate companions in Table 3.

HAT-P-10

We detect a bound companion to this star in our K band AO imaging with an effective temperature of $T_{\rm eff}$=3494±37 K and a projected separation of 0.36"±0.0015" (Ngo et al. 2015). Although the projected separation of this companion is smaller than the NIRSPEC slit width, we do not detect it in our spectroscopic observations. As shown in Table 2.2 our injection and recovery tests indicate that the companion in this system falls below our detection threshold for this technique. Additionally, if the position angle of the binary companion was perpendicular to the slit and the primary star was located in the middle of the slit, the companion may still have fallen outside the slit aperture.

Although we do not independently recover the AO companion in this system, we do find a minimum in our two-star fits at an effective temperature of 4000^{+200}_{-200} K.

Similar to HAT-P-18, HAT-P-10 is relatively active with $\log(R'_{\rm HK})$=-4.82 (Knutson et al. 2010). Therefore, it is likely that the observed chi-squared minimum is due to spots on the visible face of the star.

WASP-8

An AO-companion to WASP-8 was detected on July 27 2012 and August 19 2013 with an average $T_{\rm eff}$=3591±157 K and separation of 4.50"±0.0026" (Ngo et al. 2015). The separation between WASP-8 and its stellar companion is much larger than the width of the NIRSPEC slit, and it is therefore unlikely that this companion would contribute to our measured NIRSPEC spectrum. Although we identify a weak minimum in our spectroscopic analysis corresponding to a companion with an effective temperature of 3600^{+350}_{-250} K, this minimum falls below our empirical cutoff for a significant detection.

Systems with RV-Detected Companions

Here, we ask whether or not the candidate spectroscopic companions could have caused the RV trends. We therefore consider whether or not any of the candidate spectroscopic stellar companions detected in this study might be responsible for the radial velocity accelerations reported in Knutson et al. (2014).

For the systems where the mass of NIRSPEC candidate companion is consistent with the measured radial velocity trend, we calculate the system's likely angle from face-on given by

$$\sin\theta = \frac{\dot{\gamma} a_c^2}{G M_c} \tag{2.4}$$

as in Winn et al. (2009), where $\dot{\gamma}$ is the RV trend measured by Knutson et al. (2014), M_c is the mass of the NIRSPEC candidate companion calculated from $T_{\rm eff}$ according to Baraffe et al. (2003), and a_c is the candidate companion's semi-major axis. This latter value is the least well-known and only vaguely constrained by the size of the NIRSPEC slit.

HAT-P-22

In Knutson et al. (2014) we reported a radial velocity acceleration due to a companion with $M \sin i$ between 0.7-125 $M_{\rm Jup}$ and semi-major axis of 3.0-28 AU (1σ constraints), where upper limits on the companion mass and orbit were calculated based on the AO non-detection. We report a candidate spectroscopic companion in this system with an effective temperature of 4000^{+250}_{-400} K, corresponding to a mass

of 660^{+75}_{-175} $M_{\rm Jup}$ and a maximum projected separation of 33 AU (0.4"). According to equation 2.4, if this companion has an orbital semi-major axis less than 33 AU it must have a face-on orbit in order to be consistent with the observed RV trend. It is also possible that the companion is located at larger semi-major axes, but was observed at a time when it had a relatively small projected separation and/or small radial velocity slope.

HAT-P-10

In Knutson et al. (2014) we detected a long-term radial velocity acceleration in the HAT-P-10 system, which was consistent with having been caused by a directly imaged AO companion reported in Ngo et al. (2015). As discussed in Section 2.4, the NIRSPEC detection is likely an indication of stellar activity.

HAT-P-13

HAT-P-13 has two companions detected with RV. The first, HAT-P-13c, has an $M\sin i$ of 14.23-15.18$M_{\rm Jup}$ and a semi-major axis of 1.24-1.28 AU (1σ constraints). HAT-P-13d has an $M\sin i$ of 15-200 $M_{\rm Jup}$ and a semi-major axis of 12-37 AU (1σ constraints). Our candidate spectroscopic companion has an effective temperature of 3900^{+300}_{-350} K, which corresponds to a mass of $0.602^{+0.086}_{-0.179}$ $M_\odot$ or 630^{+91}_{-187} $M_{\rm Jup}$, and projected separation $\lesssim 85.6$ AU. If the candidate spectroscopic companion were HAT-P-13d identified by our RV survey, then it must have an inclination within 5° of face-on. However, Winn et al. (2010) argue that this system is likely coplanar, as otherwise the influence of the outer companions would tend to misalign the orbit of the inner transiting hot Jupiter with respect to the star's spin axis. They find that the innermost planet's orbit is well-aligned with the star's spin axis, suggesting that the $M\sin i$ values of the outer two companions are likely close to their true masses. For the same reason we argue here that any outer stellar companion must also be coplanar with the orbits of the planets in this system. This constraint might be relaxed if the stellar companion was distant enough that Kozai-type oscillations would not occur (see Ngo et al. 2015 and references therein), but this would require that the system was observed at a time when the projected separation between the companion and the primary was small in order to remain consistent with both our spectroscopic detection and our non-detection in AO images of this system. If we require the companion to be coplanar with the inner planets, then our radial velocity measurements allow us to rule out scenarios where the stellar companion is located

interior to 40 AU on a high inclination orbit.

WASP-22

We detect a radial velocity acceleration in this system corresponding to a companion with $M\sin i$ between 7-500 $M_{\rm Jup}$ and a semi-major axis between 6-40 AU. The candidate spectroscopic companion in this system has an effective temperature of 3700^{+150}_{-300} K, which corresponds to a mass of $0.523^{+0.063}_{-0.253}$ $M_{\odot}$ or 548^{+66}_{-266} M_{Jup}, and separation $\lesssim$ 120 AU. We therefore conclude that our spectroscopic candidate could have caused the radial velocity acceleration measured in this system if it is on an orbit within 10° of face-on. We also obtained a second spectrum of WASP-22 (Fig. 2.4) on a different night in order to make sure that the candidate companion was reliably detected in both data sets. We find consistent results from both nights albeit with varying significance, and report the stronger of the two detections in Table 2.3.

Detections below Empirical Threshold for Significance

Here we discuss the results for the systems showing marginal detections of a companion star in order to determine the effectiveness of our threshold of $\Delta\chi^2_{red} \geq 0.005$.

HAT-P-4

The radial velocity companion in this system is constrained to have $M\sin i$ between 1.5-310 $M_{\rm Jup}$ and a semi-major axis of 5-60 AU (1σ constraints). We identify a marginally significant spectroscopic signal corresponding to a stellar companion with an effective temperature of 3900^{+450}_{-400} K and a mass of $0.602^{+0.123}_{-0.224}$ $M_{\odot}$ or 631^{+129}_{-236} M_{Jup} at a projected separation of less than 120 AU. If the RV signal is caused by this companion, then it must either be located in a short-period orbit within 4° of face-on, or on a more distant orbit with a small projected separation and/or small radial velocity slope.

WASP-8

The radial velocity acceleration in this system displays significant curvature, and we are therefore able to place relatively tight constraints on the mass and orbital separation of the companion responsible for the acceleration. In this case we find that the companion has $M\sin i$ between 6.3-10.7 $M_{\rm Jup}$, and we therefore conclude that it is most likely a low-mass brown dwarf or planetary companion. Our candidate

spectroscopic companion in this system is a relatively weak detection and has an effective temperature of 3600^{+350}_{-250} K and a projected separation of less than 35 AU. Therefore, if this NIRSPEC companion candidate is in fact a true companion, then the NIRSPEC companion is not the same as the RV companion. We also detect an AO companion in this system with a temperature of 3590 K and a projected separation of 4.50", which is too large to be detected in our NIRSPEC observation. It seems unlikely that this system would contain a hot Jupiter, an outer planetary or brown dwarf companion, and two stellar companions with widely varying orbital separations, and we therefore conclude that the NIRSPEC detection in this system is unlikely to be real. This would not be surprising, as this is the weakest of the candidate companion detections listed in Table 2.3.

Given the specious nature of the candidate companion in the WASP-8 system, we assert our empirical detection threshold of $\Delta\chi^2_{red} \geq 0.005$ is a reasonable lower limit for identifying candidate companions in these systems.

2.5 False Detections Due to Star Spots

We identify the spectroscopic signal of star spots in the spectra of HAT-P-18 and HAT-P-10, as discussed in Section 2.4. Converting the area ratio for each star and its "candidate companion" suggests that the fraction of the stellar surface covered by star spots is 39% and 37% for HAT-P-18 and HAT-P-10, respectively. This level of star spot coverage is somewhat high, although not unheard of (e.g. Jackson and Jeffries 2013). In an attempt to gain more specific information on the fraction of these stars covered by star spots, we vary the contribution of the cool star spectrum to the two-star model. However, we find that there is no clear minimum separate from that of the stellar effective temperature. This suggests that the temperature of the star spots is degenerate with their fractional area over the range of effective temperatures considered in our fits.

We next consider the candidate companions around the other stars in our sample. If we attribute these spectroscopic signals to star spots we find that the fractional flux contributions of the candidate companions correspond to star spot coverage fractions between 9-37%. Although we cannot distinguish between star spots and low mass companions on the basis of our spectra alone, we consider it unlikely that all of the candidate companions presented in this paper are in fact due to stellar activity. HAT-P-18 and HAT-P-10 are relatively active stars with relatively low effective temperatures. As shown in Figure 2.5, the remaining systems with

candidate companions appear to be relatively quiet stars as measured by $\log(R'_{\rm HK})$, with the caveat that this index may not be a reliable activity indicator for stars with effective temperatures greater than 6000-6200 K (e.g., Knutson et al. 2010). Furthermore, the candidate companion temperatures implied by our fits to these quiet stars are much cooler than would be expected for star spots. We therefore conclude that HAT-P-10 and HAT-P-18 are the only systems in which our detection of a candidate companion can plausibly be explained as stellar activity.

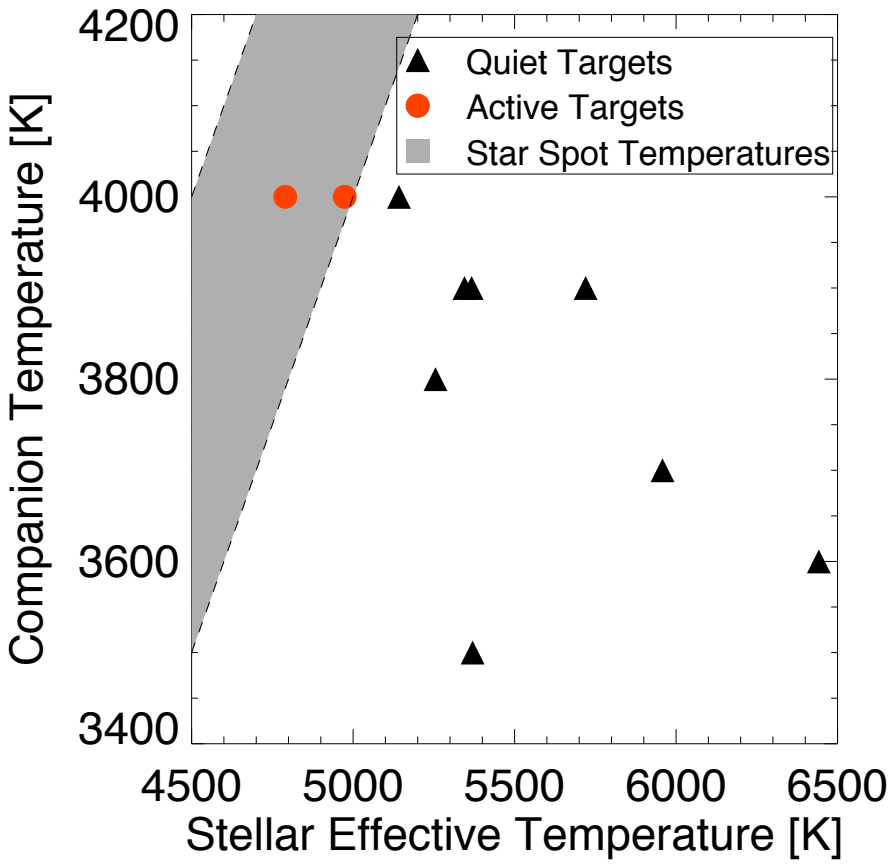

Figure 2.5: Effective temperatures of the twelve targets and their candidate companions. Targets having $\log(R'_{\rm HK})$< -4.9 are classified as quiet stars and plotted as black filled triangles. HAT-P-10 and HAT-P-18 have log(R') > -4.9 indicating moderate levels of activity, and are shown as red filled circles in this plot. The shaded region represents the expected star spot temperatures as a function of stellar effective temperature according to Frasca et al. (2005), Pont et al. (2008), and Sing et al. (2011).

2.6 Companion Fraction

Although our candidate spectroscopic companions still require additional confirmation, we can nonetheless calculate an upper limit to the companion fraction in our sample corresponding to the case where all candidates are confirmed as real. These companions have $T_{\rm eff}$ = 3500-4000 K and projected separations less than 125 AU. We exclude the seven cool stars listed in Section 3 from this calculation, as our NIRSPEC observations are not sensitive to low-mass stellar companions in these systems. Of the systems with candidate companion detections, we exclude HAT-P-10 and HAT-P-18 as the detections in these systems are likely due to stellar activity. We also exclude HAT-P-4 and WASP-8 as the detections in these systems fall below our empirical threshold for significance, and WASP-2 as AO imaging indicates that the companion in this system has a projected separation greater than 0.4". We find an *uncorrected* binary fraction of 18% ± 6% for the full survey sample, 20% ± 9% for the subset of short period gas giant planets with eccentric and/or misaligned orbits, and 25% ± 9% for the subset of planets with apparently well-aligned and circular orbits.

In order to correct for survey incompleteness we must make some assumptions about the properties of the underlying population of stellar companions in our target sample. We consider two scenarios, including one where the detected companions are all on wide orbits similar to those of the companions detected in our previous AO survey (Ngo et al. 2015), but happen to be observed at a time when they have a small projected separation. We also consider a scenario in which the companions are on orbits that are too close in to have been detected by our AO survey but far enough out to be consistent with a non-detection in our radial velocity survey (Knutson et al. 2014). For each underlying population, we calculate our sensitivity S_i for each survey target i to companions having effective temperatures within the ranges shown in Table 2.2 and projected separations less than 0.4" at the time of observation. We compute the likelihood L of obtaining our specific observations as follows:

$$L(\eta) = \prod_{i=1}^{N} (S_i \eta)^{d_i} (1 - S_i \eta)^{(1-d_i)}, \tag{2.5}$$

where η is the true/intrinsic companion fraction and d_i=1 for systems with NIRSPEC detections and $d_i = 0$ for systems without NIRSPEC detections.

Are these companions drawn from the population of wide companions detected in previous surveys?

In this scenario we assume that the observed NIRSPEC companions are part of the same population as the wide-separation companions detected in our AO survey. In this case the NIRSPEC companions would be located on relatively wide orbits, but happen to be observed at a time when they have projected separations of less than 0.4". We calculate our sensitivity S_i to this population for each target star by generating 10^6 simulated binary companions with orbital elements and mass ratio distributions drawn from field star surveys (Raghavan et al. 2010) and periods between 10^4 and $10^{7.5}$ days, as described in Ngo et al. (2015). We then determine the fraction of these simulated companions that would have been detected by our NIRSPEC observations.

For this population, we find that our average survey sensitivity is 28% with a standard deviation of 9%. If we assume an intrinsic companion fraction of 49% ± 9% as reported in Ngo et al. (2015), then we would expect to detect companions in 13% ± 5% of the systems in our NIRSPEC sample. This is entirely consistent with our actual raw companion fraction of 18% ± 6%, which is in fact an upper limit predicated on the assumption that all of the candidate companions are real. We therefore conclude that our data do not require these systems to have an additional population of close-in stellar companions, but are instead consistent with being drawn from the same population of wide-separation companions detected in our previous AO survey.

Using equation 5 and assuming that the underlying population has the same mass ratio and period distribution as the AO sample, we find that the corrected companion fraction is $\eta_T = 58\% \pm 19\%$, consistent with the $49\% \pm 9\%$ companion fraction from our AO survey. The corrected companion fraction for the subset of planets with misaligned and/or eccentric orbits is $\eta_M = 51\% \pm 30\%$, and for well-aligned planets on circular orbits is $\eta_C = 65\% \pm 30\%$. These occurrence rates are consistent with one another and suggest that there is no obvious preference for misaligned hot Jupiter systems to have stellar companions drawn from the AO sample.

Are these companions drawn from the population of intermediate companions detected in field star surveys?

We next consider whether or not the candidate companions detected in this survey might be a field star population of intermediate-period companions located too

close in to be detectable in AO images and too far out to be detected with with radial velocity monitoring. We calculate the sensitivity of our survey to this population by simulating 10^6 binary companions with orbital elements and mass ratio distributions drawn from Raghavan et al. (2010). We only consider systems with periods less than 10^4 days (i.e., interior to our cutoff for the AO survey) and those which do not create detectable RV trends. In our formulation, a binary system has no detectable RV trend if the following criterion is satisfied:

$$\frac{GM_{sim}\sin\theta}{a_{sim}^2} < \dot{\gamma}_i + 3\sigma_{\dot{\gamma}_i}, \tag{2.6}$$

where M_{sim} and a_{sim} are the mass and semi-major axis of the simulated binary companion and θ is the angle from face-on, as in equation 2.4. $\dot{\gamma}_i$ is the RV trend slope measured for system i in Knutson et al. (2014) and $\sigma_{\dot{\gamma}_i}$ is the error on that measurement.

For this population, we find that our average survey sensitivity is 49% with a standard deviation of 14%. This corresponds to a completeness-corrected companion fraction $\eta_T = 34\% \pm 11\%$ for the total sample, $\eta_M = 29\% \pm 17\%$ for the misaligned sample, and $\eta_C = 38\% \pm 17\%$ for the control sample. As before, we conclude that there is no detectable correlation between the presence of a stellar companion and the orbital properties of the transiting gas giant planet. We find that stellar companions that meet these two criterion typically have semi-major axes between 0.4 - 12.1 AU. Of field stars surveyed by Raghavan et al. (2010), 17% ± 2% had companions in this semi-major axis range. We therefore conclude that, if these companions are drawn from a unique intermediate period sample, our upper limit on the companion fraction for this population is consistent with the rates for field stars with comparable separations.

2.7 Conclusion

We perform a spectroscopic search of fifty hot Jupiter host stars in order to search for blended lines due to cool stellar companions with projected separations of less than 0.4". We detect eight candidate companions having effective temperatures ranging from 3500-4000 K. This method is complementary to our previous AO imaging survey of these same systems, which was sensitive to companions with projected separations larger than 0.4-0.5". It also allows us to determine whether or not any of the radial velocity trends in these systems might be due to high inclination stellar binaries as opposed to planetary or brown dwarf companions. Our detection sensitivity and corrected companion fractions are consistent with a scenario in

which all of the observed companions are located at larger orbital separations (i.e., consistent with the population of companions detected in our previous AO survey). Our results are also consistent with a scenario in which the observed companions are located at intermediate separations (0.4-12 AU) with a frequency comparable to that of field stars.

Regardless of the underlying population model, we find no evidence for a correlation between the presence of a spectroscopic stellar companions and the spin-orbit misalignment or orbital eccentricity of the transiting gas giant planets in these systems. Other surveys have suggested that misaligned hot Jupiters preferentially orbit stars having $T_{\rm eff} > 6200$ K (Winn et al. 2010). We note that hot stars also have higher intrinsic binary fractions (e.g., Duchene & Kraus 2013), which might lead to a spurious correlation between spin-orbit alignment and stellar multiplicity if most of our misaligned planets are located preferentially around hot stars. We selected our sample of well-aligned planets on circular orbits to have approximately the same distribution of stellar masses as our sample of misaligned and/or eccentric planets (see section 2.1 of Knutson et al. (2014)) in order to ensure that this was not an issue. We also note that this study identifies only one system with $T_{\rm eff} > 6200$ K containing a candidate companion, providing additional confirmation that our results are unaffected by this correlation. Other studies have suggested that tides can remove non-zero obliquities for planets orbiting stars cooler than 6200 K (Spalding & Batygin 2015), although planets orbiting hotter stars with less efficient tides should still retain their primordial spin-orbit alignments. In Ngo et al. (2015) we addressed this issue by repeating our spin-orbit alignment correlation test for the subset of stars hotter than 6200 K, and found no evidence for a correlation between spin-orbit alignment and stellar multiplicity. Although we could in theory repeat this analysis with our new sample of candidate companions, in practice we are limited in this case by the small number of companions detected in this survey. If misaligned orbits are instead the results of a primordial misalignment in the protoplanetary disk (Spalding & Batygin 2014), the stellar companions responsible for the misalignment might have been lost to dissolution or exchange in the cluster, therefore weakening the observed correlation between spin-orbit misalignment and the presence of a stellar companion at the current epoch. Finally, there would be no correlation between companion stars and misaligned planets if misalignment were caused by magnetic torque (Lai et al. 2011) or turbulent accretion (Bate et al. 2010; Fielding et al. 2014), neither of which require the presence of a stellar companion. Although our data appear to be consistent with this hypothesis, these models are unable to reproduce

the observed obliquity distribution for short-period gas giant planets (Spalding et al. 2014).

An independent confirmation of these spectroscopic detections would allow us to reliably calculate the statistical significance of our spectroscopic detections and to combine the results of this study with our previous RV and AO surveys in order to provide an improved estimate of the stellar multiplicity rate for these systems. As shown in Teske et al. (2015), combined direct imaging and spectroscopic surveys provide an unparalleled look at the properties of stellar companions in these systems. In the future we plan to obtain high-contrast imaging follow-up observations using angular differential imaging on NIRC2 at Keck (Marois et al. 2006) and the Differential Speckle Survey Instrument at Gemini Observatory (Horch et al. 2009), which will achieve better contrasts at small separations than our previous K band AO images with NIRC2. Because our candidate spectroscopic companions have negligible radial velocity offsets from the primary and are not typically detected by long-term radial velocity monitoring of the host star, we conclude that they are unlikely to have very small orbital separations and therefore should be resolvable with improved high-contrast imaging. In systems where we are able to directly resolve the candidate spectroscopic stellar companions, we will be able to place improved constraints on their masses and orbits.

Next, we turn away from investigations of hot Jupiter migration mechanisms and turn towards investigations of hot Jupiter formation.

2.8 References

For Table 2.1 only

(1) Bonfils, X., Delfosse, X., Udry, S., et al. 2005, A&A, 442, 635

(2) Maness, H. L., Marcy, G. W., Ford, E. B., et al. 2007, PASP, 119, 90

(3) von Braun, K., Boyajian, T. S., Kane, S. R., et al. 2012, ApJ, 753, 171

(4) Torres, G. 2007, ApJ, 671, 1

(5) Torres, G., Fischer, D. A., Sozzetti, A., et al. 2012, ApJ, 757, 161

(6) Pál,A. , G. Á. Bakos, G. Torres, et al. 2010, MNRAS, 401, 4

(7) Winn, J. N., Fabrycky, D., Albrecht, S., & Johnson, J. A. 2010a, ApJL, 718, L145

(8) Kovacs, G., Bakos, G. Á., Torres, G., et al. 2007, ApJL, 670, L41

(9) Noyes, R. W., Bakos, G. Á., Torres, G., et al. 2008, ApJL, 673, L79

(10) Van Eylen, V., Kjeldsen, H., Christensen-Dalsgaard, J., & Aerts, C. 2012, AN, 333, 1088

(11) Pál, A. , Bakos, G. Á., Fernandez, J., et al. 2009, ApJ, 700, 783

(12) Mancini, L., Southworth, J., Ciceri, S., et al. 2013b, A&A, 551, A11

(13) Latham, D. W. , G. Á. Bakos, G. Torres, et al. 2009, ApJ, 704, 2

(14) Bakos, G. A.,Pál, A., Torres, G., et al. 2009b, ApJ, 696, 1950

(15) Bakos, G. A., Torres, G.,Pál, A., et al. 2010, ApJ, 710, 1724

(16) Hartman, J. D., Bakos, G. Á., Torres, G., et al. 2009, ApJ, 706, 785

(17) Southworth, J., Hinse, T. C., Dominik, M., et al. 2012b, MNRAS, 426, 1338

(18) Torres, G., Bakos, G. A., Hartman, J., et al. 2010, ApJ, 715, 458

(19) Kovacs, G., Bakos, G. Á., Hartman, J. D., et al. 2010, ApJ, 724, 866

(20) Buchhave, L. A., Bakos, G. Á., Hartman, J. D., et al. 2010, ´ ApJ, 720, 1118

(21) Howard, A. W., Bakos, G. Á., Hartman, J., et al. 2012, ApJ, 749, 134

(22) Hartman, J. D., Bakos, G. Á., Torres, G., et al. 2011c, ApJ, 742, 59

(23) Bakos, G. Á., J. Hartman, G. Torres, et al. 2011, ApJ, 742, 116

(24) Kipping, D. M., Bakos, G. Á., Hartman, J., et al. 2010, ApJ, 725, 2017

(25) Buchhave, L. A., Bakos, G. Á, Hartman, J. D., et al. 2011, ´ ApJ, 733, 116

(26) Johnson, J. A., Winn, J. N., Bakos, G. Á., et al. 2011, ApJ, 735, 24

(27) Kipping, D. M., Hartman, J., Bakos, G. Á., et al. 2011, AJ, 142, 95

(28) Bakos, GÁ , JD Hartman, G Torres, et al. 2012, AJ, 144, 19

(29) Carter, J. A., Winn, J. N., Gilliland, R., & Holman, M. J. 2009, ApJ, 696, 241

(30) Barclay, T., Huber, D., Rowe, J. F., et al. 2012, ApJ, 761, 53

(31) O'Donovan, F. T., D. Charbonneau, G. Mandushev, et al. 2009, ApJ, 651, 1

(32) Sozzetti, A., Torres, G., Charbonneau, D., et al. 2009, ApJ, 691, 1145

(33) Bergfors, C., Brandner, W., Daemgen, S., et al. 2013, MNRAS, 428, 182

(34) Miller, G. R. M., A. Collier-Cameron, E. K. Simpson, et al. 2010, A&A, 523, A52

(35) Gibson, N. P., Pollacco, D., Simpson, E. K., et al. 2008, A&A, 492, 603

(36) Wilson, D. M., Gillon, M., Hellier, C., et al. 2008, ApJL, 675, L113

(37) Doyle, A. P., Smalley, B., Maxted, P. F. L., et al. 2013, MNRAS, 428, 3164

(38) Hellier, C., D. R. Anderson, M. Gillon, et al. ApJ, 690, L89

(39) Queloz, D., Anderson, D. R., Collier Cameron, A., et al. 2010, A&A, 517, L1

(40) Johnson, J. A., Winn, J. N., Cabrera, N. E., & Carter, J. A. 2009b, ApJL, 692, L100

(41) Christian, D. J., Gibson, N. P., Simpson, E. K., et al. 2009, MNRAS, 392, 1585

(42) Joshi, Y. C., Pollacco, D., Collier Cameron, A., et al. 2009, MNRAS, 392, 1532

(43) Southworth, J., Mancini, L., Browne, P., et al. 2013, MNRAS, 434, 1300

(44) Anderson, D. R., Hellier, C., Gillon, M., et al. 2010, ApJ, 709, 159

(45) Anderson, D. R., Collier Cameron, A., Gillon, M., et al. 2011, A&A, 534, A16

(46) Street, R. A., Simpson, E., Barros, S. C. C., et al. 2010, ApJ, 720, 337

(47) Smalley, B., Anderson, D. R., Collier Cameron, A., et al. 2011, A&A, 526, A130

(48) Brown, D. J. A., Collier Cameron, A., Diaz, R. F., et al. 2012b, ApJ, 760, 139

(49) Burke, C. J., McCullough, P. R., Valenti, J. A., et al. 2007, ApJ, 671, 2115

(50) Winn, J. N., Holman, M. J., Torres, G., et al. 2008a, ApJ, 683, 1076

(51) Johns-Krull, C. M., McCullough, P. R., Burke, C. J., et al. 2008, ApJ, 677, 657

(52) McCullough, P. R., Burke, C. J., Valenti, J. A., et al. 2008, arXiv:0805.2921

For All of Chapter 2

Adams, E.R., Ciardi, D.R., Dupree, A.K. et al. 2012, AJ, 144, 42

Albrecht, S., Winn, J. N., Johnson, J. A., et al. 2012b, ApJ, 757, 18

Baraffe, I., Chabrier, G., Allard, F., & Hauschildt, P. H. 1998, A&A, 337, 403

Bardalez Gagliuffi, D. C., Burgasser, A. J., Gelino, C. R., et al. 2014, AJ, 794, 143

Bate, M. R., Lodato, G., & Pringle, J. E. 2010, MNRAS, 401, 1505

Batygin, K., Morbidelli, A., & Tsiganis, K. 2011, A&A, 533, A7

Batygin, K. 2012, Nature, 491, 418

Beaugé, C., & Nesvorný, D. 2012, ApJ, 751, 119

Bechter, E. B., Crepp, J. R., & Ngo, H. et al. 2014, ApJ, 788, 2

Birkby, J. L., de Kok, R. J., & Brogi, M. et al. 2013, MNRAS, 436, L35

Bodenheimer, P., Hubickyj, O., & Lissauer, J. J. 2000, Icarus, 143, 2

Bonnell, I.A., Smith, K.W., Davies, M.B. et al. 2001, MNRAS, 322, 859

Boogert, A. C. A., Blake, G. A., & Tielens, A. G. G. M. 2002, ApJ, 577, 271

Burgasser, A. J., Cruz, K. L., Cushing, M., et al. 2010a, ApJ, 710, 1142

Cheetham, A.C., Kraus, A.L., Ireland, M.J., et al. 2014, ApJ(accepted), arXiv:1509.05217

Claret, A . 2010, A&A, 529, A79

Dawson, R.I., & Murray-Clay, R.A. 2013, ApJ, 767, L24

de Mooij, E.J.W., Brogi, M., de Kok, R.J., et al. A&A 538, A46 (2012)

Doyle, L.R., Carter, J.A., Fabrycky, D.C., et al. 2011, Science, 333, 1602

Duchene, G., & Kraus, A. 2013, ARA&A, 51, 269

Duquennoy, A., & Mayor, M. 1991, A&A, 248, 485

Eggenberger, A., Udry, S., Chauvin, G., et al. 2007, A&A, 474, 273

Fabrycky, D., & Tremaine, S. 2007, ApJ, 669, 1298

Fielding, D. B., McKee, C. F., Socrates, A., Cunningham, A. J., & Klein, R. I. 2014, MNRAS, 450, 3

Frasca, A., K. Biazzo, S. Catalano, et al. 2005, A&A, 432, 2

Goldreich, P., & Tremaine, S. 1980, ApJ, 241, 425

Gray, D.F. 2005, *The Observation and Analysis of Stellar Photospheres*. Cambridge University Press, Cambridge, 3 edition

Guenther, E.W., Fridlund, M., Alonso, R. et al. 2013, A&A, 556, 75

Hao, W., Kouwenhoven, M.B.N., & Spurzem, R. 2013, MNRAS, 433, 867

Horch, E. P., Veillette, D. R., Galle, R. B., et al. 2009, AK, 137, 6

Husser, T.-O., Wende-von Berg, S., Dreizler, S., et al. 2013, A&A, 553, A6

Jackson, R.J., & Jeffries, R.D. 2008, MRNAS, 431, 2

Kley, W. & Nelson, R.P. 2012, ARA&A, 50, 211-249

Knutson, H. A., Howard, A. W., & Isaacson, H. 2010, ApJ, 720, 1569

Knutson, H. A., B. J. Fulton, B. T. Montet et al. 2014, ApJ, 785, 126

Kolbl, R., G. W. Marcy, H. Isaacson, et al. 2015, AJ, 149, 18

Kraus, A. L., M. J. Ireland, L. A. Hillenbrand, et al. 2012, ApJ, 745, 19

Lai, D., Foucart, F., & Lin, D. N. 2011, MNRAS, 412, 4

Law, N. M., Morton, T., Baranec, C., et al. 2014, ApJ, 791, 35

Lee, E. J., Chiang, E., Ormel, C.W. 2014, ApJ, 797, 95

Lillo-Box, J, Barrado, D., Buoy, H. 2012, A&A, 546, 10

Lin, D. N. C., Bodenheimer, P., & Richardson, D. C. 1996, Nature, 380, 606

Lockwood, A.C., Johnson, J.A., Bender, C.F., et al. 2014, ApJ, 783, L29

Malmberg, D., Davies, M. B., & Chambers, J. E. 2007, MNRAS, 377, L1

Marois, C., Lafreniere, D., Doyon, R., et al. 2006, ApL, 641, 1

Mayer, L., J. Wadsley, T. Quinn, et al. 2005, MNRAS, 363, 2

McCullough, P. R., Burke, C. J., Valenti, J. A., et al. 2008, arXiv:0805.2921

McLean, I. S., Becklin, E. E., Bendiksen, O., et al. 1998, Proc. SPIE 3354, 566

Nagasawa, M., Ida, S., & Bessho, T. 2008, ApJ, 678, 498

Naoz, S., Farr, W. M., Lithwick, Y., Rasio, F. A., & Teyssandier,J. 2011, Nature, 473, 187

Ngo H., H. A. Knutson, S. Hinkley, et al. 2015, ApJ, 800, 138

Pichardo, B., Sparke, L. S., & Aguilar, L. A. 2005, MNRAS, 359, 521

Pollack, J. , B., O. Hubickyk, P. Bodenheimer, et al. 1996, Icarus, 124, 1.

Pont, F. , H. Knutson, R. L. Gilliland, et al. 2008, MNRAS, 385, 1

Raghavan, D., McAlister, H. A., Henry, T. J., et al. 2010, ApJS, 190, 1

Sing, D. K. , F. Pont, S. Aigrain, et al. 2011, MNRAS, 416, 2

Snellen, I. A. G., de Kok, R. J., de Mooij, E. J. W., & Albrecht, S. 2010, Nature, 465, 1049

Spalding, C. & Batygin, K. 2014, ApJ, 790, 1

Spalding, C., Batygin, K., & Adams, F. C. 2014. ApJL, 797, 2

Spalding, C. & Batygin, K. 2015, ApJ, accepted

Spurzem, R., Giersz, M., Heggie, D.C., et al. 2009, ApJ, 697, 458

Terquem, C. & Bertout, C. 1993, A&A, 274, 291

Teske, J.K., Everett, M.E., Hirsch, L, et al. 2015, accepted to AJ, arXiv:1508.06502

Triaud, A. H. M. J., Collier Cameron, A., Queloz, D., et al. 2010, A&A, 524, A25

Wang, J., Xie, J.-W., Fischer, D. A., et al. 2014, ApJ, 783, 4

Wang, J., Fischer, D. A., Xie, J.-W. et al. 2014, ApJ, 791, 111

Wang, J., Fischer, D.A., Xie, J.-W. et al. 2015, ApJ accepted, arXiv:1510.01964

Welsh, W. F., Orosz, J. A., Carter, et al. 2012, Nature, 481, 475

Winn, J. N., Howard, A. W., Johnson, J. A., et al. 2011, AJ, 141, 63

Woellert, M., Brandner, W., Bergfors, C., et al. 2015, A&A, 575, 23

Woellert, M. & Brandner, W. 2015, A&A, 579, 129

Wright, J. T., G. W. Marcy, A. W. Howard, et al. 2012, ApJ, 753, 2

Wu, Y., & Lithwick, Y. 2010, ApJ, 735, 109

Wu, Y., & Murray, N. 2003, ApJ, 589, 605

Zheng et al. 2015, MNRAS, 453, 2759

Zucker, S., & Mazeh, T. 1994, ApJ, 420, 806

Chapter 3

DIRECT DETECTION OF HOT JUPITER ATMOSPHERES

This chapter is adapted in part from work previously published as

Piskorz, D., B. Benneke, N. Crockett, et al. (2016). *The Astrophysical Journal* **832**.2, 131–139. DOI: 0004-637X/832/2/131.

Since the discovery of 51 Peg b (Mayor & Queloz 1995), the radial velocity (RV) technique has proven indispensable for exoplanet discovery. Hundreds of exoplanets have been revealed by measuring the Doppler wobble of the exoplanet host star (Wright et al. 2012), principally at visible wavelengths. To first order, the RV method yields the period and the minimum mass ($M \sin(i)$) of the orbiting planet. In order to complete the characterization of a given exoplanet, one would want to measure its radius and constrain its atmospheric constituents. Traditionally, this information is accessible only if the planet transits its host star with respect to our line of sight via transmission or secondary eclipse photometry. Successes with these techniques have resulted in the detections of water, carbon monoxide, and methane on the hottest transiting gas giants (Madhusudhan et al. 2014). These gas giants orbit their host stars in days, are known as hot Jupiters, and have an occurrence rate of only 1% in the exoplanet population (Wright et al. 2012). Broadband spectroscopic measurements of transiting hot Jupiter atmospheres are rarely able to resolve molecular bands, let alone individual lines, creating degeneracies in the solutions for atmospheric molecular abundances.

High-resolution infrared spectroscopy has recently provided another route to the study of exoplanet atmospheres, one applicable to transiting and non-transiting planets alike. Such studies capitalize on the Doppler shift between the stellar and planet lines, allowing them to determine the atmospheric compositions, true masses, and inclinations of various systems. With the CRyogenic InfraRed Echelle Spectrograph (CRIRES) at the VLT, Snellen et al. (2010) provided a proof-of-concept of this technique and detected carbon monoxide in the atmosphere of the transiting exoplanet HD 209458 b consistent with previous detections using Hubble Space Telescope data (Swain et al. 2009). By detecting the radial velocity variation of a planet's atmospheric lines in about six hours of observations on single nights,

Target	Telescope/Instrument	Wavelengths (μm)	Result	Reference
51 Peg b	VLT/CRIRES	2.287 - 2.345	CO and H_2O detections	(1)
	ESO/HARPS	0.3781 - 0.6910	H_2O detection	(2)
	VLT/CRIRES	3.1806 - 3.2659	H_2O detection	(3)
55 Cnc e	CFHT/ESPaDOnS	0.5060 - 0.7950	3σ lower limit on H_2O	(4)
HD 179949 b	VLT/CRIRES	2.2875 - 2.3454	CO and H_2O detections	(5)
HD 189733 b	VLT/CRIRES	3.1805 - 3.2659	H_2O detection	(6)
	CRIRES	1.9626 - 2.3452	CO detection	(7)
	CRIRES	2.2875 - 2.3454	Length of day	(8)
	ESO/HARPS	3.8 - 6.9	H_2O detection to 1σ	(9)
HD 209458 b	VLT/CRIRES	2.291 - 2.349	CO and winds detections	(10)
	VLT/CRIRES	2.3215 - 2.325	No temperature inversion	(11)
	VLT/CRIRES	3.947.3 - 4.0443	H_3^+ non-detection	(12)
	VLT/CRIRES, HST/WFC3, SST/IRAC	2.287 - 2.345, 1.125 - 1.655, 3.6, 4.5 & 8.0	C/O < 1 at 3.5σ	(13)
HD 88133 b	Keck/NIRSPEC	2.0 - 2.4, 3.0 - 3.4	H_2O detection	Ch. 4
KELT-2Ab	Keck/NIRSPEC, SST/IRAC	3.0 - 3.4, 3.6 & 4.5	H_2O detection	Ch. 6
tau Boo b	VLT/CRIRES	2.287 - 2.345	CO detection	(14)
	VLT/CRIRES	2.305 - 2.33	CO detection	(15)
	Keck/NIRSPEC	3.0 - 3.4	H_2O detection	(16)
	Keck/NIRSPEC	3.0 - 3.4	Reproduction of (16)	Ch. 4
ups And b	Keck/NIRSPEC	2.0 - 2.4, 3.0 - 3.4	H_2O detection	Ch. 5

Table 3.1: Selection of recent works studying hot Jupiters with ground-based high-resolution spectroscopy and the cross-correlation technique

other works have detected the dayside and nightside thermal spectra of various transiting and non-transiting hot Jupiters, reporting detections of water and carbon monoxide, as well as the presence of winds and measurements of the length of day (Snellen et al. 2010; Rodler et al. 2012; Snellen et al. 2014; Brogi et al. 2012, 2013, 2014, 2016; Birkby et al. 2013; de Kok et al. 2013; Schwarz et al. 2015, Brogi et al. 2016). With HARPS, Martins et al. (2015) observed the reflected light spectrum of 51 Peg b in a similar manner, combining 12.5 hours of data taken over seven nights when the full dayside of the planet was observable. Many of the previous efforts to study hot Jupiters with ground-based high-resolution spectroscopy are summarized in Table 3.1.

Lockwood et al. (2014) studied the hot Jupiter tau Boo b using Keck NIRSPEC (Near InfraRed SPECtrometer), confirmed the CRIRES measurement of the planet's Keplerian orbital velocity, and detected water vapor in the atmosphere of a non-transiting exoplanet for the first time. NIRSPEC was used to observe an exoplanet's emission spectrum over ~2-3 hours each night across multiple epochs, in order to capture snapshots of the planet's line-of-sight motion at distinct orbital phases. In combination with the many orders of data provided by NIRSPEC's cross dispersed echelle format and the multitude of hot Jupiter emission lines in the infrared, Lockwood et al. (2014) achieved sufficient signal-to-noise to reveal the orbital properties of tau Boo b via the Doppler shifting of water vapor lines in its atmosphere.

We pursue multi-epoch observations having planetary features shifted with respect to the star's spectrum and the Earth's atmosphere in order to develop techniques that can eventually be used on more slowly moving planets nearer the habitable zone. For nearly synchronously rotating hot Jupiters, near-infrared emission from the dayside is likely to be most readily detectable. This strategy is fundamentally different from that used at CRIRES to date since we do not allow the planet's signal to move across several pixels on the detector during one night of observations.

In this chapter, we detail our data reduction (Section 3.1), telluric removal method (Section 3.2), cross-correlation procedure (Section 3.3), and multi-epoch likelihood calculation of the planetary velocity (Section 3.4). These are aspects of the direct detection program that are standard for each of the targets. In the chapters following, we continue our Keck NIRSPEC direct detection program with a study of the emission spectra of the hot gas giants HD 88133 b (Chapter 4), ups And b (Chapter 5), and KELT-2Ab (Chapter 6). More detailed information on the codebase is given in the appendices.

3.1 Extraction of 1-D Spectra from NIRSPEC Observations

We flat field and dark subtract the data using a Python pipeline à la Boogert et al. (2002). We extract one-dimensional spectra and remove bad pixels, and calculate a fourth-order polynomial continuum by fitting the data to a model telluric spectrum after the optimal source extraction. For L band data, the wavelength solution (described to the fourth order as $\lambda = ax^3 + bx^3 + cx + d$, x is pixel number and a, b, c, and d are free parameters) is calculated by fitting the data to a model telluric spectrum. However, since telluric lines are generally weaker near 2 μm, the wavelength solution for K band data is calculated by fitting the data to a combination of model telluric and stellar spectra (given that the stellar relative velocity is well known from optical data, and is later confirmed by the cross-correlation analysis described in Section 3.3). We use an adapted PHOENIX model for our model stellar spectrum in the K band (Husser et al. 2013).

We show one order of reduced L band spectra for HD 88133 b in the top panel of Figure 3.1. We fit an instrument profile to the data and save it so that we may apply it to our stellar and planetary models. This instrument profile is similar to the formulation given in Valenti et al. (1995) and is parameterized as a central Gaussian with four left and four right satellite Gaussians, all with variable widths. Often, the best-fit widths of the third and fourth left and right satellite Gaussians are zero.

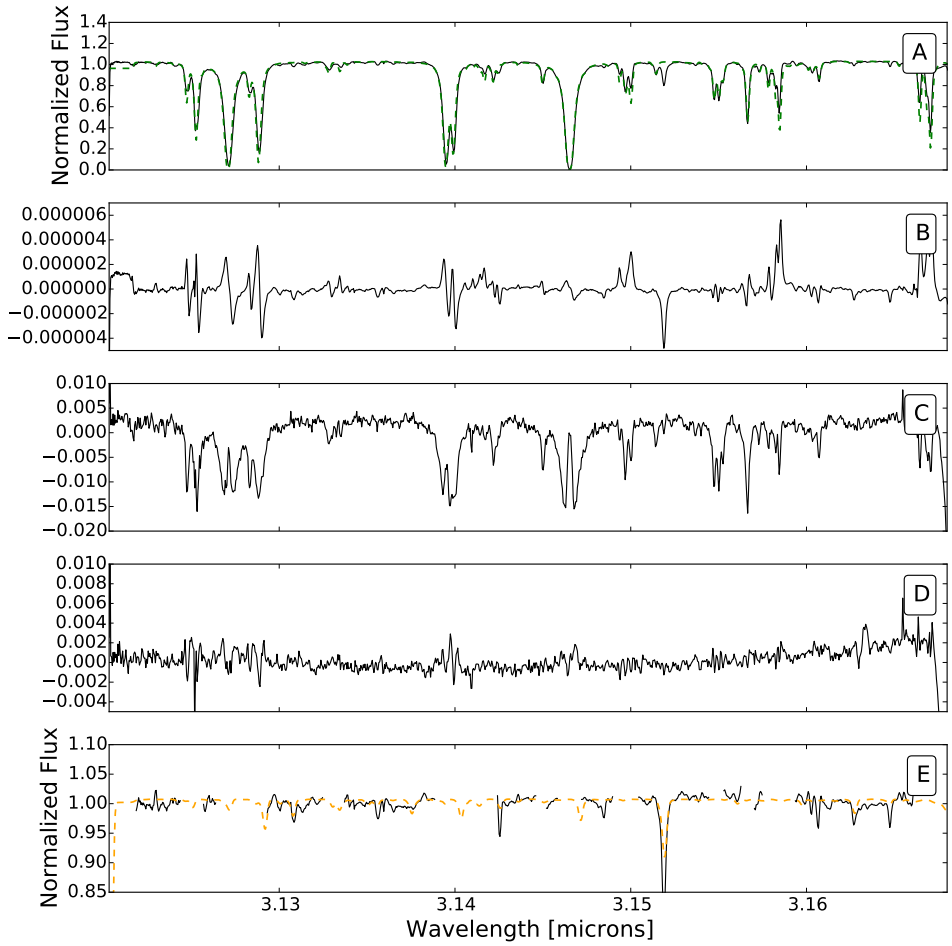

Figure 3.1: The data reduction and telluric correction process. (A): One order of a reduced AB pair of HD 881333 data taken on 2013 March 29 in *L* band, with a best-fit telluric spectrum overplotted with a green, dashed line. (B): The first principal component in arbitrary units of this time series of data which encapsulates changes in the stellar spectrum as the air mass varies during the observation. (C): The second principal component in arbitrary units which describes changes in abundances of telluric species. (D) The third principal component in arbitrary units which encompasses changes in plate scale. (E) Telluric-corrected data with the first five principal components removed shown in black. This is the data used for the cross-correlation analysis described in Section 6.5. Overplotted in orange is the stellar spectrum of HD 88133 adapted from the PHOENIX stellar library (Husser et al. 2013).

Documentation for the NIRSPEC reduction code can be found in Appendix A.

3.2 Telluric Correction with Principal Component Analysis

In this work, we depart from our traditional methods of division by an atmospheric standard (typically an A star, c.f. Boogert et al. 2002) and/or line-by-line telluric

correction (modeling atmospheric abundances with the TERRASPEC software; Bender et al. 2012) in favor of a more automated and repeatable technique: principal component analysis (PCA). This efficient method of telluric correction was also implemented by deKok et al. (2013) in their reduction of CRIRES data on HD 189733 b. PCA rewrites a data set in terms of its principal components such that the variance of the data set with respect to its mean or with respect to a model is reduced. The first principal component encapsulates the most variance; the second, the second most, etc. Over the course of an observation, the telluric components should vary the most as the air mass and atmospheric abundances change, and the planet lines should remain ∼constant. Note that we observe for only 2-3 hours at a time and at a lower resolution than CRIRES, so the planet lines do not smear. For a typical Keplerian orbital velocity of a hot Jupiter, we would have to observe for at least four hours to smear the planet lines across the NIRSPEC detector pixels. To remove the telluric lines and any other time-varying effects, we aim to isolate only the strongest principal components.

To perform the principal component analysis (see `http://stats.stackexchange.com/questions/134282/relationship-between-svd-and-pca-how-to-use-svd-to-perform-pca`), we first reduce our data set in AB pairs and construct a data matrix $\mathbf{X}$ having n rows and m columns, where n is the number of AB pairs and m is the number of pixels (1024 for individual NIRSPEC echelle orders). We linearly interpolate sub-pixel shifts between nods when aligning the AB pairs on the matrix grid, and then calculate the residual matrix $\mathbf{R}$ according to

$$\mathbf{R}_{ij} = \frac{\mathbf{X}_i - M}{\sigma_j}, \tag{3.1}$$

where i is the row number, j is the column number, M is either the mean of X_j or a telluric model, and σ_i is the standard deviation of the values in column j. We guide our principal component analysis with a telluric model for M (rather than the mean of X_j) that uses baseline values for water vapor (see the Caltech Submillimeter Observatory at `http://cso.caltech.edu/tau/`), carbon dioxide (see the Earth System Research Laboratory at Mauna Loa at `ftp://aftp.cmdl.noaa.gov/products/trends/co2/co2_weekly_mlo.txt`), and methane (see the Earth System Research Laboratory at Mauna Loa at `ftp://ftp.cmdl.noaa.gov/data/greenhouse_gases/ch4/in-situ/surface/mlo/ch4_mlo_surface-insitu_1_ccgg_DailyData.txt`) abundances. For L band data, baseline values for ozone from a reference tropical model are also included for the orders ranging from 3.12-3.17 and 3.26-3.31 μm. Next we calculate the covariance matrix $\mathbf{C}$ of our

mean-normalized data such that

$$\mathbf{C} = \frac{\mathbf{R^T R}}{n-1}. \tag{3.2}$$

A singular value decomposition of the covariance matrix is then performed to find the principal components:

$$\mathbf{C} = \mathbf{U S V^T}, \tag{3.3}$$

where $\mathbf{U}$ contains the left singular vectors (or the eigenvectors), $\mathbf{S}$ is a diagonal matrix of the singular values (or the eigenvalues), and $\mathbf{V}$ contains the right singular vectors. The first three eigenvectors, or principal components, for a 3.12-3.17 μm order observation of HD 88133 b taken on 2013 March 29 are shown in Figure 3.1. The first component recovers changes in the total systemic signal with air mass; the second encapsulates changes in abundances of telluric species, resulting in adjustments to line cores and wings; and the third describes changes to the plate scale. Higher order components typically reflect instrumental fringing and other small effects.

We reconstruct the time-varying portion of each AB spectrum by combining the first k principal components of the data set, given by $\mathbf{U}_k\mathbf{S}_k$, where $\mathbf{U}_k$ is the first k columns of $\mathbf{U}$ and $\mathbf{S}_k$ is the k x k upper-left part of $\mathbf{S}$. Rank-k data, $\mathbf{X}_k$, can be built as

$$\mathbf{X}_k = \mathbf{U}_k\mathbf{S}_k\mathbf{U}_k^\mathbf{T}. \tag{3.4}$$

To produce a telluric-corrected spectrum, $\mathbf{X}_{corr,i}$, each row $\mathbf{X}_i$ of $\mathbf{X}$ is divided by its corresponding un-mean normalized row in $\mathbf{X}_{k,i}$:

$$\mathbf{X}_{corr,i} = \frac{\mathbf{X}_i}{\mathbf{X}_{k,i}\sigma_j + M}. \tag{3.5}$$

Finally, we collapse the rows of data in $\mathbf{X}_{corr}$ and clip regions of substantial telluric absorption (>75%). Depending on the order, anywhere between 30 and 60% of the data is removed by clipping out strong features. This results in a single high signal-to-noise spectrum for each night of observations. The final telluric-corrected spectrum for HD 88133 b on 2013 March 29 is given in the final panel of Figure 3.1.

The version of PCA described here diverges from the approach outlined in deKok et al. (2013) which used PCA to determine the eigenvectors making up the light curves in each spectral channel. Our formulation calculates the eigenvectors comprising each observed spectrum. We also guide our principle component analysis with a

telluric model. The equivalent for deKok et al. (2013) would have been to guide the PCA with vectors for air mass, water vapor content, etc.

For data taken in L band, we find that PCA can reliably correct for the Earth's atmosphere for all orders of data. However, for K band data, we cannot effectively remove the dense, optically-thick telluric forest of CO_2 lines in the order spanning from 2.03 - 2.06 μm, and we omit this wavelength range from subsequent analysis.

It is essential to determine the efficacy of PCA in removing telluric signatures and further ensure that we are not removing the planet's signal as well. Since ~99.9% of the variance is explained by the first principal component, we find that the following results are roughly consistent when different numbers of principal components are removed from the data. We calculate the percent variance removed by each component and, if we assume the planet signal is on the order of 10^{-5} of the total signal, then for most cases we would have to remove about fifteen components to delete the planet signal. We have experimented with incrementally removing up to ten principal components as input to the subsequent analysis; we remove the first five principal components from the data presented in Chapters 4-6.

Documentation for the code that removes telluric lines via principal component analysis can be found in Appendix B.

3.3 Two-Dimensional Cross Correlation

Once cleaned, each order of data for each epoch is cross-correlated with the model predictions of the stellar and planetary atmospheres to determine the cross-correlation function (CCF). We use the TODCOR algorithm to produce a two-dimensional array of correlation values for shifts in the velocities of the star and planet (Zucker & Mazeh 1994). Documentation for TODCOR inputs can be found in Appendix C.

For the 1-D case, as described in Zucker (2003), a Doppler-shifted spectrum could be written as

$$f(n) = a_0 g(n - s_0) + d_n, \tag{3.6}$$

where n is the bin number (related to wavelength but calculated such that bin size is constant in velocity-space; see Tonry & Davis 1979), $g(n)$ is a model spectrum, a_0 is the scaling, s_0 is the shift, and d_n is random noise having a standard deviation σ_0. For simplicity, Zucker (2003) assumes, the number of bins N is large (there are no edge effects) and the observed spectrum and model spectrum have zero means. The

data has a standard deviation s_f^2 and the model has a standard deviation s_g^2 so that

$$s_f^2 = \frac{1}{N}\sum_n f^2(n) \tag{3.7}$$

and

$$s_g^2 = \frac{1}{N}\sum_n g^2(n). \tag{3.8}$$

With this notation, the cross-covariance function $R(s)$ is written as

$$R(s) = \frac{1}{N}\sum_n f(n)g(n-s) \tag{3.9}$$

and the cross-correlation function $C(s)$ is written as

$$C(s) = \frac{1}{Ns_f s_g}\sum_n f(n)g(n-s) = \frac{R(s)}{s_f s_g}. \tag{3.10}$$

In testing our models, we find that the correlation coefficient between our stellar and planet models for the two orders spanning from 2.31 - 2.38 μm is generally an order of magnitude higher than the same correlation coefficient in any other order in the *L* or *K* band, and so we omit them from this study. This behavior is due to the strong correlation between stellar and planetary CO at R=30,000. For example, the hot Jupiter host star HD 88133 has an effective temperature of 5438 K and its CO band (and especially the CO band head at 2.295 μm) is extremely prominent. The *K* band data analysis that follows is only performed on the three orders spanning from 2.10 - 2.20 μm. The main absorbers in this region include carbon dioxide and water vapor.

Determining nightly likelihood curves from cross-correlation functions

For each night's observation, we combine the CCF's of each order to produce the maximum likelihood curves. At the location of maximum correlation, we "slice" the 2D-array along the stellar and planetary velocity axes, and convert those cross-correlation curves to nightly maximum likelihood curves. Lockwood et al. (2014) showed that the cross-correlation function related to the log of maximum likelihood. This fact is shown in greater detail in Zucker (2003) and is summarized here for completeness. Likelihood is the probability of a certain outcome or set of observations *D* given an assumed model *M* and is generally defined as

$$L = \prod_n \frac{1}{\sqrt{2\pi\sigma^2}} \exp\left(\frac{-(D(n)-M(n))^2}{2\sigma^2}\right) \tag{3.11}$$

and for this scenario is specifically defined as

$$L = \left(\frac{1}{\sqrt{2\pi\sigma^2}}\right)^N \exp\left(-\sum_n \frac{(f(n) - ag(n-s))^2}{2\sigma^2}\right) \tag{3.12}$$

In equation 3.12, $f(n)$ is the data and $ag(n-s)$ and σ together represent the model which describes the data with a given scaling a, shift s, and standard deviation of error on the measurements σ. As usual, we rewrite equation 3.12 as the log of the likelihood.

$$\log L = -N \log \sigma^2 - \frac{1}{2\sigma^2} \sum_n (f(n) - ag(n-s))^2 - N \log 2\pi. \tag{3.13}$$

The last term of equation 3.13 is constant and can be ignored. We define $\hat{a}$, $\hat{\sigma}$, and $\hat{s}$ as the values of a, σ, and s, which maximize the value of the log likelihood. $\hat{s}$ also maximizes the value of the cross-correlation function $C(s)$ given in equation 3.10. To determine the values of $\hat{a}$ and $\hat{\sigma}$, we solve

$$\left.\frac{\partial \log L}{\partial a}\right|_{\hat{a}} = \frac{1}{\sigma^2} \sum_n -f(n)g(n-s) + \hat{a}g^2(n-s) \equiv 0 \tag{3.14}$$

and

$$\left.\frac{\partial \log L}{\partial \sigma^2}\right|_{\hat{\sigma}^2} = -\frac{N}{\hat{\sigma}^2} + \frac{1}{\hat{\sigma}^3} \sum_n (f(n) - ag(n-s))^2 \equiv 0. \tag{3.15}$$

With the simplifying assumption that $\sum_n g^2(n-s) = \sum_n g^2(n)$, we find that

$$\hat{a} = \frac{\sum_n f(n)g(n-s)}{\sum_n g^2(n)} \tag{3.16}$$

and

$$\hat{\sigma}^2 = \frac{1}{N} \sum_n (f(n) - ag(n-s))^2. \tag{3.17}$$

Next, we rewrite $\hat{a}$ and $\hat{\sigma}$ in terms of the cross-covariance function $R(\hat{s})$ and the cross-correlation function $C(\hat{s})$. $\hat{a}$ is straightforward:

$$\hat{a} = \frac{R(\hat{s})}{s_g^2}. \tag{3.18}$$

$\hat{\sigma}^2$ is derived as follows:

$$\hat{\sigma}^2 = \frac{1}{N} \sum_n f^2(n) - \frac{2\hat{a}}{N} \sum_n f(n)g(n-\hat{s}) + \frac{\hat{a}^2}{N} \sum_n g^2(n-\hat{s}) \tag{3.19}$$

$$\hat{\sigma}^2 = s_f^2 - \frac{2R^2(\hat{s})}{s_g^2} + \frac{R^2(\hat{s})}{s_g^2} \tag{3.20}$$

$$\hat{\sigma}^2 = s_f^2\left(1 - \frac{R^2(\hat{s})}{s_f^2 s_g^2}\right) \tag{3.21}$$

$$\hat{\sigma}^2 = s_f^2(1 - C^2(\hat{s})). \tag{3.22}$$

We can write $\log L$ in terms of $C(\hat{s})$ by substituting equations 3.18 and 3.22 into equation 3.13. First, we substitute for $\hat{\sigma}^2$ and expand the second term.

$$\log L = -N \log\left(s_f^2(1 - C^2(\hat{s}))\right)^{\frac{1}{2}} - \frac{1}{2s_f^2(1 - C^2(\hat{s}))}\sum_n (f(n) - \hat{a}g(n-s))^2 \tag{3.23}$$

$$\log L = -N \log s_f - \frac{N}{2}\log(1 - C^2(\hat{s})) - \frac{1}{2s_f^2(1 - C^2(\hat{s}))}\sum_n (f(n) - \hat{a}g(n-s))^2. \tag{3.24}$$

The first term is constant. Now we must reduce the third term. The third term can be broken into three pieces. The first piece is

$$-\frac{1}{2s_f^2(1 - C^2(\hat{s}))}\sum_n (f^2(n)) = -\frac{NC^2(\hat{s})}{2(1 - C^2(\hat{s}))}. \tag{3.25}$$

The second piece is

$$\frac{1}{2s_f^2(1 - C^2(\hat{s}))}\sum_n (2\hat{a}f(n)g(n-s)) = \frac{NC^2(\hat{s})}{1 - C^2(\hat{s})}. \tag{3.26}$$

The third piece is

$$-\frac{1}{2s_f^2(1 - C^2(\hat{s}))}\sum_n (\hat{a}^2 g^2(n-s)) = -\frac{NC^2(\hat{s})}{2(1 - C^2(\hat{s}))}. \tag{3.27}$$

The sum of these three pieces is zero, so Zucker (2003) concludes that the likelihood and cross-correlation function are related as

$$\log L = -\frac{N}{2}\log(1 - C^2(\hat{s})) + constant. \tag{3.28}$$

Next, we are most interested in the error on $\hat{s}$. The covariance matrix of $\log L$ with respect to each of its parameters is equal to the negative inverse of the Hessian of $\log L$. The square root of the values on the diagonal of the Hessian are the errors on the measurement of each parameter. Zucker (2003) shows that the covariance matrix of $\log L$ is diagonal and the inversion to the Hessian matrix is straight forward. Specifically,

$$\frac{\partial^2 \log L}{\partial \hat{s}^2} = \frac{\hat{a}NR''(\hat{s})}{\hat{\sigma}^2}, \tag{3.29}$$

where $R''(\hat{s})$ is the second derivative of $R(\hat{s})$. The error on $\hat{s}$ is

$$\sigma_s^2 = -\frac{1}{N}\frac{1}{R''(\hat{s})}\frac{\hat{\sigma}^2}{\hat{a}} = -\left(N\frac{C''(\hat{S})}{C(\hat{s})}\frac{C^2(\hat{s})}{1-C^2(\hat{s})}\right)^{-1}. \tag{3.30}$$

Here, the first factor suggests that the more bins of data available, the lower the error on the measurement of $\hat{s}$. The second factor encompasses the sharpness of the cross-correlation (or cross-covariance) peak. A higher (absolute) value for the second derivative of $R(\hat{s})$ or of $C(\hat{s})$ suggests a sharper peak and a smaller error. The third factor is essentially the ratio of the noise ($\hat{\sigma}^2 \propto 1 - C^2(\hat{s})$) to the signal ($\hat{a} \propto R(\hat{s}) \propto C(\hat{s})$). The lower the noise and the higher the signal, the smaller the error on $\hat{s}$.

Zucker (2003) shows that the calculation of the total maximum likelihood of s and σ_s for multiple spectra with the same Doppler shift is analogous to the derivation above. In this case,

$$\log L = -\frac{N}{2}\sum_i \log(1 - C_i^2(s)) \tag{3.31}$$

and $C_i^2(\hat{s})$ is the i-th cross-correlation for a single nights' data. For example, in the L band, there are four distinct orders of data, resulting in four distinct CCF's, so i=[0,1,2,3]. Equations 3.28 and 3.31 are equivalent and give

$$\log(1 - C^2(\hat{s})) = \sum_i \log(1 - C_i^2(s)). \tag{3.32}$$

The left-hand side of equation 3.32 can be rewritten in terms of an effective correlation value called $\mathcal{L}$ and is essentially a likelihood.

$$M\log(1 - \mathcal{L}^2(s)) = \sum_i \log(1 - C_i^2(s)), \tag{3.33}$$

which reduces to

$$(1 - \mathcal{L}^2(s))^M = \prod_i 1 - C_i^2(s) \tag{3.34}$$

and finally

$$\mathcal{L}(s) = 1 - \left(\prod_i 1 - C_i^2(s)\right)^{\frac{1}{M}}. \tag{3.35}$$

This gives the likelihood curve, $\mathcal{L}$ for a single night of data. Analagous to equation 3.30, the error on the peak location of the total maximum likelihood curve is

$$\sigma_s^2 = -\left(MN\frac{\mathcal{L}''(\hat{s})}{\mathcal{L}(\hat{s})}\frac{\mathcal{L}^2(\hat{s})}{1-\mathcal{L}^2(\hat{s})}\right)^{-1}. \tag{3.36}$$

Note, in our implementation, each spectrum is not required to have the same number of bins N.

There are other methods of combining cross-correlation functions, such as a simple average or a weighted average. However, Zucker (2003) explains the benefits of converting $C(\hat{s})$ to $\log L$ or $\mathcal{L}$. The maximum likelihood approach requires no *a priori* knowledge of the scaling a or the signal-to-noise and allows these values to vary amongst the spectra. Zucker (2003) shows that, compared to other methods, the likelihood method more often identifies the correct peaks in the cross-correlation curves (i.e., a histogram of $\hat{s}$ for 1000 simulations having different S/N ratios has the smallest standard deviation compared to a simple average or a weighted average). Additionally, comparing the height of the strongest peak for $\hat{s}$ to that of the other spurious peaks suggests that the peak is more "peaky" for the likelihood method compared to the other methods.

Since the likelihood depends on the square of the cross-correlation function, a side effect of this approach is a lack of dependence on the sign of the scaling a. For the case of $a < 0$, absorption lines would appear as emission lines, but the correct value of s would still be retrieved. This may be troublesome if one is searching for inverted hot Jupiter atmospheres.

For each epoch, we find we can easily retrieve and confirm the stellar velocity in the nightly likelihood curves (created from each order's cross-correlation function). The stellar velocity is given by

$$v_{pri} = v_{sys} - v_{bary} \tag{3.37}$$

and is dominated by the barycentric velocity v_{bary} at the time of observation and the systemic velocity of the target v_{sys}. We are insensitive to the reflex motion of the star, which is on the order of 0.01 km/s. Using equation 3.36 to calculate σ_s (a.k.a. $\sigma_{v_{pri}}$), we find the average error on our measurements of the stellar velocity is 0.2 km/s.

The retrieval of the planet velocity v_{sec} is more complex, and requires combining the data from multiple epochs. Though there are many peaks and troughs in the planetary maximum likelihood curve produced for each night's observation, only one peak per night represents the properly registered correlation of the data with the model planetary spectrum. This is not to say that most of the planetary maximum likelihood peaks are spurious; rather, they are the results of unintended systematic structure in the cross-correlation space.

3.4 Maximum Likelihood Analysis of Planetary Velocity

For each target, we evaluate the most likely value for the line-of-sight orbital velocity K_p by combining the nightly maximum likelihood curves for the planetary velocity according to

$$v_{sec}(f) = -K_p(\cos(f + \omega) + e\cos\omega) + v_{pri}, \tag{3.38}$$

where f is the true anomaly of the planet in its orbit at the time of observation, ω is the longitude of periastron measured from the ascending node, and e is the eccentricity of the orbit. The stellar velocity shift has the opposite sign and its amplitude is K_s, the velocity semi-amplitude measured by radial velocity studies. For circular orbits, Equation 6.1 simplifies to

$$v_{sec}(t_{obs}) = K_p(\sin(\tfrac{2\pi}{P}(t_{obs} - t_{start})) + \phi)) + v_{pri}, \tag{3.39}$$

where t_{obs} is the observation time in Julian date, P is period and ϕ is a phase lag which equals zero when t_{start} is set at quadrature before "transit." We test a range of orbital velocities from -150 to 150 km/s in steps of 1 km/s, and in turn test a range of planet masses and orbital inclinations. In essence, the final likelihood value $\mathrm{ML}(K_p)$ is

$$\mathrm{ML}(K_p) = \sum_i \mathcal{L}_i(K_p|v_{sec}), \tag{3.40}$$

where $\mathcal{L}_i$ is the i-th night's maximum likelihood curve.

Here, calculating the error on K_p is less straightforward than calculating the error on $\hat{s}$. We do not expect equal error bars for all values of K_p since the cross-correlation is affected by different noise due to telluric absorptions and imperfect correction of correlated noise as a function of wavelength. This is especially true when we combine data taken in different bands (L band at 3.0-3.4 μm vs. K band at 2.0-2.4 μm). Therefore, we adopt jackknife error estimation to determine the error bars on K_p and use a Bayes factor to determine the significance of the planet detection. This process is described in detail for each planet detection in the following chapters and is generally described here.

For each target, we create a series of delete-1 jackknife samples (McIntosh 2016 and references therein). This means we remove the first night's data from the full dataset and calculate a new maximum likelihood curve for K_P. Then we remove the second night's data from the full dataset and calculate a new maximum likelihood curve for K_P, etc. If we have six nights of data, we have six jackknife samples. The jackknifed sample with the i-th night of data removed is called X_i and the maximum likelihood

curve resulting from that jackknifed data set is called ML_i. The jackknifed error bars are given by

$$\sigma_{jack} = \sqrt{\frac{n-1}{n}\sum_{i=1}^{n}(\mathrm{ML}_i - \mathrm{ML}_{avg})^2}, \tag{3.41}$$

where n is the number of jackknife samples (or the number of nights) and $\mathrm{ML}_{avg} = \frac{1}{n}\sum_{i=1}^{n}\mathrm{ML}_i$. In other words, the jackknifed error bars are equivalent to $\sqrt{n-1}$ times the standard deviation of the jackknife samples. To check the quality of these error bars, we calculate the reduced chi-squared value as given by

$$\chi^2_{red} = \frac{\chi^2}{\nu}, \tag{3.42}$$

where ν is the number of degrees of freedom (number of observations minus number of parameters). In the cases discussed in the following chapters we find that χ^2_{red} is less than 1, suggesting that the error bars have been overestimated. This can be explained by the fact that there is high variance between jackknife samples, driving a high standard deviation and therefore large error bars.

To determine the significance of the detection, we fit a Gaussian distribution (indicating the presence of a planetary signal) and a flat line (indicating no planetary signal) and calculate the Bayes factor. As in Kass & Raftery (1995), we define the Bayes factor B to be the ratio of likelihoods between two models, in this case the likelihood of the Gaussian distribution compared to the likelihood of the straight line. $2\ln B$ must be greater than 10 for a model to be very strongly preferred. When $2\ln B = 10$, the strength of the detection is 3σ.

Once a value for K_p is determined, the planet's true mass M_p can be calculated with information on the the stellar mass M_s and RV semi-amplitude K_s according to

$$M_p = \frac{M_s K_s}{K_p} \tag{3.43}$$

and the planet's orbital inclination i (measured from face-on) can be calculated from the indicative mass $M\sin i$ according to

$$i = \arcsin\left(\frac{M\sin i}{M_p}\right). \tag{3.44}$$

In the following three chapters, we apply these methods to three non-transiting and one transiting hot Jupiter.

For Table 3.1 only

(1) Brogi, M., Snellen, I.A.G., de Kok, R.J., et al. 2013, ApJ, 767, 1

(2) Martins, J.H.C., Santos, N.C., Figueira, P., et al. 2015, A&A, 576, A134

(3) Birkby, J. L., de Kok, R. J., & Brogi, M. et al. 2017, AJ, 153, 3

(4) Esteves, L.J., de Mooij, E.J.W., Jayawardhana, R. et al. 2017, AJ, 153, 168

(5) Brogi M., de Kok R. J., Birkby J. L., et al. 2014, A&A, 565A, 124B

(6) Birkby, J. L., de Kok, R. J., & Brogi, M. et al. 2013, MNRAS, 436, L35

(7) de Kok R. J., Brogi M., Snellen I. A. G. et al. 2013, A&A, 554, A82

(8) Brogi, M., de Kok, R.J., Albrecht, S. et al. 2016, ApJ, 817, 2

(9) Allart, R., Lovis, C., Pino, L, et al. 2017, A&A, arXiv:1706.00027v1

(10) Snellen, I. A.G., de Kok, R. J., de Mooij,et al. 2010, Nature, 465, 1049

(11) Schwarz, H., Brogi, M., deKok, R.J., et al. 2015, A&A, 579, A111

(12) Lenz, L.F., Reiners, A., Seifahrt, A., et al. 2016, A&A, 589, A99

(13) Brogi, M., Line, M., Bean, J., et al. 2017, ApJL, 839, L2

(14) Brogi, M., Snellen, I.A.G., de Kok, R.J., et al. 2012, Nature, 486, 502

(15) Rodler, F., Lopez-Morales, M., & Ribas, I. 2012. ApJL, 753, L25

(16) Lockwood, A.C., Johnson, J.A., Bender, C.F., et al. 2014, ApJ, 783, L29

For All of Chapter 3

Allart, R., Lovis, C., Pino, L, et al. 2017, A&A, arXiv:1706.00027v1

Birkby, J. L., de Kok, R. J., & Brogi, M. et al. 2013, MNRAS, 436, L35

Birkby, J. L., de Kok, R. J., & Brogi, M. et al. 2017, AJ, 153, 3

Boogert, A. C. A., Blake, G. A., & Tielens, A. G. G. M. 2002, ApJ, 577, 271

Brogi, M., Snellen, I.A.G., de Kok, R.J., et al. 2012, Nature, 486, 502

Brogi, M., Snellen, I.A.G., de Kok, R.J., et al. 2013, ApJ, 767, 1

Brogi M., de Kok R. J., Birkby J. L., et al. 2014, A&A, 565A, 124B

Brogi, M., de Kok, R.J., Albrecht, S. et al. 2016, ApJ, 817, 2

Brogi, M., Line, M., Bean, J., et al. 2017, ApJL, 839, L2

de Kok R. J., Brogi M., Snellen I. A. G. et al. 2013, A&A, 554, A82

Esteves, L.J., de Mooij, E.J.W., Jayawardhana, R. et al. 2017, AJ, 153, 168

Husser, T.-O., Wende-von Berg, S., Dreizler, S., et al. 2013, A&A, 553, A6

Lenz, L.F., Reiners, A., Seifahrt, A., et al. 2016, A&A, 589, A99

Lockwood, A.C., Johnson, J.A., Bender, C.F., et al. 2014, ApJ, 783, L29

Madhusudhan, N., Knutson, H.A., Fortney, J.J., & Barman, T. 2012, Exoplanetary atmospheres. In *Protostars and Planets VI* (H. Beuther et al., eds.), pp. 739-762. Univ. of Arizona, Tuscon.

Martins, J.H.C., Santos, N.C., Figueira, P., et al. 2015, A&A, 576, A134

Mayor, M. & Queloz, D. 1995, Nature, 378, 23

McIntosh, A. 2016, arXiv:1606.00497

Rodler, F., Lopez-Morales, M., & Ribas, I. 2012. ApJL, 753, L25

Schwarz, H., Brogi, M., deKok, R.J., et al. 2015, A&A, 579, A111

Snellen, I. A.G., de Kok, R. J., de Mooij,et al. 2010, Nature, 465, 1049

Snellen, I.A.G., Brandl, B.R., deKok, R.J., et al. 2014, Nature, 503, 63

Swain, M. R. Tinetti, G., Vashisht, G., et al. 2009, ApJ, 704, 1616.

Tonry, J. & Davis, M. 1979, AJ, 420, 806

Valenti, J. A., Butler, R. P., & Marcy, G. W. 1995, PASP, 107, 966

Wright, J. T., G. W. Marcy, A. W. Howard, et al. 2012, ApJ, 753, 2

Zucker, S. & Mazeh, T. 1994, ApJ, 420, 806

Zucker, S. 2003, MNRAS, 342, 1291.

Chapter 4

DIRECT DETECTION OF HD 88133 B'S ATMOSPHERE

This chapter is adapted from work previously published as

Piskorz, D., B. Benneke, N. Crockett, et al. (2016). *The Astrophysical Journal* **832**.2, 131–139. DOI: 0004-637X/832/2/131.

4.1 Introduction

Here, we apply the spectroscopic techniques described in Chapter 3 to directly detect the emission spectrum of the hot gas giant HD 88133 b. This system allows us to test the brightness limits of the method and develop a more robust orbital dynamics model that can be applied to eccentric systems. In Section 4.2 we present new (stellar) radial velocity (RV) observations of HD 88133 and an updated ephemeris. In Section 4.3 we outline our NIRSPEC observations of HD 88133, which is reduced, corrected, and cross-correlated as described in Chapter 3. In Section 4.4 we describe the results cross correlation and maximum likelihood analyses, and present the detection of the thermal spectrum of HD 88133 b. In Section 4.5 we first test our pipeline by reproducing earlier detections of the atmosphere of the hot Jupiter tau Boo b and then we discuss HD 88133 b's atmosphere and future observations.

4.2 HIRES Observations and RV Analysis

The RV measurements of HD 88133 have been made under the purview of the California Planet Survey (CPS; Howard et al. 2010) with the High Resolution Echelle Spectrometer (HIRES; Vogt et al. 1994) at the W.M. Keck Observatory. Seventeen RV measurements of HD 88133 were published in an earlier study (Fischer et al. 2005), and here we extend that data set to 55 individual RV measurements, having a baseline of eleven years (see Table 4.1 and `http://iopscience.iop.org/0004-637X/832/2/131/suppdata/apjaa449ft1_mrt.txt` for the full table). RV data are reduced with the standard CPS HIRES configuration and reduction pipeline (Wright et al. 2004; Howard et al. 2010; Johnson et al. 2010). Doppler shifts are recovered by comparison to an iodine absorption spectrum and a modeling procedure presented in Butler et al. (1996) and Howard et al. (2011). Processed RV data are shown in Figure 4.1.

Julian Date-2440000	Radial Velocity (m/s)	σ_{RV} (m/s)
13014.947812	-21.97	2.03
13015.947488	23.44	2.06
13016.952546	20.55	1.91
13044.088461	21.71	1.63
13044.869410	-24.07	1.46
13045.843414	-31.17	1.42
13046.081308	-19.97	1.52

Table 4.1: Selection of HD 88133 RV Measurements.

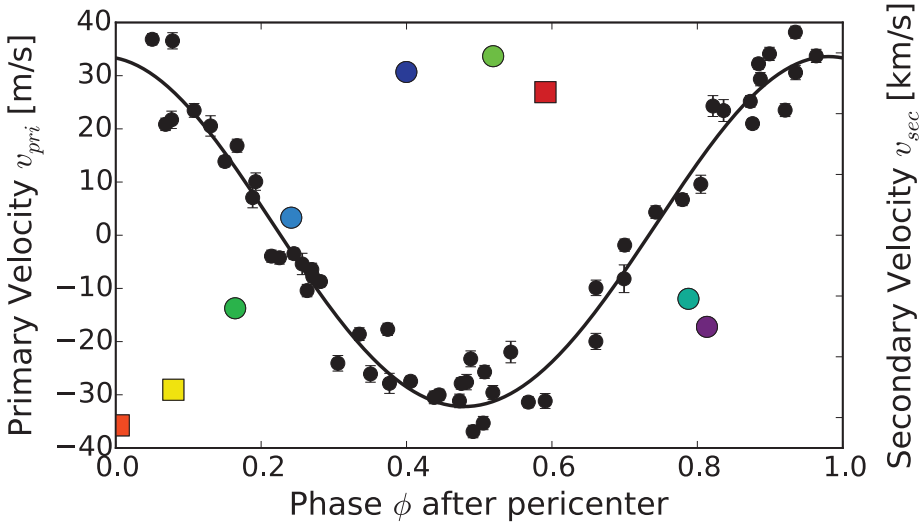

Figure 4.1: RV data from the California Planet Survey with the best-fit stellar RV (primary velocity) curve overplotted in black. The colored points represent the NIRSPEC observations of this planet based on the observation phases and our qualitative expectations of their secondary velocities. In the course of this chapter, we will show that the most likely value for the Keplerian orbital velocity of HD 88133 b is 40 ± 15 km/s.

The RV data are fit with a Markov-Chain Monte Carlo (MCMC) technique following Bryan et al. (2016). Eight free parameters (six orbital parameters: the velocity semi-amplitude K, the period of the orbit P, the eccentricity of the orbit e, the argument of periastron ω, the true anomaly of the planet at a given time f, and the arbitrary RV zero point γ; a linear velocity trend $\dot{\gamma}$; and a stellar jitter term σ_{jitter} as in Isaacson & Fischer 2020) having uniform priors contribute to the model m and are simultaneously fit to the data v. We initiate the MCMC chains at the values published by Fischer et al. (2005), allowing the chains to converge quickly and avoiding degeneracies in e and ω. The likelihood function is given by

$$\mathcal{L} = \frac{1}{\sqrt{2\pi}\sqrt{\sigma_i^2 + \sigma_{jit}^2}} \exp\left(-0.5\left(\frac{(v-m)^2}{\sigma_i^2 + \sigma_{jit}^2}\right)\right), \tag{4.1}$$

where σ_i is the instrument error and σ_{jit} is the stellar jitter. The stellar jitter term is added in quadrature to the uncertainty value of each RV measurement. Best-fit orbital elements indicated by this analysis, as well as other relevant system parameters, are included in Table 4.2, and the best-fit velocity curve is shown in the Figure 4.1. This represents a substantial improvement to the ephemeris originally published in Fischer et al. (2005). We combine these values with the velocities derived by our NIRSPEC analysis described in Chapter 3 to break the $M\sin(i)$ degeneracy for HD 88133 b.

4.3 NIRSPEC Observations

Data were taken on six nights (2012 April 1 and 3, 2013 March 10 and 29, 2014 May 14, 2015 April 8) in L band and three nights (2015 November 21, 2015 December 1, and 2016 April 15) in K band in an ABBA nodding pattern with the NIRSPEC instrument at the W.M. Keck Observatory (McLean et al. 1998). With a 0.4″x24″ slit NIRSPEC has an L band resolution of 25,000 (30,000 in K band). Individual echelle orders cover from 3.4038-3.4565 / 3.2567-3.3069 / 3.1216-3.1698 / 2.997-3.044 μm in the L band and from 2.3447-2.3813 / 2.2743-2.3096 / 2.2085-2.2422 / 2.1464-2.1788 / 2.0875-2.1188 / 2.0319-2.0619 μm in the K band.

A schematic of the planet's orbit during our observations is given in Figure 4.2 assuming the best-fit orbital parameters from our HIRES RV analysis in Section 4.2. Details of our observations are given in Table 4.3. In Table 4.3, S/N$_L$ and S/N$_K$ are calculated at 3.0 μm and 2.1515 μm, respectively. Each S/N calculation is for a single channel (i.e., resolution element) for the whole observation.

Property	Value	Reference
Stellar		
Mass, M_{st}	1.18 ± 0.06 $M_{\odot}$	Mortier et al. (2013)
Radius, R_{st}	1.943 ± 0.064 $R_{\odot}$	Torres et al. (2010)
Effective temperature, $T_{\rm eff}$	5438 ± 34 K	Mortier et al. (2013)
Metallicity, [Fe/H]	0.330 ± 0.05	Mortier et al. (2013)
Surface gravity, $\log g$	3.94 ± 0.11	Mortier et al. (2013)
Rotational velocity, $v \sin i$	2.2 ± 0.5	Mortier et al. (2013)
Systemic velocity, v_{sys}	-3.45 ± 0.119 km/s	Chubak et al. (2012)
K band magnitude, K_{mag}	6.2	Wenger et al. (2000)
Velocity semi-amplitude, K	$32.9^{+1.03}_{-1.03}$ m/s	Section 4.2
RV zero point, γ	$3.08^{+1.51}_{-1.47}$ m/s	Section 4.2
Velocity trend, $\dot{\gamma}$	$-0.0013^{+0.0009}_{-0.0010}$ m/s/yr	Section 4.2
Stellar jitter, σ_{jitter}	$4.68^{+0.51}_{-0.61}$	Section 4.2
Planetary		
Indicative mass, $M \sin(i)$	$0.27^{+0.01}_{-0.01} M_{Jup}$	Section 4.2
Mass, M_p	$1.02^{+0.61}_{-0.28} M_J$	Section 4.4
Inclination, i	$15^{+6}_{-5}{}^{\circ}$	Section 4.4
Semi-major axis, a	0.04691 ± 0.0008 AU	Butler et al. (2006)
Period, P	$3.4148674^{+4.57e-05}_{-4.73e-05}$	Section 4.2
Eccentricity, e	$0.05^{+0.03}_{-0.03}$	Section 4.2
Argument of periastron, ω	$7.22^{+31.39}_{-48.11}{}^{\circ}$	Section 4.2
Time of periastron, t_{peri}	$2454641.984^{+0.293}_{-0.451}$ JD	Section 4.2
Phase uncertainty, $\sigma_{f+\omega}$	6.34°	Section 4.2

Table 4.2: HD 88133 System Properties

Date	Julian Date (- 2,440,000 days)	Mean anomaly M (2π rad)	True anomaly f (2π rad)	Barycentric velocity v_{bary} (km/s)	Int. time (min)	S/N$_{L,K}$
***L* band**						
2012 April 1	16018.837	0.89	0.86	-20.96	140	1680
2012 April 3	16020.840	0.48	0.48	-21.66	140	2219
2013 March 10	16361.786	0.29	0.33	-11.59	180	2472
2013 March 29	16380.726	0.84	0.80	-19.70	150	1812
2014 May 14	16791.796	0.18	0.22	-29.27	120	1694
2015 April 8	17120.835	0.50	0.50	-23.01	160	2938
***K* band**						
2015 November 21	17348.129	0.06	0.68	29.95	60	2701
2015 December 1	17358.117	0.96	0.62	29.25	60	2823
2016 April 15	17493.301	0.54	0.53	-29.15	80	2466

Table 4.3: NIRSPEC Observations of HD 88133 b

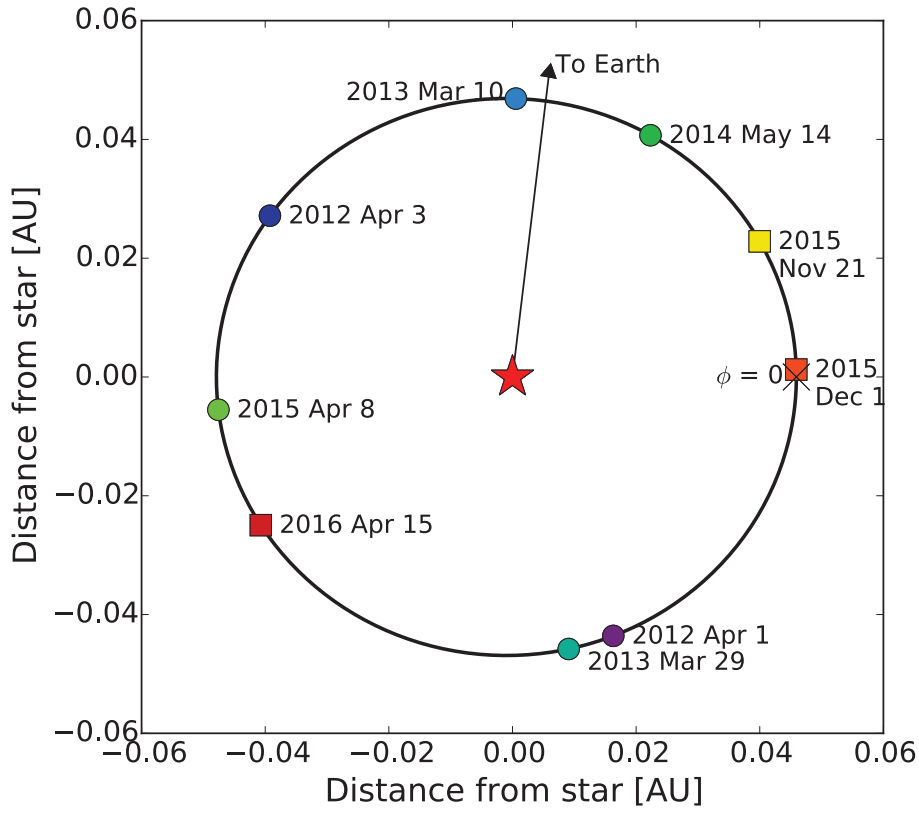

Figure 4.2: Top-down schematic of the orbit of HD 88133 b around its star according to the orbital parameters derived by Fischer et al. (2005), Butler et al. (2005), and this work. Each point represents a single epoch's worth of NIRSPEC observations of the system. Circles indicate L band observations and squares represent K band observations. The black arrow represents the line of sight to Earth.

4.4 NIRSPEC Data Analysis and Results

After reducing our suite of NIRSPEC data on HD 88133 b and after using PCA to remove the strongest components, we have a large, clean set of near-infrared spectra of HD 88133 b. We run a two-dimensional cross-correlation analysis (TODCOR algorithm; Zucker & Mazeh 1994) to find the optimum shifts for the stellar and planetary spectra entwined in our telluric- and instrument-corrected data. This requires accurate model stellar and planet spectra.

Model Stellar Spectrum

Our synthetic stellar spectrum is a PHOENIX model (Husser et al. 2013) interpolated to match the published effective temperature $T_{\rm eff}$, surface gravity $\log g$, and metallicity [Fe/H] of HD 88133 listed in Table 6.1. As HD 88133 has a $v \sin i < 5$ km/s, instrumental broadening dominates, and we convolve the stellar model with

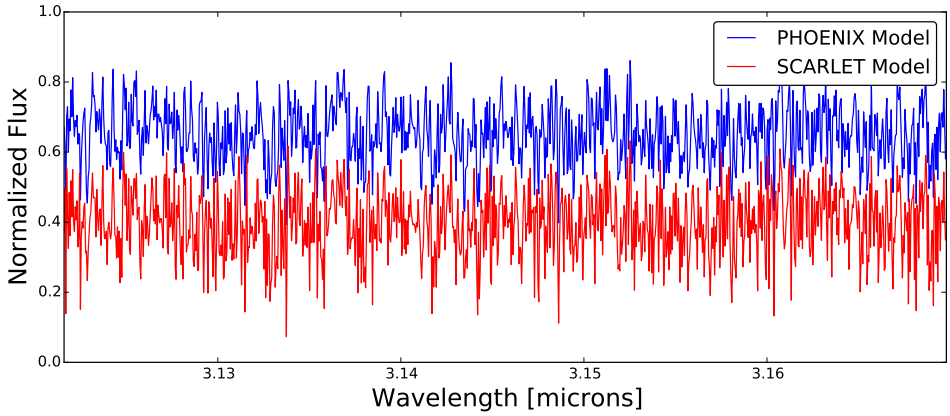

Figure 4.3: Forward models for the planetary atmosphere of HD 88133 b produced by the PHOENIX and SCARLET models drawn at instrument resolution. Note that the flux calculated by the SCARLET model is shifted downward by 0.3 for clarity. Features shown here are principally due to water vapor. The correlation coefficient between these two models at zero-lag is 0.92.

an instrumental profile calculated from the data.

Model Planetary Spectrum

We have computed the high-resolution thermal emission spectrum of HD 88133 b using both the SCARLET (Benneke 2015) and PHOENIX (Barman et al. 2001; Barman et al. 2005) frameworks. An example of one order of our *L* band planet models is shown in Figure 4.3. Both models compute the thermal structure and equilibrium chemistry of HD 88133 b given the irradiation provided by the host star. Models are computed for a cloud-free atmosphere with solar elemental composition (Asplund et al. 2009) at a resolving power of R > 250K, and assume perfect heat redistribution between the day and night sides. The model spectra are subsequently convolved with the instrumental profile derived from the data. We find consistent results for both models despite minor differences in the molecular line lists used.

The SCARLET model considers the molecular opacities of H_2O, CH_4, NH_3, HCN, CO, and CO_2 and TiO from the high-temperature ExoMol database (Tennyson & Yurchenko 2012), and O_2, O_3, OH, C_2H_2, C_2H_4, C_2H_6, H_2O_2, and HO_2 from the HITRAN database (Rothman et al. 2009). Absorption by the alkali metals (Li, Na, K, Rb, and Cs) is modeled based on the line strengths provided in the VALD database (Piskunov et al. 1995) and H_2-broadening prescription provided in Burrows & Volobuyev (2003). Collision-induced broadening from H_2/H_2 and H_2/He collisions is computed following Borysow (2002).

Unlike SCARLET, PHOENIX is a forward modeling code that converges to a solution based on traditional model atmosphere constraints (hydrostatic, chemical, radiative-convective, and local thermodynamic equilibrium) for an assumed elemental composition. The PHOENIX model uses similar opacities as SCARLET (for example, most of the latest linelists from ExoMol and HITRAN). Additional line data for metal-hydrides come from Dulick et al. (2003) (and references therein). Broadening of alkali lines follows Allard et al. (2003). These differences are of only minor importance for this study because SCARLET and PHOENIX use the same water linelist and water opacity dominates the spectral features across the spectral range of our observations (Figure 4.3).

Based on the effective temperatures of the planet and the star, the photometric contrast α_{phot} (defined as the ratio of the planet flux to the stellar flux) is on the order of 10^{-4}. This is also a rough upper bound for the spectroscopic contrast α_{spec}. Since the cross-correlation analyses described in Section 3.3 are not very sensitive to contrast ratios, varying the value of α_{spec} does not change our conclusions on the radial velocity of the planet, and thus the system inclination (Lockwood et al. 2014). However, the specific value of α_s does affect our conclusions on the composition and structure of the planet's atmosphere. That is, the overall velocity structure of the cross-correlation surface is not much affected by α_{spec}, though the size and structure of the final maximum likelihood peak near the planet's signature will be.

Results of 2-D Cross-Correlation Analysis

We run a 2D cross correlation analysis on the data set for HD 88133 b with the stellar and planetary models for the target. The results of the TODCOR algorithm (Zucker & Mazeh 1994) for the are shown in Figure 4.4.

Planet Mass and Orbital Solution

When the six maximum likelihood curves produced from *L* band data (panels B-G in Figure 4.4) are combined with equal weighting according to Eq. 3.38, we see that the most likely value for the radial projection of the planet's Keplerian orbital velocity K_P is 41 ± 16 km/s. Figure 4.5 shows the maximum log likelihood versus the planet's Keplerian orbital velocity. These error bars are calculated as in Lockwood et al. (2014) by fitting a Gaussian to the likelihood peak and reporting the value of σ, assuming all the points on the maximum likelihood curve are equally weighted. We deduce that the peak in the likelihood curve based on the PHOENIX model at ~60 km/s does not represent the planet's velocity, and we prove this in Section 4.5. The

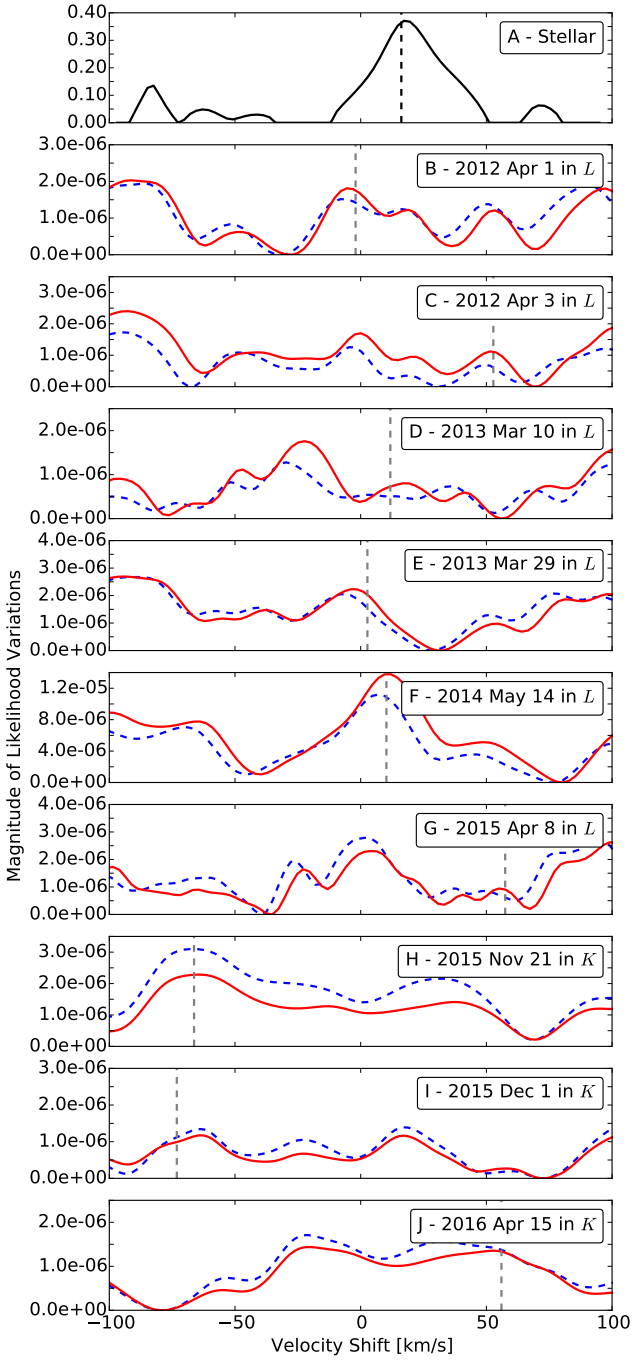

Figure 4.4: Maximum likelihood functions for each observational epoch. (A): Maximum likelihood function of the stellar velocity shift of data taken on 2013 March 29. The black vertical dashed line indicates the expected stellar velocity shift. (B) - (G): Maximum likelihood function of v_{sec} for L band data from 3.0-3.4 μm taken on 2012 April 1 and 3, 2013 March 10 and 29, 2014 May 14, and 2015 April 8, respectively. (H) - (J): Maximum likelihood function of v_{sec} for K band data from 2.10-2.20 μm taken on 2012 November 21, 2015 December 1, and 2016 April 15, respectively. Note in (B) - (J), the blue dashed curve shows the maximum likelihood function for the PHOENIX model, the red curve shows the maximum likelihood function for the SCARLET model, and the grey vertical dashed lines indicate the planetary velocity shift on that date given an orbital solution having K_P = 40 km/s. Based on $\sigma_{f+\omega}$, the error on the calculated planetary velocity shift is about 1.2 km/s.

same calculation applied to the three nights of K band data (panels H-J in Fig. 4.4) suggests that K_P is 32 ± 12 km/s.

The combination of all nine nights of data yields K_P = 40 ± 15 km/s. It is this value of K_P that we use to calculate the secondary velocity curve shown in the bottom panel of Figure 4.2. The peak near K_P = 40 km/s is consistent between the two planet models cross-correlated with the data. Here, given the full suite of data, we calculate error bars on the individual points with jackknife sampling. One night's worth of data is removed from the sample and the maximum likelihood calculation is repeated. The standard deviation of each point amongst the resulting eight maximum likelihood curves is proportional to the error bars on each point on the maximum likelihood curve.

We note that error bars calculated by jackknife sampling and shown in Figure 4.5 are merely an estimate. In fact, for the Gaussian fit, the reduced chi-squared value (chi-squared divided by the number of degrees of freedom) is 0.1, indicating that the error bars are overestimated. This can be explained by the fact that there is high variance between jackknife samples, driving a high standard deviation and therefore large error bars. To examine this behavior further, we fit a Gaussian distribution (indicating the presence of a planetary signal) and a flat line (indicating no planetary signal) and determine the significance of the signal. As in Kass & Raftery (1995), we define the Bayes factor B to be the ratio of likelihoods between two models, in this case the likelihood of the Gaussian distribution compared to the likelihood of the straight line. $2\ln B$ must be greater than 10 for a model to be very strongly preferred.

For the Gaussian distribution compared the the straight line, $2\ln B$ is nearly 10.2, indicating the the Gaussian approximation to the signal at 40 km/s is stronger than a flat line at a level of 3.2σ. Combining K_P with the parameters given in Table 6.1, a K_P of 40 ± 15 km/s implies that the true mass of HD 88133 b is $1.02^{+0.61}_{-0.28} M_J$ and its orbital inclination is $15^{+6}_{-5}{}^{\circ}$.

Note that the values of v_{sec} implied by the most likely value of K_P often, but do not always, correspond with peaks in the maximum likelihood curves for each night, as indicated by the vertical grey dashed lines in Figure 4.4. Especially for nights having a small line-of-sight velocity, planetary lines may be lost in the telluric and/or stellar cross correlation residuals.

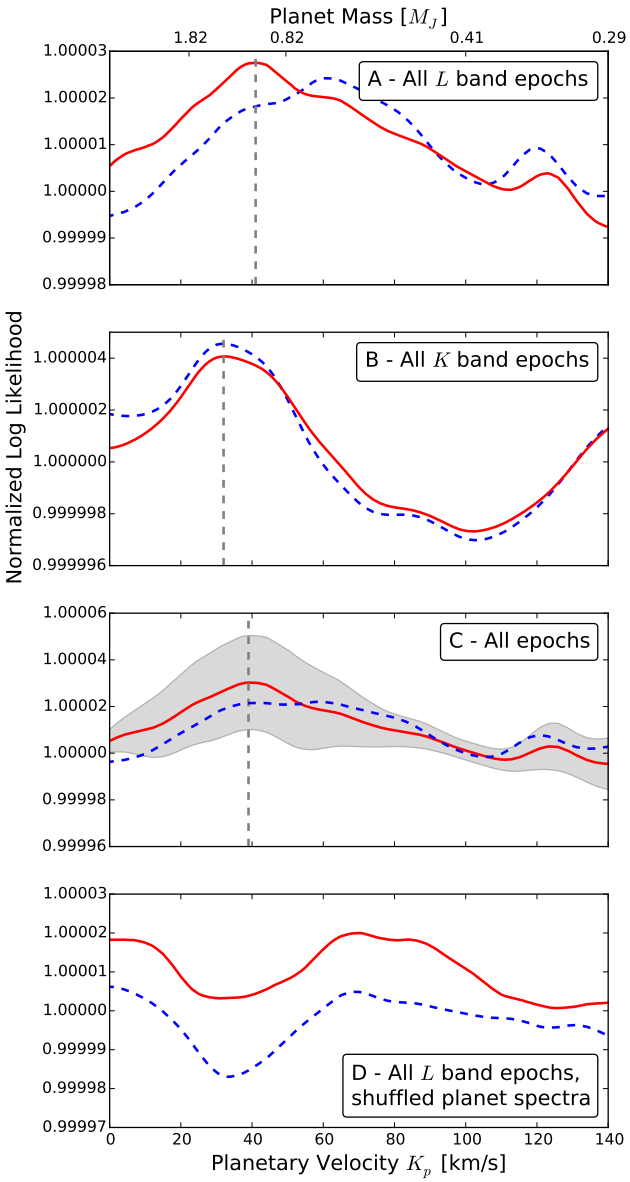

Figure 4.5: Normalized log likelihood as a function of Keplerian orbital velocity K_P. Note that the vertical axes cannot be directly compared, and the color scheme is the same as Figure 4.4. (A): Normalized log likelihood curve for six nights of L band data from 3.0-3.4 μm. (B): Normalized log likelihood curve for three nights of K band data from 2.10-2.20 μm. (C): Normalized log likelihood for all epochs and orders of NIRSPEC data used in panels (A) and (B). The grey region represents the one-sigma error bars determined by jackknife sampling for data cross-correlated with the SCARLET model. (D): Normalized log likelihood curve for six nights of L band data cross-correlated with shuffled planetary spectra.

4.5 Discussion

Tests of the Orbital Solution

We first check our detection of HD 88133 b's emission spectrum at a K_P of 40 km/s by varying the spectroscopic contrast α_{spec} uniformly with orbital phase. We tested nine values of α_{spec} from 10^{-7} to 10^{-3}, and find the maximum likelihood peak near 40 km/s is robust for $\alpha_{spec} \geq 10^{-5.5}$.

We create a "shuffled" planetary model by randomly rearranging chunks of each planetary atmosphere model. If the maximum likelihood peak at 40 km/s is real, then cross correlating our data with a "shuffled" planetary model (which has no coherent planet information) should show little to no peak at the expected K_P. And, indeed, the data-"shuffled" planetary model cross-correlation shows no peak at 40 km/s while the peak at $\sim$ 60 km/s remains for the PHOENIX model (see Panel D of Figure 4.5).

We also check our results by varying the orbital elements of the system. We obtain roughly the same values for Keplerian orbital velocity (within the error bars) for various combinations of eccentricities down to $\sim$ 0 and arguments of perihelion within 20° of the reported value. Our results are most sensitive to these orbital elements as they affect the calculations of the true anomaly and secondary velocity, and therefore the positions of the dashed vertical lines in each epoch's maximum likelihood curve shown in Figure 4.4. Even with a different ephemeris, so long as the dotted vertical lines are near their current peaks, we obtain a comparable final result for the Keplerian orbital velocity of the system.

We note that as HD 88133 b's orbit is slightly eccentric, it is not truly tidally locked. Calculations following Hut (1981) suggest that the planet spins about 10% faster than synchronous. Our strategy prefers that the planet be tidally locked so that as much of the planet's (dayside) emission as possible is captured when the planet has a high line-of-sight velocity relative to the star.

Finally, we have reprocessed the tau Boo b data published by Lockwood et al. (2014) with the methods presented in Chapter 3. The specific departure from Lockwood et al. (2014) is the use of principal component analysis to correct for telluric features in the data (Section 3.2). Our analysis of five nights of L band data recovers a projected Keplerian orbital velocity of 121 ± 8 km/s, a mass of $5.39^{+0.38}_{-0.24} M_J$, and an orbital inclination of $50^{+3}_{-4}{}^{\circ}$ for tau Boo b. This is in good agreement with Lockwood et al. 2014 (K_P=111±5 km/s) as well as Brogi et al. 2012 (K_P=110±3.2 km/s) and Rodler et al. 2012 (K_P=115±11 km/s), thereby validating our PCA-based methods.

Observation Notes

The peak in log likelihood produced solely from *L* band data (panel A of Figure 4.5) is an order of magnitude larger than the peak produced solely from *K* band data, though the values of K_P preferred by each data set are consistent. Though the single channel signal-to-noise ratio for our data is greater in the *K* band than in the *L* band, we only observe HD 88133 in *K* for three nights and only use three orders of data in our final cross-correlation analysis whereas we observe in *L* for six nights and use all four orders of data. Furthermore, six nights of *L* band observations on Keck yields an aggregate shot noise of $\sim$ 800,000 for all epochs and all wavelength bins, suggesting that the detection of a planet having a spectroscopic contrast down to 10^{-5} is feasible.

Additionally, we attempt to detect the planet's CO band near 2.295 μm, and find that effectively separating the stellar spectrum from the planet's is a complex process. Future observations should consider avoiding the CO band head and focusing on the CO comb (low- to moderate- angular momentum P and R branches) itself, particularly the regions between the stellar lines where shifted planetary CO should be present. These intermediate regions have Δv $\sim$ 60 km/s, which is certainly sufficient for the detection of shifted planetary CO and especially so given the high resolution of the next generation of cross dispersed infrared echelle spectrographs, including iSHELL and the upgraded CRIRES and NIRSPEC instruments.

The Spectrum of HD 88133

We took the opportunity during our reprocessing of the tau Boo b data to evaluate the required accuracy of the stellar model. The original Lockwood et al. (2014) analysis was performed with a stellar spectrum using a MARCS solar model with adjustments made to specific line parameters. We re-run the analysis with a PHOENIX model for tau Boo. The correct stellar velocity at each observation epoch is still recovered and the final result for the planet's K_P remains unchanged. This suggests that, for the sake of detecting the planet's spectrum and thus the planet's velocity, a detailed model of the star is not necessarily required; however a refined stellar spectrum will be critical for learning about the planet's atmosphere in detail.

The Atmosphere of HD 88133 b

Acquisition of both *L* and *K* band NIRSPEC data provides a unique opportunity to constrain the atmosphere of HD 88133 b. Generally, the spectroscopic contrast is dominated by water vapor in the *L* band and by carbon monoxide and other species

in the K band. Ultimately, the shape of the log likelihood peak in Figure 4.5 will provide information about the structure of the atmosphere (e.g., Snellen et al. 2010 and Brogi et al. 2016) and even information about the planet's rotation rate (e.g., Snellen et al. 2014 and Brogi et al. 2016).

We do not presently consider orbital phase variations in atmosphere dynamics, radiative transfer, and the resulting spectral signatures from the day to night sides of the hot Jupiter.

4.6 Conclusion

We report the detection of the emission spectrum of the non-transiting exoplanet HD 88133 b using high resolution near-infrared spectroscopy. This detection is based on the combined effect of thousands of narrow absorption lines, predominantly water vapor, in the planet's spectrum. We find that HD 88133 b has a Keplerian orbital velocity of 40 ± 15 km/s, a true mass of $1.02^{+0.61}_{-0.28} M_J$, and a nearly face-on orbital inclination of $15^{+6\,\circ}_{-5}$.

4.7 References

Allard, N. F.,Allard, F., Hauschildt, P. H., Kielkopf, J. F., & Machin, L. 2003, A&A, 411, L473

Asplund, M., Grevesse, N., Suval, J.A., Scott, P. 2009, ARAA, 47, 1

Barman, T. S., Hauschildt, P. H., & Allard, F. 2001, ApJ, 556, 885

Barman, T. S., Hauschildt, P. H., & Allard, F. 2005, ApJ, 632, 1132

Benneke, B. 2015, arXiv:1504.07655

Borysow, A. 2002, A&A, 390, 4

Brogi, M., de Kok, R.J., Albrecht, S. et al. 2016, ApJ, 817, 2

Bryan, M.L., Knutson, H.A., Howard, A.W., et al. 2016, ApJ, 821, 2

Burrows, A., & Volobuyev, M. 2003, ApJ, 583, 985

Butler R. P., Marcy G. W., Williams E. et al 1996 PASP 108 500

Butler, R.P., Wright, J.T., Marcy, G.W., et al. 2006, ApJ, 646, 505

Chubak C., Marcy G., Fischer D. A. et al. 2012, arXiv:1207.6212

Dulick, M., Bauschlicher, C. W., Jr., Burrows, A., et al. 2003, ApJ, 594, 1

Fischer, D.W., Laughlin, G., Butler, P., et al. 2005, ApJ, 620, 481.

Howard A. W., Johnson J. A., Marcy G. W. et al. 2010, ApJ, 721, 1467

Howard A. W., Johnson J. A., Marcy G. W. et al. 2011, ApJ, 730, 10

Isaacson H. & Fischer D. 2010, ApJ, 725, 875

Johnson J. A., Howard A. W., Marcy G. W. et al. 2010, PASP, 122, 888

Kass, R.E., & Raftery, A.E. 1995, JASA, 90,773

Lockwood, A.C., Johnson, J.A., Bender, C.F., et al. 2014, ApJ, 783, L29

McLean, I. S., Becklin, E. E., Bendiksen, O., et al. 1998, Proc. SPIE 3354, 566

Mortier, A., Santos, N.C., Souse, S.G., et al. 2013, A&A, 557, A70

Piskunov, N. E., Kupka, F., Ryabchikova, T. A., Weiss, W. W., & Jeffery, C. S. 1995, A&A S, 112, 525

Rothman, L.S., Gordon, I.E., Barbe, A., et al. 2009, J. Quant. Spectrosc. Radiat. Transfer, 110, 533

Snellen, I. A.G., de Kok, R. J., de Mooij, E. J. W., & Albrecht, S. 2010, Nature, 465, 1049

Snellen, I.A.G., Brandl, B.R., deKok, R.J., et al. 2014, Nature, 503, 63

Tennyson, J., & Yurchenko, S. N. 2012, MRNAS, 425, 21

Torres, G., Bakos, G. A., Hartman, J., et al. 2010, ApJ, 715, 458

Vogt S. S., Allen S. L., Bigelow B. C. et al. 1994, Proc. SPIE, 2198, 362

Wenger, M., Ochsenbein, F., Egret, D. et al. 2000, A&AS, 143, 1

Wright J., Marcy G. W., Butler R. P. and Vogt S. S. 2004, ApJS, 152, 261

Zucker, S. & Mazeh, T. 1994, ApJ, 420, 806

Chapter 5

DIRECT DETECTION OF UPS AND B'S ATMOSPHERE

This chapter is adapted from work previously published as

Piskorz, D., B. Benneke, N. Crockett, et al. (2017). *The Astronomical Journal* **154**.2, 78–86. DOI: 10.3847/1538-3881/aa7dd8.

5.1 Introduction to the upsilon Andromedae system

We now apply the direct detection method described in Chapter 3 to the unique upsilon Andromedae system and its hot Jupiter ups And b.

The first exoplanet in the upsilon Andromedae system was discovered in 1997 with the radial velocity (RV) technique (Butler et al. 1997). Two more years of RV observations revealed the presence of two additional planets in the system, making ups And the first multiple exoplanet system discovered around a main sequence star (Butler et al. 1999). Three planets orbit the F star ups And A: (1) ups And b, a hot Jupiter with a minimum mass of $0.71 M_J$ and a period of 4.617 ± 0.0003 days, (2) ups And c, a gas giant with a minimum mass of $2.11 M_J$ orbiting with a period of 241.2 ± 1.1 days and an eccentricity of 0.18 ± 0.11, and (3) ups And d, another gas giant having a minimum mass of $4.61 M_J$ orbiting with a period of 1266.6 ± 30 days and an eccentricity of 0.41 ± 0.11. Adding to the intrigue, in 2002, a red dwarf companion ups And B with a projected separation of 750 AU from ups And A was detected and determined to have negligible effects on RV observations (Lowrance et al. 2012).

This unique assemblage spurred a torrent of investigations into the origin and stability of the system, a few of which we mention here. Adams & Laughlin (2006) showed that the inclusion of general relativity was required to explain the short period and small eccentricity of ups And b. Were it not for general relativity, ups And b would precess slowly and its eccentricity would be pumped by the massive outer planets. Depending on the mutual inclinations of the planets in the system, it is possible that the Kozai-Lidov mechanism is responsible for the short-period orbit of ups And b (Nagasawa et al. 2008), while Lissaeur & Rivera (2001) suggested that the present-day dynamics of ups And b may be detached from that of the outer planets. Chiang & Murray (2002) suggested that if the orbital planes of ups And c

and d were coplanar and locked in an apisidal resonance, then the eccentricity of ups And d would be pumped over time as the apsidal resonance damped. Once the apsides are aligned, secular interactions would cause eccentricity to be transferred from ups And d to ups And c. Barnes & Greenberg (2006) determined that ups And c and d lie near the separatrix between libration and circulation, though this behavior could not be explained by planet-planet scattering (Barnes & Greenberg 2007).

For lack of complete ephemerides, many of these works assumed the planets' minimum masses were their true masses in their models, and therefore that the system was coplanar. A notable exception was Rivera & Lissaeur (2000) who concluded that scattering or ejections is a likely cause of the outer planets' high eccentricities. In all, one statement can summarize many of these works: the ups And A system is on the edge of instability.

Determining the masses and inclinations of ups And A's planets is critical for realistic interpretations of the system's origin and stability. Five 24 μm Spitzer observations of ups And b suggested $i_b > 30°$ (Harrington et al. 2006). To that, Crossfield et al. (2010) added seven individual and twenty-eight continuous hours of 24 μm Spitzer observations to further constrain $i_b > 28°$. This work also reported that the flux maximum for ups And b occurred 80° before opposition, an observation inconsistent with atmospheric circulation models.

McArthur et al. (2010) used a combination of high-precision astrometry taken with the Fine Guidance Sensor on the Hubble Space Telescope and a large RV data set (974 observations taken over fourteen years) to determine all the orbital elements of ups And c and d and provide some insight into the orbital elements of ups And b. ups And c was shown to have a mass of 14M_J and inclination of 8° from face-on while ups And d has a mass of 10M_J and an inclination of 24° from face-on. (See Table 5.1 for all reported orbital elements with error bars. Note that we calculate argument of periastron from the values of longitude of periastron and longitude of ascending node reported in McArthur et al. 2010. We calculate the error bars on the longitude of periastron by combining the reported error bars on argument of periastron and longitude of ascending node in quadrature.) The mutual inclination of ups And c and d is about 30°. McArthur et al. (2010) made no astrometric detection of ups And b, indicating that its inclination must be greater that 1.2°. They also postulated the presence of a fourth planet in the system in resonance with the third planet and determined that the stellar companion ups And B was indeed bound with a true separation of $\sim$ 9900 AU. The existence of the fourth

planet ups And d was further supported by Curiel et al. (2011). A non-Newtonian simulation of the system suggested that ups And b had an inclination less than ~60° or greater than ~135°.

Drawing on the results of McArthur et al. (2010), Dietrick et al. (2015) ran post-Newtonian numerical simulations of the system to determine which masses and inclinations of ups And b would allow the system as a whole to be stable. The system has a general "region of stability" when $i_b < 40°$. Specifically, Dietrick et al. (2015) investigated four stable, prograde simulations having $i_b < 25°$, but precise conclusions on the mass and inclination of the innermost planet have eluded astronomers.

As described in the two previous chapters, ground-based high-resolution spectroscopy techniques have successfully broken the degeneracy between mass and inclination for non-transiting planets and would be ideal for determining the mass and inclination of ups And b. These techniques treat the target star and its planet as if they were a spectroscopic binary, teasing out the line-of-sight Keplerian velocity of the planet as it orbits the star. Observers using CRIRES (e.g., Snellen et al. 2010) or HARPS (e.g., Martins et al. 2015) tend to allow the planet lines to smear across the detector over the course of many hours. Observers using NIRSPEC (e.g., Lockwood et al. 2014) take up to two hour long snapshots of the planet's emission spectrum at various phases of the planet's orbit. Since NIRSPEC has a resolution of 25,000-30,000 at the observed wavelengths, planet lines generally do not smear across pixels during a 2-3 hour observation. Owing to NIRSPEC's cross-dispersed echelle format, this method yields many planet lines spread over many orders, producing sufficient signal-to-noise to detect the planet's atmosphere.

In this chapter, we use NIRSPEC observations and the methods presented in Chapter 3 and Piskorz et al. (2016) to discern the true mass, inclination, and atmospheric composition of the hot Jupiter ups And b. An important divergence from the method presented in Piskorz et al. (2016) is the inclusion of K band data taken with two different echelle settings, accessing planetary features across the full K band. In Section 5.2, we detail our NIRSPEC observations, data reduction, and telluric correction, while Section 5.3 describes the cross-correlation analysis and maximum likelihood calculation of the orbital solution for ups And b. In Section 5.4, we discuss the robustness of our orbital solution, the long-term stability of the ups And A system, insights into the atmosphere of ups And b, and give some notes on the observations.

Property	Value	Reference
μ **And A**		
Mass, M_{st}	1.31 ± 0.02 $M_{\odot}$	Takeda et a l. (2007)
Radius, R_{st}	1.64 $^{+0.04}_{-0.05} R_{\odot}$	Takeda et a l. (2007)
Effective temperature, $T_{\rm eff}$	6213 ± 44 K	Valenti & Fischer (2005)
Metallicity, [Fe/H]	0.13 ± 0.07	Gonzalez & Laws (2007)
Surface gravity, $\log g$	4.25 ±0.06	Valenti & Fischer (2005)
Rotational velocity, $v \sin i$	9.62 ± 0.5 km/s	Valenti & Fischer (2005)
Systemic velocity, v_{sys}	-28.59 km/s	Nidever et al. (2002)
K band magnitude, K_{mag}	2.86 ± 0.08	van Belle & von Bruan (2009)
μ **And b**		
Velocity semi-amplitude, K	70.51 ± 0.37 m/s	McArthur et al. (2010)
Line-of-sight orbital velocity, K_P	55 ± 9 km/s	This work
Indicative mass, $M \sin(i)$	0.69 ± 0.02M_J	McArthur et al. (2010)
Mass, M_p	1.7 $^{+0.33}_{-0.24}$ M_J	This work
Inclination, i	24 ± 4°	This work
Semi-major axis, a	0.0594 ± 0.0003 AU	McArthur et al. (2010)
Period, P	4.617111 ± 0.000014 d	McArthur et al. (2010)
Eccentricity, e	0.012 ± 0.005	McArthur et al. (2010)
Argument of periastron, ω	44.11 ± 25.56°	McArthur et al. (2010)
Time of periastron, t_{peri}	2450034.05 ± 0.33 JD	McArthur et al. (2010)
Phase uncertainty, $\sigma_{f+\omega}$	0.9°	This work
μ **And c**		
Mass, M_p	13.98 $^{+2.3}_{-5.3} M_J$	McArthur et al. (2010)
Inclination, i	7.868 ± 1.003°	McArthur et al. (2010)
Semi-major axis, a	0.8259 ± 0.043 AU	McArthur et al. (2010)
Period, P	240.9402 ± 0.047 d	McArthur et al. (2010)
Eccentricity, e	0.245 ± 0.006	McArthur et al. (2010)
Argument of periastron, ω	10.81 ± 7.73°	McArthur et al. (2010)
Longitude of periastron,ϖ	247.66 ± 1.76°	McArthur et al. (2010)
Longitude of ascending node, Ω	236.85 ± 7.53°	McArthur et al. (2010)
Time of periastron, t_{peri}	2449922.53 ± 1.17 JD	McArthur et al. (2010)
μ **And d**		
Mass, M_p	10.25 $^{+0.7}_{-3.3} M_J$	McArthur et al. (2010)
Inclination, i	23.758 ± 1.316°	McArthur et al. (2010)
Semi-major axis, a	2.53 ± 0.014 AU	McArthur et al. (2010)
Period, P	1281 ± 1.055 d	McArthur et al. (2010)
Eccentricity, e	0.316 ± 0.006	McArthur et al. (2010)
Argument of periastron, ω	248.92 ± 3.55°	McArthur et al. (2010)
Longitude of periastron, ϖ	252.99 ± 1.31°	McArthur et al. (2010)
Longitude of ascending node, Ω	4.07 ± 3.30°	McArthur et al. (2010)
Time of periastron, t_{peri}	2450059.38 ± 3.50 JD	McArthur et al. (2010)

Table 5.1: ups And System Properties

5.2 NIRSPEC Observations and Data Reduction

Observations

We used NIRSPEC (Near InfraRed SPECtrometer; McLean et al. 1998) at Keck Observatory to observe ups And A and b on seven nights (2011 September 6, 7, and 9, 2013 October 27 and 29 and November 7, and 2014 October 7) in L, three nights (2016 September 19, November 12, and December 15) in K_r (the **right**, long-wavelength half of the dispersed, K-band filtered light), and three nights (2014 October 5 and 2016 August 21 and September 19) in K_l (the **left**, short-wavelength half of the dispersed, K-band filtered light). We obtained spectral resolutions of ~25,000 in L and ~30,000 in K using the 0.4"x24" slit setup and used an ABBA nodding pattern during data acquisition. In L band, the echelle orders typically cover 3.4038-3.4565 / 3.2467-3.3069 / 3.1193-3.1698 / 2.995-3.044 μm. The echelle orders in K_r band typically cover 2.38157-2.41566 / 2.31-2.34284 / 2.24245-2.27485 / 2.17894-2.20861 / 2.11878-2.14639 / 2.06170-2.08703 μm, while in K_l band the echelle orders typically cover 2.34238-2.37535 / 2.27198-2.30374 / 2.20554-2.23653 / 2.14362-2.17298 / 2.08461-2.11312 / 2.02931-2.05634 μm. Altogether, the two K band setups provide near continuous wavelength coverage across the entire K band. Table 5.2 gives the details of these thirteen nights of observations. In Table 5.2, S/N$_L$, S/N$_{K_r}$, S/N$_{K_l}$ are calculated at 3.0, 2.1325, and 2.1515 μm, respectively. Each S/N calculation is for a single channel (i.e., resolution element) for the whole observation.

A top-down schematic of ups And b in orbit around ups And A is shown in Figure 5.1 with the expected orbital phase of each observational epoch marked. Figure 5.2 shows radial velocity measurements of ups And A taken from Fischer et al. (2014) in comparison with expectations for the line-of-sight velocity of ups And b. We aim to take observations when the line-of-sight velocities of the star and planet are most distinct and when we expect to observe a decent amount of dayside radiation from the planet, thus maximizing the planet flux.

Extraction of 1-D Spectra and PCA-like Telluric Correction

Our data reduction and cleaning methods are parallel to those described in Chapter 3 and Piskorz et al. (2016). Here, we summarize deviations from what was previously described.

Figure 5.3 shows a raw spectrum of ups And taken on 2013 October 29, the first three principal components, and a cleaned spectrum of ups And.

Date	Mod. Julian Date (- 2,440,000.5 days)	Mean anomaly M (2π rad)	Barycentric velocity v_{bary} (km/s)	Int. time (min)	S/N$_{L,K}$
***L* band**					
2011 September 6	55810.639	0.25	21.07	60	5376
2011 September 7	55811.637	0.46	20.82	10	2661
2011 September 9	55813.509	0.87	20.33	100	8265
2013 October 27	56592.526	0.59	1.89	140	9173
2013 October 29	56594.512	0.02	0.99	140	5937
2013 November 7	56603.609	0.99	-3.17	180	8686
2014 October 7	56937.553	0.32	10.64	50	5641
***K*$_r$ band**					
2016 September 19	57650.361	0.73	17.14	100	11517
2016 November 12	57704.265	0.38	-5.37	230	12872
2016 December 15	57737.300	0.53	-18.63	70	7666
***K*$_l$ band**					
2014 October 5	56935.579	0.87	11.47	70	7764
2016 August 21	57621.589	0.45	24.15	30	4369
2016 September 19	57650.501	0.73	17.14	120	10649

Table 5.2: NIRSPEC Observations of ups And b

As in our analysis of HD 88133 data, we find the telluric correction by PCA works well for all orders of L band data, but poorly for the K_r and K_l band orders spanning 2.06170-2.08703 μm and 2.02931-2.05634 μm where there is a dense forest of telluric CO_2 lines. We also find that a few nights of K band observations were contaminated by significant issues with the read-out electronics. In these cases, we exclude the data on the "bad" side of the detector from our analysis; about 25% of the data is on the noisy side of the detector. Additionally, we remove the 2011 September 7 observations from our data set, since the ten minute total integration time is not sufficient for principal component analysis.

As in Piskorz et al. (2016), all but about 0.1% of the variance in each night's data set is encapsulated by the first principal component. The following results are roughly consistent for data sets with more than the first principal component removed. As discussed in Section 5.4 and shown in Figure 5.7, the expected photometric contrast α_{phot} at the observed wavelengths is $\sim 10^{-6}$. Based on the percent variance removed by each principal component we determine that deletion of a signal of this magnitude requires the removal of upwards of the first fifteen principal components from our data. In the analysis that follows, our data set has the first five principal components removed, leaving the stellar and planetary signals intact.

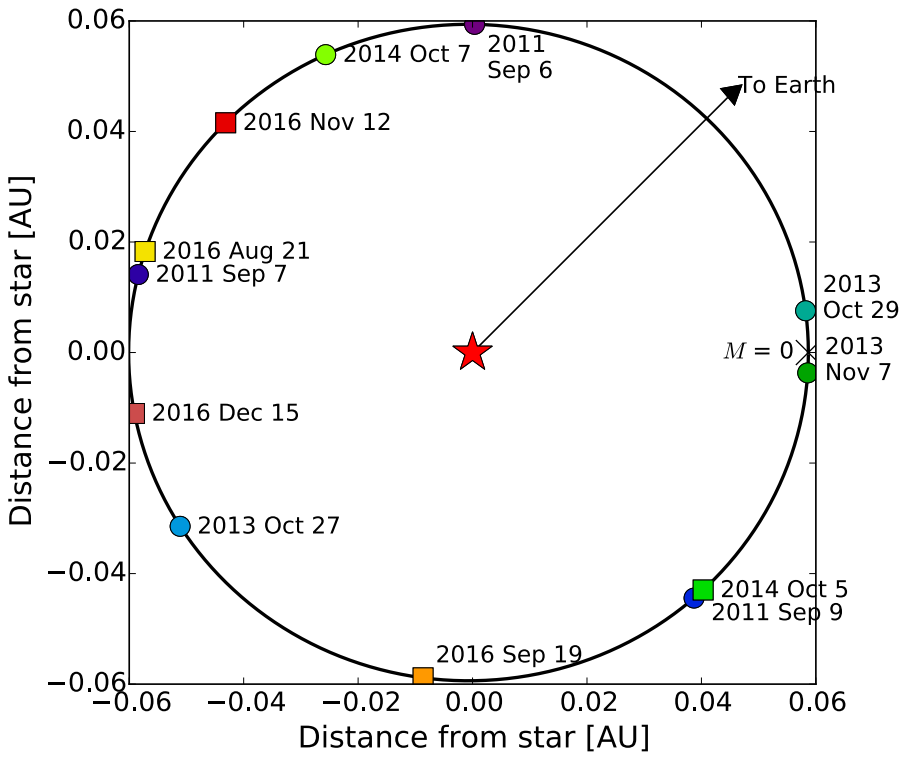

Figure 5.1: Top-down schematic of the orbit of ups And b around its star according to the orbital parameters derived by McArthur et al (2010). Each point represents a single epoch of NIRSPEC observations of the system. Circles indicate L band observations and squares represent K band observations. The black arrow represents the line of sight to Earth.

5.3 Data Analysis and Results

A two-dimensional cross-correlation analysis reveals the ideal velocity shifts for the stellar and planet spectra embedded in our clean data set Zucker & Mazeh (1994). This analysis calls for accurate stellar and planetary model spectra.

Model Stellar Spectrum

Our PHOENIX stellar model is interpolated between the spectral grid points presented in (Husser e al. 2013) for the effective temperature $T_{\rm eff}$, surface gravity log g, and metallicity [Fe/H] values listed for ups And A in Table 5.1. We rotationally broaden this model, assuming a stellar rotation rate of 9.62 km/s (Valenti & Fischer 2005) and limb darkening coefficient of 0.29 (Claret 2000). For completeness, we instrumentally broaden the stellar model with an instrumental profile fitted to the data.

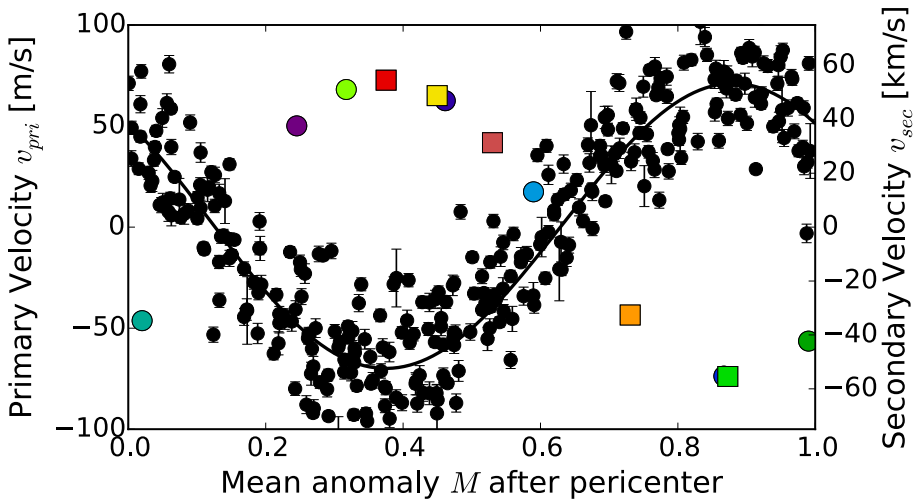

Figure 5.2: RV data from Fischer et al. (2014) with the best-fit stellar RV (primary velocity) curve over-plotted in black, corresponding to the left y-axis. RV contributions from ups And c and d have been removed according to the orbital elements provided in McArthur et al. (2010). The colored points represent the NIRSPEC observations of this planet correspond to the right y-axis and are based on the observation phases and our expectations of their secondary velocities. In the course of this paper, we will show that the most likely value for the Keplerian orbital velocity of ups And b is 55 ± 9 km/s.

Model Planetary Spectrum

We compute a high-resolution (R=250,000) thermal emission spectrum of ups And b according to the SCARLET framework (Benneke 2015). The thermal structure and equilibrium chemistry of the ups And b model spectrum are dependent upon the expected stellar flux at the location of the planet. The model assumes perfect heat redistribution (perhaps a flawed assumption, see Crossfield et al. 2010 and Section 5.4) and a solar elemental composition (Asplund et al. 2009). The temperature profiles are computed self-consistently for a 1 x solar, C/O=0.54 atmosphere by iteratively recalculating the radiative-convective equilibrium and atmospheric equilibrium chemistry. We assume an internal heat flux of T_{int}=75 K. Our default model in this paper is has an inverted temperature structure due to the short-wavelength absorption of TiO and VO. The SCARLET framework includes molecular opacities of H_2O, CH_4, NH_3, HCN, CO, CO_2, and TiO (ExoMol database by Tennyson & Yurchenko 2012), molecular opacities of O_2, O_3, OH, C_2H_2, C_2H_4, C_2H_6, H_2O_2, and HO_2 (HITRAN database by Rothman et al. 2009), absorptions by alkali metals (VALD database by Piskunov et al. 1995), H_2-broadening (Burrows & Volobuyev

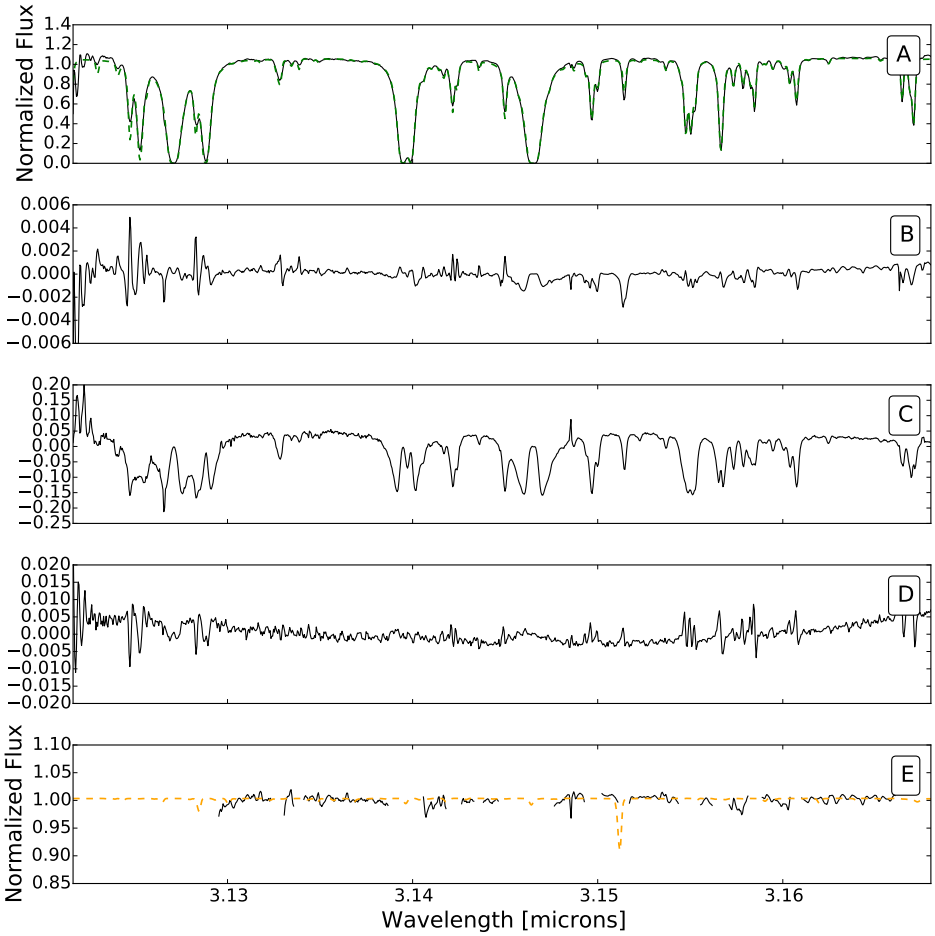

Figure 5.3: Raw spectrum of ups And, first three principal components, and cleaned spectrum. (A): One order of data from ups And taken on 2013 October 29. The best-fit telluric spectrum is over plotted as a dashed green line. (B-D): The first three principal components in arbitrary units describing changes in air mass, molecular abundances in the Earth's atmosphere, and plate scale, respectively. (E): Same as (A), but with the first five principal components removed, and with a fitted stellar spectrum overplotted as a dashed orange line.

2003), and collision-induced broadening from H_2/H_2 and H_2/He collisions (Borysow 2002).

Line positions and amplitudes are critical to obtaining the correct cross-correlation function. We use the line information from ExoMol for H_2O and CH_4. The line lists were computed using ab-initio calculations based on quantum mechanics. The line center wavelengths of these calculations are accurate. Line amplitudes are harder to compute in ab-inbitio calculations, but we are using the best state-of-the-art line lists available, which is ExoMol for the temperature encountered in hot Jupiters. Model planet spectra are convolved with the instrumental profile from Section 6.3 before the cross-correlation analysis.

Two-Dimensional Cross Correlation

We use the TODCOR algorithm (Zucker & Mazeh 1994) to cross-correlate each order of data for each epoch with the stellar and planet models, yielding a two-dimensional array of cross-correlation values for different stellar and planetary velocity shifts.

As in Piskorz et al. (2016), at this step, we eliminate the K_r and K_l band orders ranging from 2.3 - 2.4 μm from the analysis since there is high correlation between the stellar and planetary models themselves at these wavelengths. This means we remove any signal from carbon monoxide, and the dominant molecule in the planetary model in the remaining wavelengths is water vapor.

Following Lockwood et al. (2014), for each epoch of observations, we combine the correlation function for each order and produce nightly stellar and planetary maximum likelihood curves, a few of which are shown in Figure 5.4. For every epoch, we are able to confirm the expected velocity of the star (see Equation 3.37). We suspect that the significant off-peak correlation signature in the primary velocity curve for the K_l band data implies that we were too aggressive in our clipping and that we have scratched the noise limit of our data (see Section 5.4).

The right column of Figure 5.4 shows the maximum likelihood curves for shifts in the planetary velocity. Two aspects are notable. First, the likelihood variations of the K band data are an order of magnitude smaller than those of the L data, indicative of the small signals present in the K band data. Second, there are many peaks and troughs in the planetary maximum likelihood curves. Therefore, determining the line-of-sight velocity of the planet is not straightforward. Only one peak in each maximum likelihood curve represents the real planetary velocity for a given epoch;

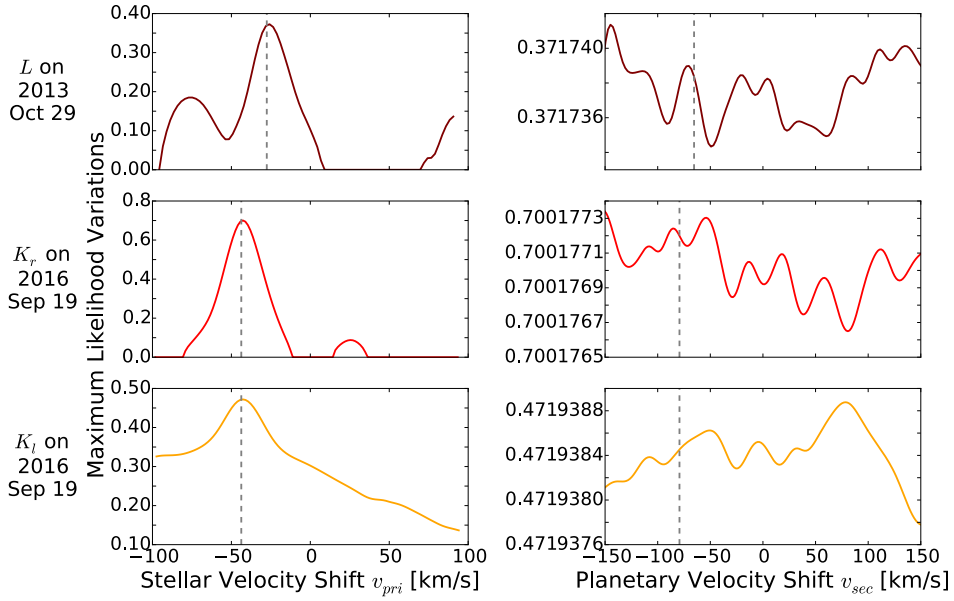

Figure 5.4: Maximum likelihood functions for selected epochs of data in each band. Panels in the left column show the maximum likelihood function for the velocity shift of the star ups And in each band observed while panels in the right column shows the maximum likelihood function for the velocity shift of the planet ups And b. The grey vertical lines represent the expected values of v_{pri} and v_{sec} (based on the barycentric and systemic velocities and the line-of sight Keplerian velocity determined in Section 5.3). Based on $\sigma_{f+\omega}$, the error on v_{sec} is 0.4 km/s.

the other peaks are chance correlations with the repeating structure in the planetary model. The multi-epoch data are critical in breaking this degeneracy.

Planet Mass and Orbital Solution

We use the cross correlation functions for the planetary velocity shift v_{sec} at each epoch to determine the most likely value of the line-of-sight Keplerian velocity K_P. For the sake of completeness, we use the equation for orbital velocity which considers eccentricity, even though the eccentricity of ups And b is very nearly zero. As a result of this near-zero eccentricity, the mean anomalies M of our observations are essentially the same as the true anomalies f. The velocity v_{sec} of the planet a function of its true anomaly f is given in Equation 3.39. We test orbital velocities from -150 to 150 km/s in steps of 1 km/s and thus test a variety of planet masses and orbital inclinations. This results in a plot of maximum log likelihood versus the planet's orbital velocity (first column of Figure 5.5).

Six L band cross-correlation functions similar to that in the upper right panel of

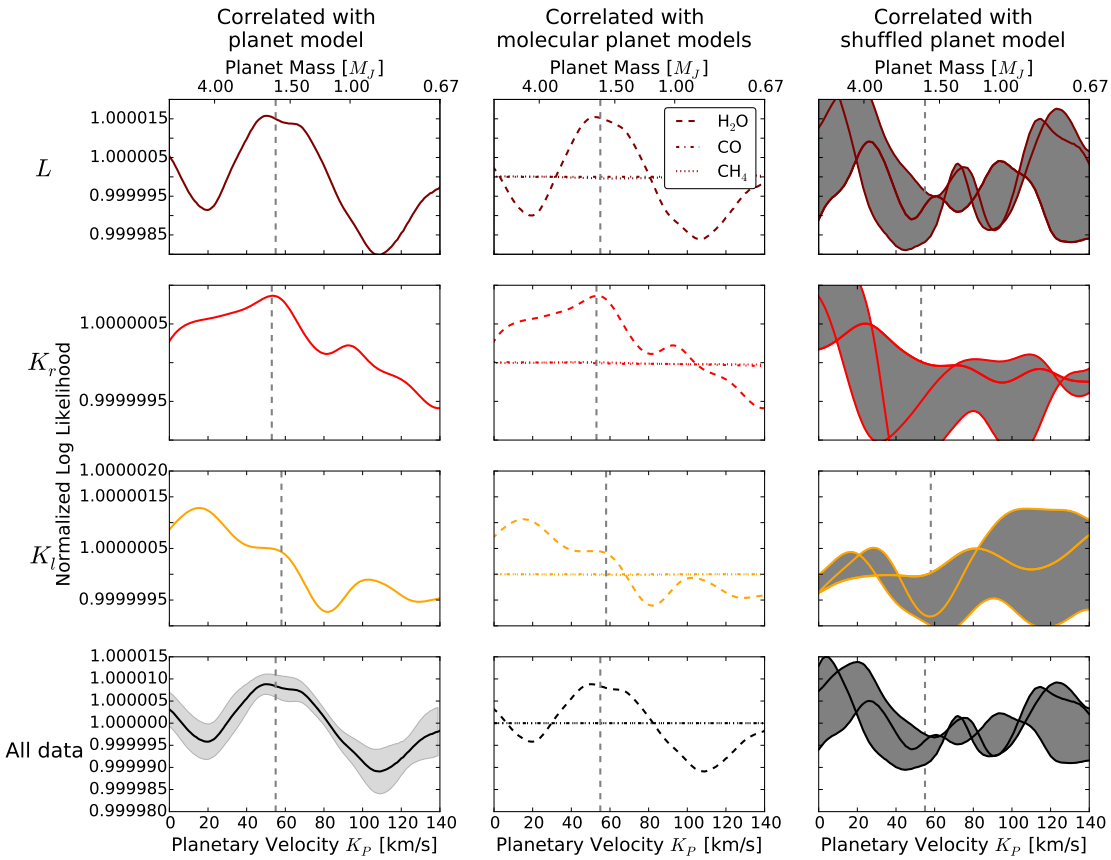

Figure 5.5: Normalized log likelihood as a function of Keplerian orbital velocity K_P. Note that the vertical axes cannot be directly compared. Likelihood curves in the left column are the result of correlating NIRSPEC data with a SCARLET planet model for ups And b. The light shading on the maximum likelihood curve of all the data correlated with a planet model represent the jackknifed error bars. Likelihood curves in the center column are the result of correlation NIRSPEC data with SCARLET planet models containing single molecules. Likelihood curves in the right column are the result of correlation NIRSPEC data with multiple shuffled SCARLET planet models (which eliminates the planet signal in most cases); the dark shading is for the sake of clarity, only. The first row of likelihood curves considers only L band data, the second only K_r band data, the third only K_l band data, and the fourth all the data.

Figure 5.4 are combined to produce the likelihood curve in the upper left panel of Figure 5.5 when combined with equal weighting. The single peak in K_P is at 55 ± 3 km/s. The error bars reported here are the three-sigma error on the mean value of a Gaussian curve fit to the maximum likelihood peak with equal weighting to the points on the maximum likelihood curve. The error bars are not the full-width at half-maximum of the fitted Gaussian. We more robustly calculate the weighting of the points on the maximum likelihood curve and the error bars and significance of the K_P measurement based on the full eleven nights of data later in this section. Three K_r band cross-correlation functions similar to that in the middle right panel of Figure 5.4 produce the likelihood curve in the second row of the first column of Figure 5.5 and shows a peak at K_P = 53 ± 3 km/s. Finally, three K_l band cross-correlation functions similar to that in the bottom right panel of Figure 5.4 produce the likelihood curve in the third row of the first column of Figure 5.5 and shows a peak at K_P = 58 ± 3 km/s.

The combination of all twelve nights of data is shown in the bottom left panel of Figure 5.5 and gives K_P = 55 km/s. We use this value of K_P to calculate the expected v_{sec} for each epoch of observation and note this value as a vertical line on the curves in the right column of Figure 5.4. For most cases (especially in L and K_r bands), the expected v_{sec} corresponds to a local maximum in likelihood. We also use K_P = 55 km/s to calculate the secondary velocities plotted in Figure 5.2.

Given the full suite of data, we calculate the error bars of each point of the maximum likelihood curve using jackknife sampling. We remove one night of data from the sample at a time and recalculate the maximum likelihood curve. The error on each point is proportional to the standard deviation of the twelve resulting maximum likelihood curves. These errors are shown in the bottom left panel of Figure 5.5. These errors are an estimate only. For a Gaussian fit to the peak at 55 km/s, the reduced chi-squared value (chi-squared divided by the number of degrees of freedom) is 0.15, suggesting that the error bars are likely an overestimate. These large error bars are driven by a high variance in the jackknife samples. The Gaussian fit also gives error bars on the ultimate K_P measurement: 55 ± 9 km/s.

To determine the significance of this detection, we use the jackknifed error bars to fit a Gaussian (above) and a straight line and the compare the likelihoods of the fits with the Bayes factor B. Here, the Gaussian fit corresponds to the presence of a planetary signal and the linear fit corresponds to the lack thereof. The Bayes factor B is the ratio of the likelihood of two competing models (Kass & Raftery 1995). If

$2\ln B$ is greater than 10, then the model is very strongly preferred.

For the Gaussian fit compared to the linear fit, the value of $2\ln B$ is 10.5, indicating that the signal at 55 km/s is stronger than a straight line at about 3.7σ. Therefore, the line-of-sight orbital velocity of ups And b is 55 ± 9 km/s. Using the indicative mass of ups And b and the law of conservation of momentum, we calculate that the true mass of ups And b is $1.7\ ^{+0.33}_{-0.24}\ M_J$, and the orbital inclination of ups And b is 24 ± 4°.

Measurements of ups And b's Atmosphere

With SCARLET, we can calculate the contributions of individual molecules (H_2O, CO, and CH_4) to the total spectrum to understand the dominant opacity structures. We cross-correlate these molecular planet models with our L, K_r, and K_l band data. Results of these single molecule cross-correlation calculations are shown in the middle column of Figure 5.5 for each band observed and indicate that the atmospheric opacity of ups And b is dominated by water vapor at the observed wavelengths. The likelihood curves for data correlated with CO- and CH_4-only planetary models show variations at least an order of magnitude smaller than the H_2O-only results. If carbon monoxide or methane are present at these wavelengths, they exists at levels below the detection limit of this data set. (See Section 5.4.) Note that we were forced to remove the CO band at 2.2935 μm from our data set because of the presence of CO features in the stellar spectrum.

5.4 Discussion

Tests of the Orbital Solution

Our initial test of the fidelity of the line-of-sight velocity detection at 55 km/s is to vary the spectroscopic contrast α_{spec}. We test α_{spec} from 10^{-7} to 10^{-3} and find that the peak at 55 km/s is robust down to $10^{-6.5}$. α_{spec} is truly the ratio between the depths of the spectral lines, and so could be as low as zero for perfectly isothermal atmospheres.

Analagous to Piskorz et al. (2016), we produce a "shuffled" planetary model by randomly rearranging chunks of the planetary model. Cross-correlating our data with a shuffled model should show no peak near 55 km/s if the planet truly exists with a line-of-sight orbital velocity of 55 km/s. For each band of data, we run this test three times and the results are shown in the right-hand column of Figure 5.5. The L, K_r, and K_l band detections show minima near 55 km/s, showing that the planet signal is successfully eliminated.

We use our inclination measurement of 24 ± 4° to compare our detection to the results presented in other works. The spectroscopic technique presented here would be unable to detect the motion of ups And b if $i_b < 4.9°$ due to the size of a resolution element on NIRSPEC. Our inclination measurement is largely in agreement with previous works. Spitzer brightness measurements indicated $i_b > 28°$ (Crossfield et al. 2010). Newtonian orbital simulations considering the orbital elements of ups And c and d suggested that orbits having $i_b < 60°$ can be stable (McArthur et al. 2010). Analagous post-Newtonian orbital simulations prescribed a "region of stability" for $i_b < 40°$. Our measurement of $i_b = 24 \pm 4°$ lies within the error bars of these ranges.

System Stability

Many previous works have characterized the ups And A system as on the edge of instability. Here we evaluate our calculation of the inclination of ups And b by running numerical simulations of the system with the Mercury software (Chambers 1999). Mercury is a hybrid-simplectic–Burlisch Stoer algorithm (Chambers 1999). We include the central star ups And A and the three planets ups And b, c, and d, set the time step to one-twentieth of the orbital period of ups And b, and consider general relativity.

Our method of calculating K_P and i_b provides no insight into the longitude of ascending node of ups And b, Ω_b. As a result, we investigate values of i_b between 22° and 27° in steps of 1° and values of Ω_b between 0° and 360° in steps of 10°. We adjust M_b as is necessary given the value of i_b. All other orbital elements are taken from McArthur et al. (2010). Specifically, the orbital elements used for our simulations are listed in Table 6.1.

Of our 216 simulations, 122 were stable for more than 100,000 years. These simulations have $\Omega_b < 100°$ or $\Omega_b > 260°$. Of these systems, 53 were stable for more then 1 Myr, having $\Omega_b < 40$ ° and $\Omega_b > 320°$.

We extract the 24 simulations having $23° < i < 25°$ and run them for 100 Myr. All but two are stable. It seems that for the successful simulations the orbital planes of planets b and d remain roughly aligned. For example, if $i_b = 24°$ and $\Omega_b = 0°$, then the mutual inclination of ups And b and c is about 29° and the mutual inclination of ups And b and d is about 2°. Recall, the mutual inclination of ups And c and d is 29°. Successful simulations tend to have mutual inclinations clustered about these values. In these simulations, the apsides of ups And c and d oscillate as in

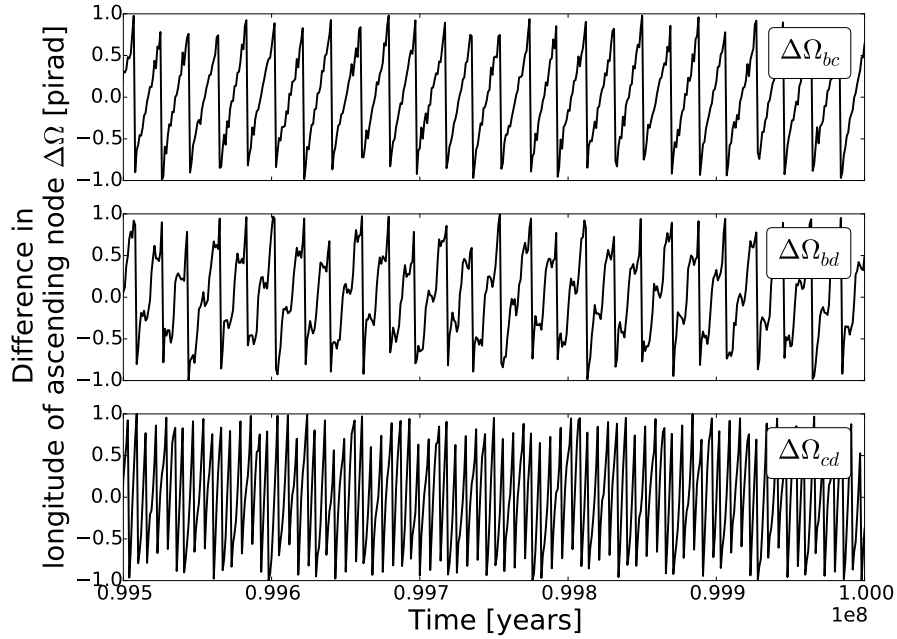

Figure 5.6: Plot of the difference in longitude of ascending node $\Delta\Omega$ versus time for the last 500,000 years of the 100 Myr Mercury simulation for each pair of planets in the ups And system. This simulation was initialized with $i_b = 24°$ and $\Omega_b = 0°$.

Chiang & Murray (2002), Barnes et al. (2011), and other works, and the orbital evolution of ups And b is secular (Figure 5.6). We stress that these simulations are stable not necessarily because of the value of ups And b's inclination, but because of the direction ups And b's inclination vector points over time. Our Mercury simulations provide evidence that stable ups And A systems do indeed exist for the inclination we have measured, and provide insight into the three-dimensional geometry of ups And b's orbit.

The Atmosphere of ups And b

In our planetary model, the L band opacity is dominated by water vapor. Therefore, our L band detection of ups And b's thermal emission spectrum suggests that radiative transfer in the planet's atmosphere is dominated by water vapor at these wavelengths. In fact, the source of the correlation signal for all wavelengths investigated is water vapor (see the middle column of Figure 5.5). Based on the analysis of α_{spec} presented in Section 5.4, the detection of H_2O suggests that its spectroscopic contrast $\alpha_{spec} > 10^{-6.5}$.

We perform a comparison of the cross-correlation results given inverted and non-inverted model spectra. The main differences in the final maximum likelihood curves stem from the different line strengths at a given wavelength for each model. In other words, the differences stem from the optical depths as a function of wavelength. Therefore, the only conclusion we can draw at this time is the atmosphere of ups And b is dominated by water at the probed wavelengths.

Though the K band is typically dominated by CO absorption, the usable K band wavelengths in our dataset do not include strong CO absorption. The non-detections of CO and CH_4 suggest that their spectroscopic contrasts are $\alpha_{spec} < 10^{-6.5}$ at these wavelengths.

Our models do not account for cloud cover, atmospheric recirculation, or the differences between dayside and nightside spectra. Crossfield et al. (2010) reported a flux maximum in the Spitzer phase curve of ups And b at 80° before opposition, or at mean anomaly $M = 0.4$, in our formulation. $M = 0.4$ is almost directly between the phases of 2016 November 12 and 2016 August 21 observations as diagrammed in Figure 6.4. Fortuitously, this indicates that even if the planet's flux maximum is shifted from what would traditionally be expected, our measurements are still able to capture dayside emission.

Observation Notes

From our raw data sets, we calculate the shot noise per resolution element for each observation. (See Table 5.2.) We compare the aggregate shot noise values to the expected photometric signal from the planet for each order observed, using the stellar and planet models described in Sections 5.3 and 5.3. As Figure 5.7 suggests, we easily achieve the required S/N to detect the planet with six nights of L band observations, but only marginally achieve that required with three nights of K_l and K_r observations. In fact, we achieve slightly better shot noise for K_r than for K_l, a possible reason for the stronger detection of the planet signal here (Figures 5.4 and 5.5).

In this suite of observations, the K_l band data sets are equivalent to the K band data presented for HD 88133 in Piskorz et al. (2016). With four nights of K band data, Piskorz et al. (2016) were able to detect the signal from HD 88133 b, though not as clearly as in the six nights of L band data. This points to the general trend that, with NIRSPEC at Keck, L band observations may be more amenable to direct detection of exoplanet atmospheres than those in the K band. For hot Jupiters, the increase

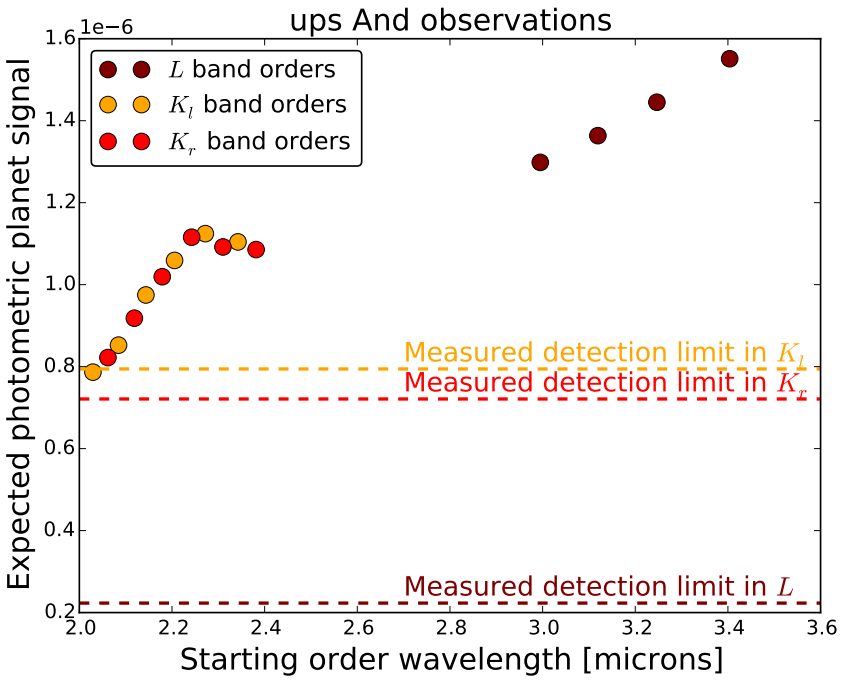

Figure 5.7: Expected planet-star contrast as a function of starting order wavelength compared to achieved photometric contrast. Points represent the expected planet photometric signal calculated from a PHOENIX stellar model and a SCARLET planet model for each observed order of data (6 orders in K_l, 6 orders in K_r, and 4 orders in L). Dotted lines represent the achievable contrast given by the aggregate shot noise for all epochs of data in each band. Note that in our analysis we do not use the first two and final orders of the K_l and K_r bands.

in the thermal background from K to L band is more than compensated for by the significant increase in planet flux relative to the star. In other words, though the increment of detection limit achieved per unit integration time is higher in the K band than in the L band, the star-planet contrast near 2 μm may be too small for a bona fide planet detection with our data. For this cross-correlation method, the superiority of L band observations over K band observations is a demonstration of the theoretical results presented in deKok et al. (2014).

5.5 Conclusion

We detect the thermal emission spectrum of ups And b with ground-based high-resolution spectroscopy. For the hot Jupiter ups And b, we find a Keplerian velocity of 55 ± 9 km/s, a true mass of 1.7 $^{+0.33}_{-0.24}$ M_J, and an orbital inclination of 24 ± 3. With dynamical simulations, we show that the ups And A system is stable for

at least 100 Myr given the reported ups And b orbital elements. Using the many planet lines available in the L and K bands, we determine that the planet's opacity structure is dominated by water vapor. For the set of observations presented here, the signal is noticeably stronger in the L band than in K, suggesting that L band observations may be best suited for these analyses moving forward. Further thermal IR measurements can be used to dig deeper into the structure and compositions of hot Jupiter atmospheres and eventually atmospheres of planets at larger semi-major axes.

5.6 References

Adams, F.C., & Laughlin, G. 2006, ApJ, 649, 2.

Asplund, M., Grevesse, N., Suval, J.A., Scott, P. 2009, ARAA, 47, 1

Barnes, R. & Greenberg, R. 2006b, ApJ, 652, L53

Barnes, R. & Greenberg, R. 2007, ApJL, 659, L53

Barnes, R., Greenberg, R., Quinn, T.R., et al. 2011, ApJ, 726, 2

Benneke, B. 2015, arXiv:1504.07655

Birkby, J. L., de Kok, R. J., & Brogi, M. et al. 2013, MNRAS, 436, L35

Boogert, A. C. A., Blake, G. A., & Tielens, A. G. G. M. 2002, ApJ, 577, 271

Borysow, A. 2002, A&A, 390, 4

Brogi, M., Snellen, I.A.G., de Kok, R.J., et al. 2012, Nature, 486, 502

Brogi, M., Snellen, I.A.G., de Kok, R.J., et al. 2013, ApJ, 767, 1

Brogi M., de Kok R. J., Birkby J. L., Schwarz H. & Snellen I. A. G. 2014, A&A, 565A, 124B

Brogi, M., de Kok, R.J., Albrecht, S. et al. 2016, ApJ, 817, 2

Burrows, A., & Volobuyev, M. 2003, ApJ, 583, 985

Butler, R.P., Marcy, G.W., Williams, E. et al. 1997, ApJ, 474, 2

Butler, R.P., Marcy, G.W., Fisher, D.A., et al. 1999, ApJ, 526, 916

Chambers, J.E. 1999, MNRAS, 304, 793-799.

Chiang, E.I., & Murray, N. 2002, ApJ, 576, 1

Claret, A . 2010, A&A, 529, A79

Crossfield, I.J.M., Hansen, B.M.S., Harrington, J. et al. 2010, ApJ, 723, 2

Curiel, S. et al. 2011, A&A, 525, A78

Dietrick, R., Barnes, R., McArthur B., et al. 2015, ApJ, 798, 1

de Mooij, E.J.W., Brogi, M., de Kok, R.J., et al. 2012, A&A 538, A46

de Kok R. J., Brogi M., Snellen I. A. G. et al. 2013, A&A, 554, A82

de Kok R. J., Birkby, J., Brogi M. et al. 2014, A&A, 561, A150

Fischer, D.A., Marcy, G.W., & Spronck, J.F.P. 2014, ApJSS, 210, 1

Gonzalez, G. & Laws, C. 2007, MNRAS, 278, 1141

Harrington, J., Hansen, B. M., Luszcz, S. H., et al. 2006, Science, 314, 623

Husser, T.-O., Wende-von Berg, S., Dreizler, S., et al. 2013, A&A, 553, A6

Kass, R.E., & Raftery, A.E. 1995, JASA, 90,773

Lissaeur, J.J. & Rivera, E.J. 2001, ApJ, 554, 1141

Lockwood, A.C., Johnson, J.A., Bender, C.F., et al. 2014, ApJ, 783, L29

Lowrance, P.J., Kirkpatrick, J.D., & Beichman, C.A. 2002, ApJL, 572, 1

Martins, J.H.C., Santos, N.C., Figueira, P., et al. 2015, A&A, 576, A134

McArthur, B.E., Benedict, G.F., Barnes, R., et al. 2010, ApJ, 715:1203-1220

McLean, I. S., Becklin, E. E., Bendiksen, O., et al. 1998, Proc. SPIE 3354, 566

Nagasawa, M., Ida, S., & Bessho, T. 2008, ApJ, 678, 498

Nidever, D.L., Marcy, G.S., Butler, R.P., et al. 2002, ApJSS, 141, 503

Piskorz, D., Benneke, B., Crockett, N.R. et al. 2016, ApJ, 832, 2

Piskunov, N. E., Kupka, F., Ryabchikova, T. A., Weiss, W. W., & Jeffery, C. S. 1995, A&A S, 112, 525

Rivera, E.J., & Lissaeur, J.J. 2000, ApJ, 530, 454

Rodler, F., Lopez-Morales, M., & Ribas, I. 2012. ApJL, 753, L25

Rothman, L.S., Gordon, I.E., Barbe, A., et al. 2009, J. Quant. Spectrosc. Radiat. Transfer, 110, 533

Schwarz, H., Brogi, M., deKok, R.J., et al. 2015, A&A, 579, A111

Snellen, I. A.G., de Kok, R. J., de Mooij, E. J. W., & Albrecht, S. 2010, Nature, 465, 1049

Snellen, I.A.G., Brandl, B.R., deKok, R.J., et al. 2014, Nature, 503, 63

Takeda, G., Ford, E.B., Sills, A. et al. 2007, ApJSS, 168, 2

Tennyson, J., & Yurchenko, S. N. 2012, MRNAS, 425, 21

Valenti, J. A., Butler, R. P., & Marcy, G. W. 1995, PASP, 107, 966

Valenti, J.A., & Fischer, D.A., 2005, ApJSS, 189, 141

vanBelle, G.T., & vonBraun, K. 2009, AJ, 661, 1085

Wright, J.T., Upadhyay, S., Marcy, G.W., et al. 2009, ApJ, 693, 2

Zucker, S. & Mazeh, T. 1994, ApJ, 420, 806

Chapter 6

DIRECT DETECTION OF KELT-2AB'S ATMOSPHERE

This chapter is adapted from work submitted as

Piskorz, D., M. Line, H. Knutson, et al. (2017). *Submitted to The Astronomical Journal*.

6.1 Introduction

The direct detection method's reliance on the Doppler shifting of the planet's spectrum provides a pathway towards not only characterizing the atmospheres of non-transiting planets, but also constraining atmospheric models of transiting planets having additional broadband data. The combination of space-based, low-resolution spectra with ground-based, high-resolution spectra was carried out on the hot Jupiter HD 209458 b (Brogi et al. 2017). The data set suggested an oxygen-rich atmosphere (C/O < 1 at 3.5σ) and sub-stellar metallicity (0.1-1.0 times stellar at 1σ), and provided tighter constraints on the molecular abundances of water vapor, carbon monoxide, and methane than either dataset alone could have.

Here, we apply the observation, reduction, and cross-correlation techniques presented in Chapter 3 to the transiting hot Jupiter KELT-2Ab and present a method for combining ground-based (Keck NIRSPEC) and space-based (Spitzer IRAC) observations to provide constraints on KELT-2Ab's atmospheric composition. KELT-2 (also commonly known as HD 42176) was targeted by the KELT (Kilodegree Extremely Little Telescope) North transit survey. Once the initial transit detection was made with five years' worth of data, follow-up radial velocity measurements were made with TRES (Tillinghast Reflector Echelle Spectrograph) and follow-up photometry was taken with four telescopes (Beatty et al. 2012). KELT-2 is a binary star system with a hot Jupiter orbiting KELT-2A. KELT-2A is a late F star having $T_{\rm eff}$ = 6148 K and R_{st} = 1.836 $R_{\odot}$. KELT-2B is a K2 star and was shown to be bound by the photometry presented in Beatty et al. (2012). The two stars have a projected separation of 2.29" or 295 ± 10 AU. The binary system was more recently observed by Wollert et al. (2015), and remains bound. KELT-2Ab orbits KELT-2A. It is a hot Jupiter with a mass of 1.52 M_J, a mildly-inflated radius of 1.29 R_J, and orbital period of 4.11 days. The relevant properties of KELT-2A and KELT-2Ab are given

Property	Value	Reference
KELT-2A		
Mass, $M_\star$	$1.314\ ^{+0.063}_{-0.060} M_\odot$	Beatty et al. (2012)
Radius, $R_\star$	$1.836\ ^{+0.066}_{-0.046} R_\odot$	Beatty et al. (2012)
Effective temperature, $T_{\rm eff}$	6148 ± 48 K	Beatty et al. (2012)
Metallicity, [Fe/H]	0.034 ± 0.78	Beatty et al. (2012)
Surface gravity, $\log g$	$4.030\ ^{+0.015}_{-0.026}$	Beatty et al. (2012)
Rotational velocity, $v \sin i$	9.0 ± 2.0	Beatty et al. (2012)
Systemic velocity, v_{sys}	-47.4 km/s	Gontcharov (2006)
K band magnitude, K_{mag}	7.35 ± 0.03	Cutri et al. 2003
KELT-2Ab		
Velocity semi-amplitude, K	$161.1\ ^{+7.6}_{-8.0}$ m/s	Beatty et al. (2012)
Line-of-sight orbital velocity, K_P (transit measurement)	$145\ ^{+9}_{-8}$ km/s	Beatty et al. (2012)
Line-of-sight orbital velocity, K_P (NIRSPEC measurement)	148 ± 7 km/s	This work
Mass, M_p	1.524 ±0.088 M_J	Beatty et al. (2012)
Radius, R_p	$1.290^{+0.064}_{-0.050}\ R_J$	Beatty et al. (2012)
Semi-major axis, a	0.05504 ± 0.00086 AU	Beatty et al. (2012)
Period, P	4.1137913 ± 0.00001 days	Beatty et al. (2012)
Eccentricity, e	0	Beatty et al. (2012)
Argument of periastron, ω	90°	Beatty et al. (2012)
Time of periastron, t_{peri}	$2455974.60338^{+0.00080}_{-0.00083}$ JD	Beatty et al. (2012)

Table 6.1: KELT-2A System Properties

in Table 6.1.

In Section 6.2, we detail Spitzer observations of KELT-2Ab and reduction. Section 6.3 details the NIRSPEC observations of KELT-2Ab and reduction. Section 6.4 describes the self-consistent grid of planetary atmospheric models used in Section 6.5's cross-correlation analysis of the NIRSPEC data. We calculate a NIRSPEC-informed prior in Section 6.5 and use it to fit atmospheric models to Spitzer observations in Section 6.6. We discuss our measurements of the planet's atmosphere in Section 6.7 and conclude in Section 6.8.

6.2 Spitzer Observations and Data Reduction

Spitzer Observations

We observed KELT-2A's secondary eclipse in the 3.6 and 4.5 μm bands for one session each with the Infrared Array Camera (IRAC; Fazio et al. 2004) on the Spitzer Space Telescope (Werner et al. 2004) as a part of Program ID 10102 (Deming et al.). Spitzer observations and results are given in Table 6.2. In Table 6.2, t_{trim} is the amount of time trimmed from the start of each time series, n_{bin} is the bin size used

λ (μm)	Start Date (UT)	t_{trim} (hr)	n_{bin}	r_{phot}	Bkgd. (%)	Eclipse Depth (ppm)	Eclipse Time (BJD_UTC)
3.6	2014 Dec 17	0.5	192	2.5	0.61	572^{+45}_{-46}	2457009.218±0.001
4.5	2014 Dec 25	0.5	198	3.0	0.38	616^{+44}_{-45}	2457017.448±0.001

Table 6.2: Spitzer Observations and Measurements of KELT-2Ab

in the photometric fits, r_{phot} is the radius of the photometric aperture in pixels, and "Bkgd" is the Relative sky background contribution to the total flux in the selected aperture.

We used the standard peak-up pointing mode for these observations, which places the star reliably in the center of a pixel after allowing for an initial 30 minute settling time at the new pointing position. We observed our target in subarray mode with 0.4 s exposures in both bandpasses with a total duration of 14.4 hours (120,832 images) for each visit. The raw photometry for each band pass is shown in Figure 6.1 and the data with detector trends removed and best-fit light curves is shown in Figure 6.2.

Spitzer Data Reduction

We utilize the flat-fielded and dark-subtracted "Basic Calibrated Data" (BCD) images provided by the standard Spitzer pipeline for our analysis. We first estimate the sky background by masking out a circle with a radius of 15 pixels centered on the position of the star, as well as the central several (13th-16th) columns and the central two (14th-15th) rows, which are contaminated by diffraction spikes from the star. We also exclude the top (32nd) row of the array, which displays a systematically lower value than the rest of the image. We then discard 3σ outliers and make a histogram of the remaining pixel values, which are drawn from the corners of the 32x32 pixel array. We fit this histogram with a Gaussian function to determine the sky background and subtract this background from each image.

We determine the position of the star in each image using flux-weighted centroiding with a radius of 3.5 pixels, and calculate the flux in a circular aperture with radii of 2.0 - 3.0 pixels (in steps of 0.1 pixels) and 3.5 - 5.0 pixels (in steps of 0.5 pixels) to create our photometric time series. We consider an alternative version of the photometry utilizing a time-varying aperture, where we scale the radius of the aperture proportionally to the square root of the noise pixel parameter, which is proportional to the full width half max (FWHM) of the stellar point spread function (Knutson et al. 2012; Lewis et al. 2013), but find that we obtain optimal results in both bandpasses using a fixed aperture. In all cases, we calculate the noise pixel

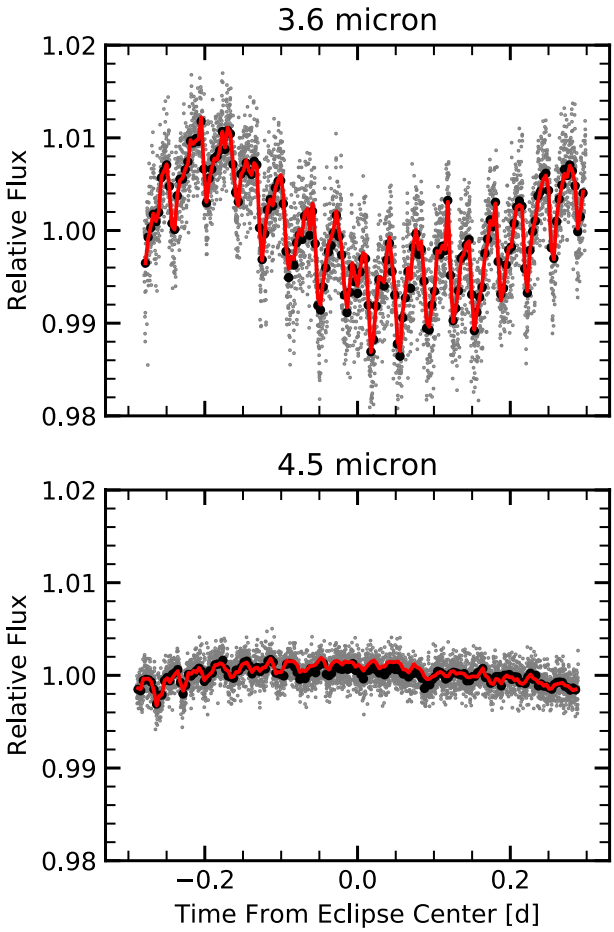

Figure 6.1: Raw Spitzer photometry for 3.6 and 4.5 μm secondary eclipses plotted in 10-second (grey) and 5-minute (black) bins. The best-fit detector model for each observation is shown as a red line.

parameter using an aperture with a radius of 4.0 pixels.

After extracting a photometric time series for each visit, we fit each time series with the pixel-level decorrelation (PLD) model described in Deming et al. (2015), in which we utilize a postage stamp of nine pixels centered on the position of the star. We also include both a linear and (for the 3.6 μm data only) an exponential function of time. We also assume that all points in our time series have the same measurement error, and allow this error to vary as a free parameter in our fits. As discussed in Kammer et al. (2015) and Morley et al. (2016), we optimize our choice of aperture, bin size, and trim duration individually for each visit by selecting the options which simultaneously minimize the RMS of the unbinned residuals as well as the time-correlated noise in the data. We quantify this time-correlated noise

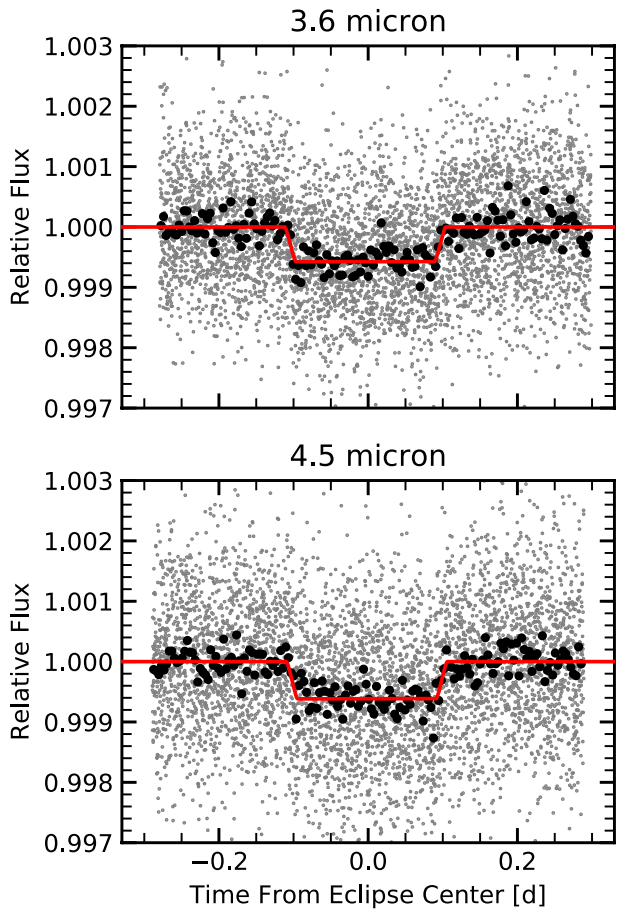

Figure 6.2: Normalized secondary eclipse light curves after dividing out the best-fit detector noise model are shown in grey (10-second bins) and black (5-minute bins). The best-fit eclipse light curves are overplotted in red.

component by calculating the RMS as a function of bin size in steps of $2n$ points per bin (Figure 6.3), and then take the least squares difference between the log of the predicted square root of n scaling and the log of the actual RMS as a function of bin size.

In order to improve the convergence of our Markov-Chain Monte Carlo (MCMC) fits we elect to reduce the degrees of freedom in our model by using linear regression to determine the optimal set of nine PLD coefficients at each step in the MCMC chain. Although this might cause us to under-estimate the uncertainties in our best-fit eclipse depth and time, we find that in practice the uncertainties in these parameters change by a negligible amount when we allow the PLD coefficients to vary as free parameters in our fits as compared to the linear regression approach. It also has the added benefit of substantially reducing the convergence time for our

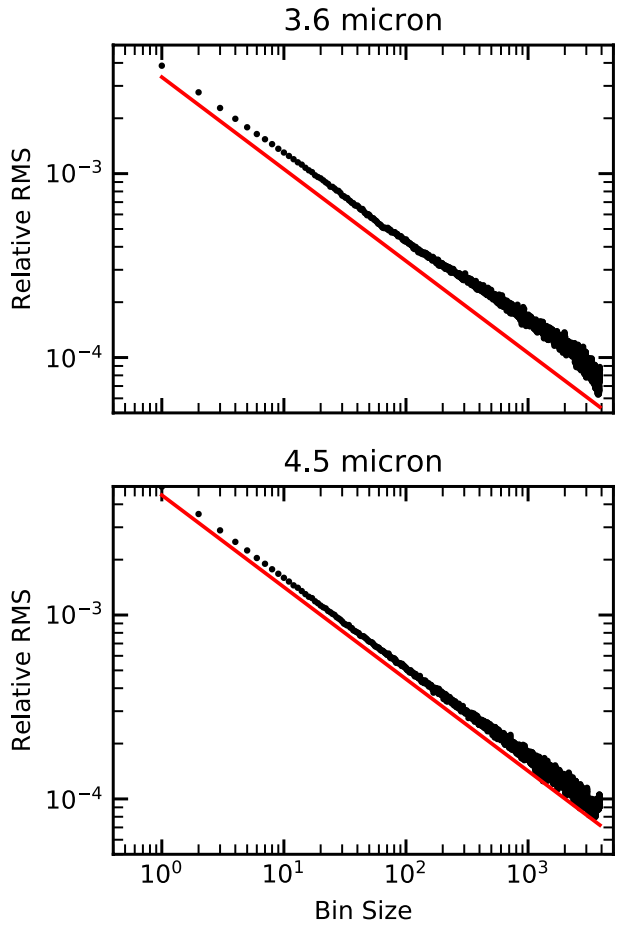

Figure 6.3: Standard deviation of residuals for 3.6 and 4.5 μm Spitzer light curves as a function of bin size are shown in black with the predicted photon noise limit for each channel scaled by the square root of the number of points in each bin shown in red for comparison.

MCMC chains, as the nine PLD coefficient values are strongly correlated with one another and it takes substantial time to fully explore this nine-dimensional space.

To fit the secondary eclipse light curves, we use the `batman` package (Kreidberg 2015). Figure 6.2 shows the corrected Spitzer photometry and the best-fit secondary eclipse light curves for each channel. The 3.6 micron (channel 1) secondary eclipse depth is 572^{+45}_{-46} ppm and the 4.5 micron (channel 2) secondary eclipse depth is 616^{+44}_{-45} ppm. The eclipse times are consistent with a circular orbit, and the eclipse depths are inconsistent with a blackbody.

These secondary eclipse measurements inform the contrast values used in the reduction and cross-correlation analysis of NIRSPEC L band data discussed in Sec-

Date	Julian Date (- 2,400,000 days)	Mean anomaly M (2π rad)	Barycentric velocity v_{bary} (km/s)	Int. time (min)	S/N$_L$
2015 December 1	57357.892	0.26	11.77	180	1476
2015 December 31	57387.967	0.57	-3.62	100	1125
2016 February 18	57436.810	0.44	-24.74	80	1070
2016 December 15	57738.104	0.68	4.79	20	650
2017 February 10	57794.796	0.46	-22.42	130	2103
2017 February 18	57802.867	0.42	-24.93	140	1414

Table 6.3: NIRSPEC Observations of KELT-2Ab

tions 6.3 and 6.5. In Section 6.6, we will use these eclipse depths alone and in tandem with NIRSPEC L band observations of KELT-2Ab to place constraints on the properties of the hot Jupiter's atmosphere.

6.3 NIRSPEC Observations and Data Reduction

NIRSPEC Observations

We observe the KELT-2A system with NIRSPEC (Near InfraRed SPECtrometer; McLean et al. 1998) at Keck Observatory on six nights (2015 December 1, 2015 December 31, 2016 February 18, 2016 December 15, 2017 February 10, and 2017 February 18) in L band. We use the 0.4"x24" (3-pixel) slit setup, an ABBA nodding pattern for data acquisition (2-minute exposure per nod), and obtain resolutions $\left(\frac{\lambda}{\Delta\lambda}\right)$ of $\sim$ 25,000. We adjust the echelle and cross-disperser grating angles to provide wavelength coverage in each order of 3.4038-3.4565 / 3.2467-3.3069 / 3.1193-3.1698 / 2.995-3.044 μm. Table 6.3 gives more details on these observations. In Table 6.3, Julian date and mean anomaly refer to the middle of the observing sequence and S/N$_L$ is calculated at 3.0 μm. Each S/N calculation is for a single channel (i.e., resolution element) for the whole observation.

Figures 6.4 and 6.5 provide the location and radial velocity of KELT-2Ab for each observation epoch. We observe the system when the planet has a high line-of-sight velocity and thermal emission from its hot dayside is visible. Our observations are short enough that the planet's signal does not smear across pixels for the entire co-added observation.

NIRSPEC Data Reduction

We reduce our data and correct for telluric lines with the methods and Python pipeline described in Piskorz et al. (2016) and Chapter 3 with few deviations. A

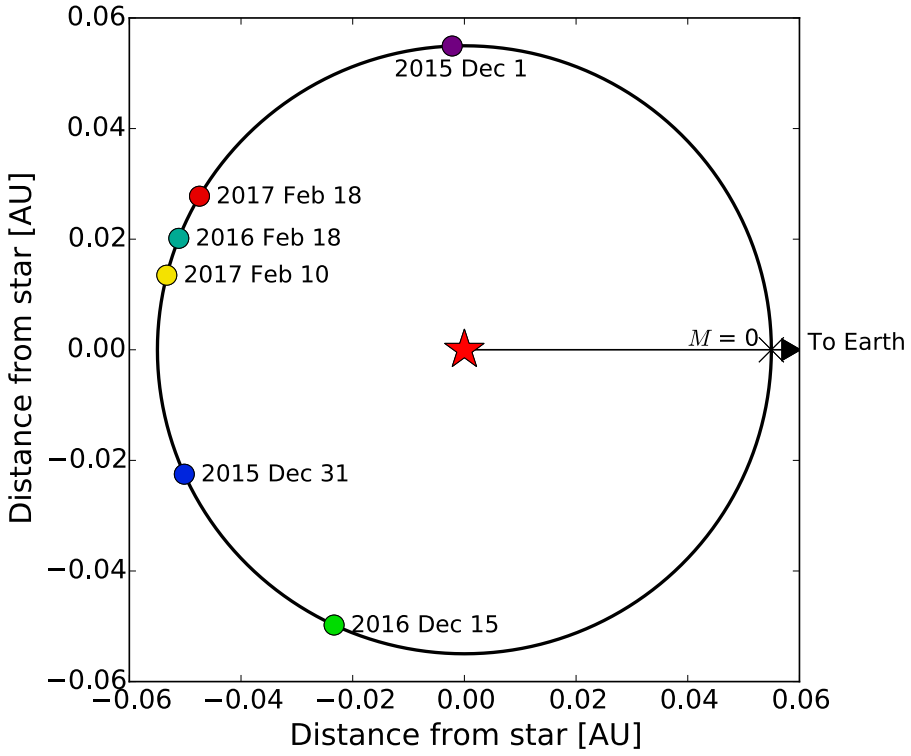

Figure 6.4: Top-down schematic of the orbit of KELT-2Ab around its star according to the orbital parameters shown in Table 6.1. Each point represents a single epoch of NIRSPEC observations of the system. The black arrow represents the line of sight to Earth.

typical result of model-guided principal component analysis on KELT-2Ab is shown in Figure 6.6.

The following results are roughly consistent for data sets with more than the first principal component removed. As suggested by the Spitzer data in Section 6.2, the expected photometric contrast α_{phot} is roughly 600 ppm in the IRAC bandpasses. We calculate the percent variance removed by each principal component, and find that up to five principal components can be removed without deleting the planet signal. In the following sections, we use a KELT dataset with the first five principal components removed.

This L band data set will be interpreted with a two-dimensional cross-correlation technique (Zucker & Mazeh 1994 and Section 6.5). Such an analysis first requires a set of high-resolution planetary model spectra, which we describe in the next section.

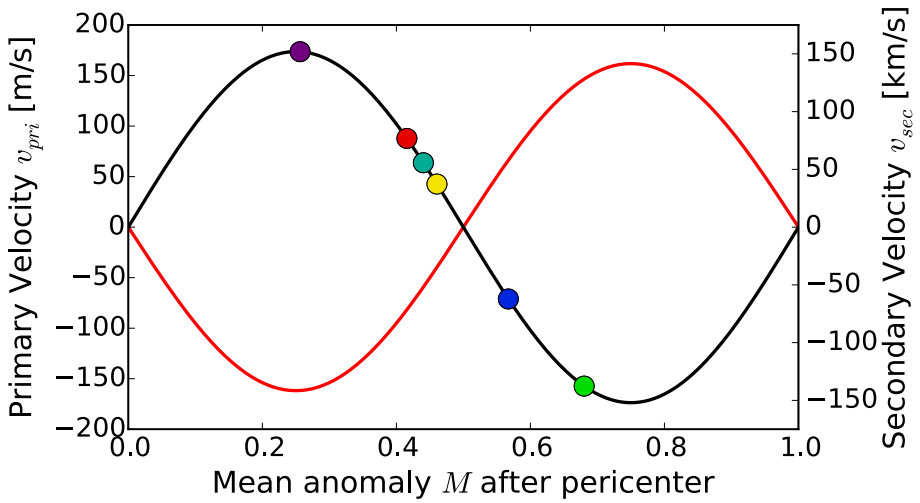

Figure 6.5: Toy model showing the spectroscopic binary nature of the KELT-2A system. Based on values in Table 6.1, the stellar RV curve is in red and planetary RV curve is in black. The colored points represent the NIRSPEC observations of this planet, correspond to the right y-axis, and are based on the observation phases and our expectations of the secondary velocities at those phases.

6.4 High-Resolution Atmospheric Models with ScCHIMERA

We use a newly developed grid of cloud free self-consistent thermochemical-radiative-convective equilibrium models (Self-consistent CHIMERA — ScCHIMERA) to simultaneously interpret the Spitzer and NIRSPEC *L* band data. The CHIMERA framework was originally presented in Line et al. (2013a).

ScCHIMERA solves for radiative equilibrium using the Toon et al. (1989) two-stream source function technique for the planetary emission combined with a Newton-Raphson iteration scheme (McKay et al. 1989). Opacities are treated within the "resort-rebin" correlated-K (CK; Lacis & Olnis 1991) framework described in Molliere et al. (2015) and Amundsen et al. (2017), and can handle any arbitrary combination of molecular abundances. The CK tables for H_2O, CH_4, CO, CO_2, NH_3, H_2S, HCN, C_2H_2, Na, K, TiO, VO, FeH, and H_2-H_2/He collision induced opacities are generated at an R=100 from 0.3 -200 μm for 20 Gauss-Quadrature g-ordinates from the line-by-line cross-section tables described in Freedman et al. (2008; 2014, Table 1). Extinction due to H_2 and He Rayleigh scattering is added in as a continuum absorber within the CK framework. Convective adjustment while maintaining energy conservation is imposed where the radiative temperature gradient is steeper than the local adiabat.

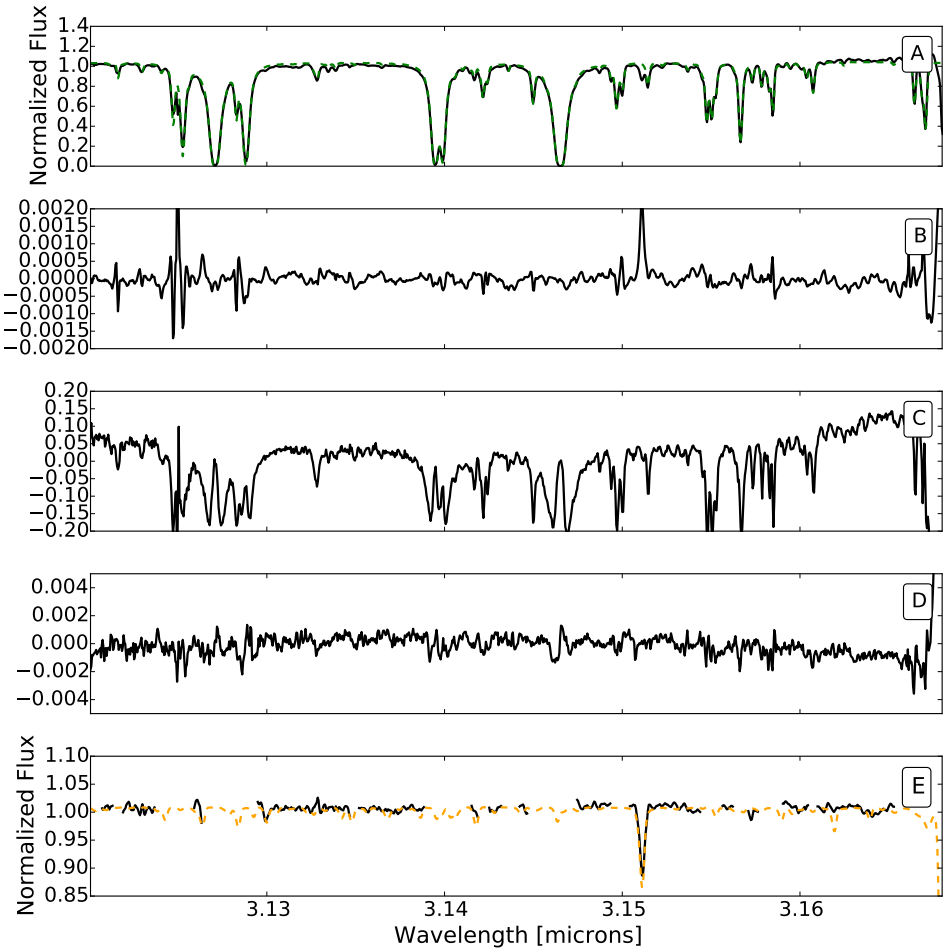

Figure 6.6: Raw spectrum of KELT-2A, the first three principal components of the time-series of data, and a cleaned spectrum. (A): One order of data from KELT-2A taken on 2015 December 1. The best-fit telluric spectrum is over plotted as a dashed green line. (B-D): The first three principal components in arbitrary units. These components describe changes in air mass, molecular abundances in the Earth's atmosphere, and plate scale, respectively, over the course of the observation. (E): Same as (A), but without the first five principal components. A fitted stellar spectrum is overplotted as a dashed orange line.

In this cloud-free version we need not consider scattering in the visible stream. Here, we treat the wavelength-dependent incident stellar flux (from a PHOENIX stellar grid model; Husser et al. 2013) by including only the "direct" beam and pure extinction over an average cosine zenith angle of $\frac{1}{\sqrt{3}}$. The incident stellar flux is scaled by a parameter, f, to account for day-night heat transport and an unknown albedo. Chemical equilibrium abundances, molecular weight, and atmospheric heat capacities are computed using the CEA2 routine (Gordon & McBride 2003)

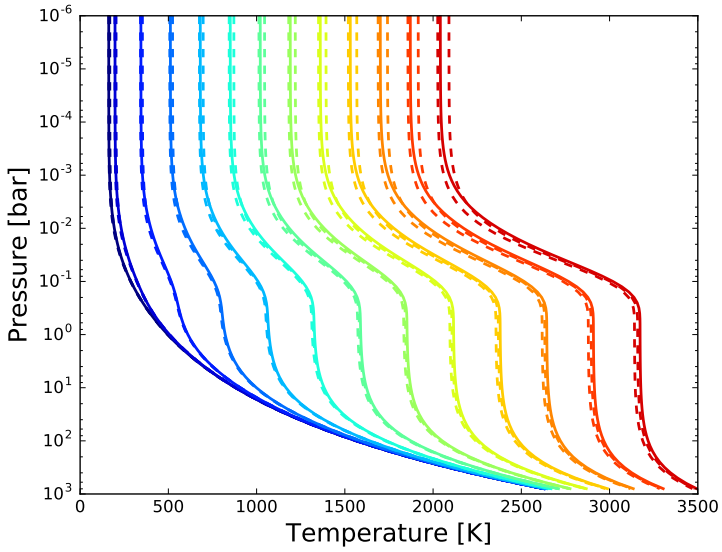

Figure 6.7: Validation of irradiated temperature profiles derived from the ScCHIMERA numerical radiative-equilibrium solver (solid) against double-gray analytic solutions (dashed; from Guillot 2010). Analytic solutions for two different values of the radiative diffusivity are shown (e.g., Parmentier et al. 2013) and bracket the numerical solution which is exact in the limit of no-scattering (Toon et al. 1989). The model set up here is for a gravity of 10 m/s^2, an internal temperature of 200 K, an infrared gray opacity of 0.3 m^2/kg, a gray visible-to-infrared opacity ratio of 5×10^{-3}, and a range of irradiation temperatures from 0 - 2300 K in steps of 200 K. The numerical solution agrees with the analytic solutions to better than 3% at all layers.

given the Lodders et al. (2003) abundances scaled via a metallicity and C/O ratio parameter (as in Molliere et al. 2015). The radiative-convective numerical scheme is implemented in pure Python (with k-table T-P interpolation in C) using the anaconda numba package for added acceleration. Validation of the numerical implementation of the radiative-equilibrium solver against analytic solutions is shown in Figure 6.7 and validation of the the opacity treatment against a brown dwarf grid model from Saumon & Marley (2008) is shown in Figure 6.8. Differences in all validation cases are less than 5%.

For the following cross-correlation analysis, we use a grid of ScCHIMERA planetary model spectra using the line-by-line version of the opacities given the converged T-P profile and thermochemical equilibrium molecular abundances. These spectra have resolution R = 500,000 and are calculated on the grid defined by metallicity log z = -1.0 - 2.0 in steps of 0.5, carbon-to-oxygen ratio C/O = 0.25 - 1.0 in steps

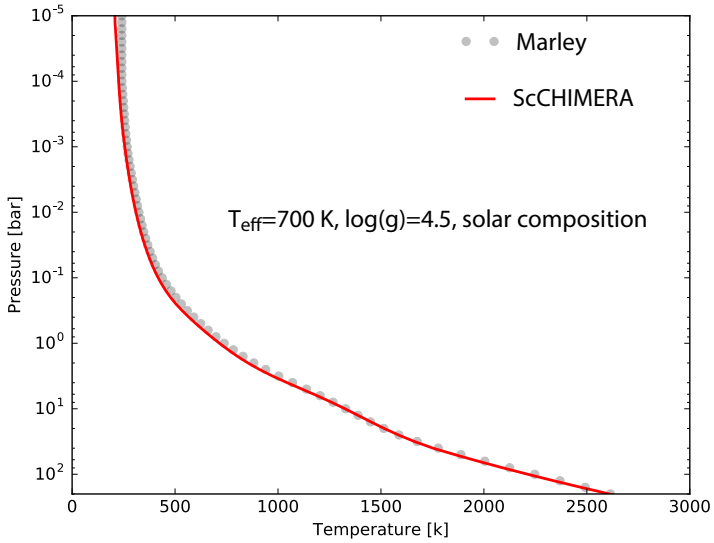

Figure 6.8: Validation of a non-irradiated temperature profile using the Sc-CHIMERA (solid) correlated-K "resort-rebin" opacity implementation against a Saumon & Marley (2008) grid model (dot) for a 700 K, $\log g = 4.5$ (cgs) brown dwarf. Agreement is better than 5%.

of 0.25, and stellar flux scaling f = 0.5 - 2.0 in steps of 0.25. Stellar flux scaling is a rough measure of energy redistribution. For $f \gtrsim 1.5$, the model atmosphere shows a temperature inversion. For the relevant regions of the grid, H_2O is the only significant L band opacity source, and no model spectrum is consistent with a blackbody.

6.5 NIRSPEC Data Analysis and Results

Two-Dimensional Cross Correlation

We measure the stellar and planetary velocity for each epoch of data with a two-dimensional cross correlation analysis (TODCOR), according to Zucker & Mazeh (1994), and with associated PHOENIX stellar and ScCHIMERA planet models. We use PHOENIX stellar model spectra based on the effective temperature, surface gravity, and metallicity of KELT-2A listed in Table 6.1 (Husser et al. 2013). All models are rotationally and instrumentally broadened before proceeding with the cross-correlation analysis.

For each ScChimera model, TODCOR produces a matrix of correlation values for various stellar and planetary velocity shifts. We combine the correlation functions for the orders of a single epoch and calculate a nightly maximum likelihood curve

for the star's and planet's velocities. An example of the resulting likelihood curves for three sets of cross-correlations (each with a best-fitting ScCHIMERA model) is shown Figure 6.9. With the PHOENIX model, we detect the star's velocity at a combination of the systemic velocity and the barycentric velocity, as expected (see Panel A of Figure 6.9). This technique is not sensitive to the reflex motion of the star, which is below the velocity precision of NIRSPEC.

Planet Mass and Orbital Solution

However, for a single epoch, we are unable to reliably identify the planet's velocity based on its nightly maximum likelihood curve (see Panels B-G of Figure 6.9). To retrieve an estimate of the line-of-sight Keplerian velocity, we must combine the nightly likelihood curves into a single, multi-epoch likelihood curve (Lockwood et al. 2014). Our equation for orbital velocity assumes a circular orbit, as is likely the case for KELT-2Ab (Beatty et al. 2012):

$$v_{sec}(M) = -K_p \sin(2\pi M) + \gamma \tag{6.1}$$

reproduced from Equation 3.39. Here, v_{sec} is the planet's velocity shift, M is the mean anomaly of the observation epoch ($M = 0$ at transit), and γ is a combination of the systemic and barycentric velocities. We test a range of K_P values from -250 to 250 km/s in order to create a final maximum likelihood curve for each ScCHIMERA model as shown in Figure 6.10.

For all ScCHIMERA models, we are able to detect the planet's velocity at 150 km/s. The line-of-sight Keplerian velocity of KELT-2Ab is 145^{+9}_{-8} km/s based on the transit method (Beatty et al. 2012). Our NIRSPEC measurement of the planet's velocity lies comfortably within this range.

We calculate error bars on our measurement of K_P with jackknife sampling. We remove one night's worth of NIRSPEC data, recalculate the maximum likelihood curve, and repeat, resulting in six maximum likelihood curves. The error bars for each value of K_P are directly related to the standard deviation of the six maximum likelihood curves as a function of K_P. These error bars are shown as grey shading in Figure 6.10.

With these error bars, we fit a Gaussian to the peak at 150 km/s, resulting in a K_P measurement of 148 ± 7 km/s. This corresponds to a mass of 1.5 ± 0.1 M_J and an orbital inclination of $79^{+11}_{-9}{}^{\circ}$. Based on this value of K_P, we mark the expected v_{sec} for each observational epoch in Panels B-G of Figure 6.9.

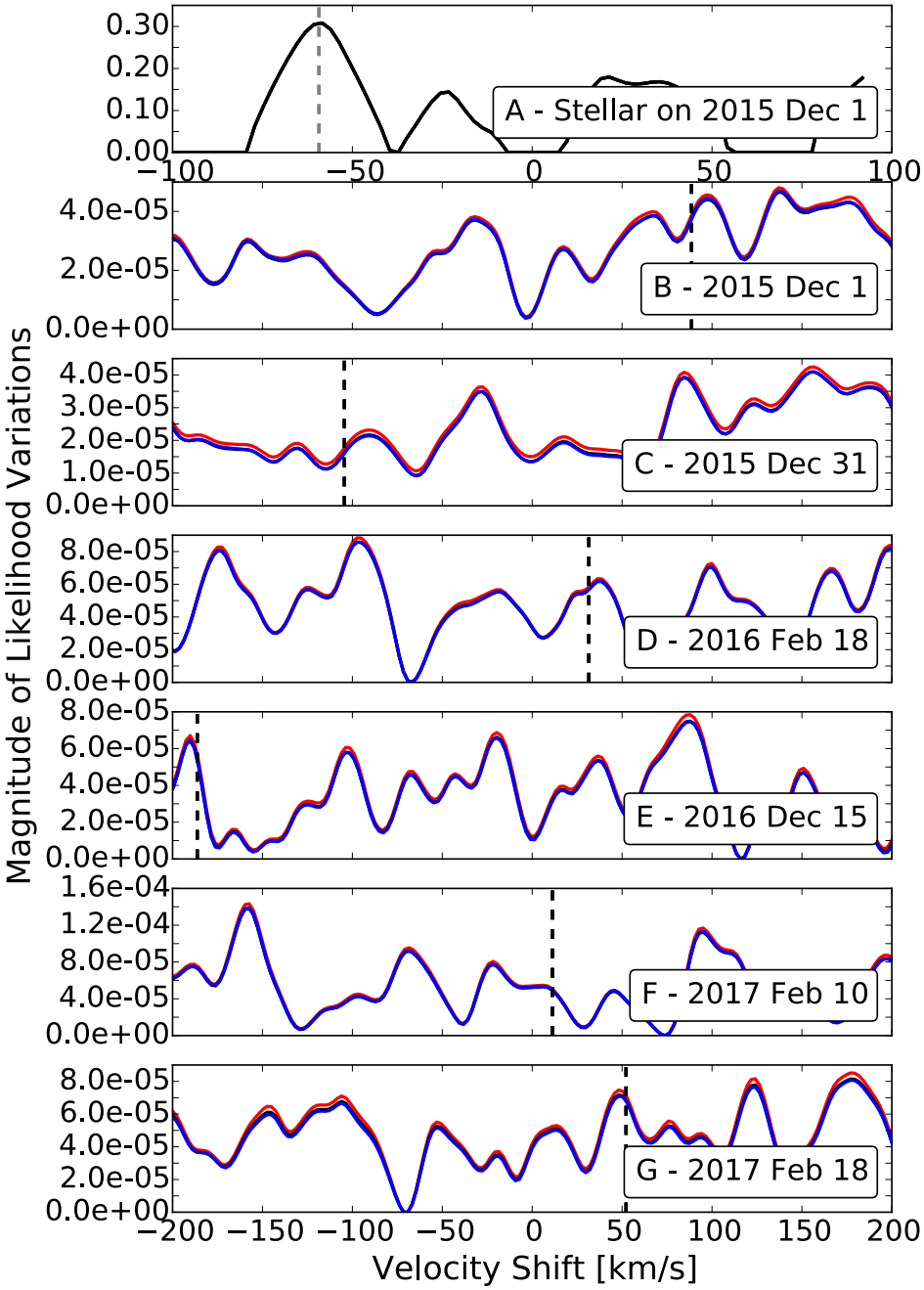

Figure 6.9: Maximum likelihood functions for all epochs of L band data. (A) Maximum likelihood function for the stellar velocity shift on 2015 December 1. (B-G) Maximum likelihood function for the planetary velocity shift. The grey and black vertical lines represent the expected values of v_{pri} and v_{sec}, respectively (based on the barycentric and systemic velocities and the line-of sight Keplerian velocity determined in Section 6.5). The red, black, and blue curves represent the correlation with the NIRSPEC-only best-fit, Spitzer-only best-fit, and NIRSPEC+Spitzer best-fit planet models, respectively.

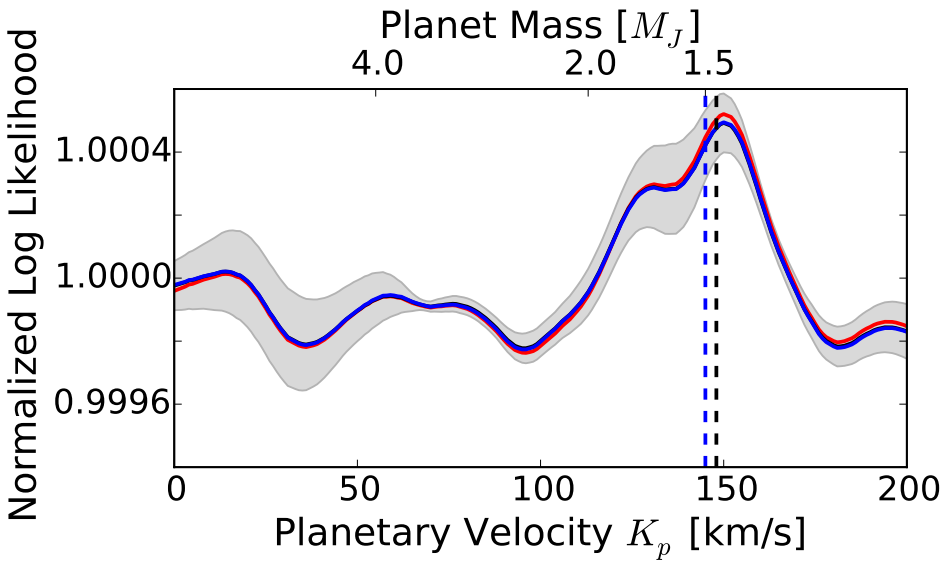

Figure 6.10: Normalized log likelihood as a function of Keplerian orbital velocity K_P. Likelihood curves resulting from correlating NIRSPEC data with the NIRSPEC-only best-fit, Spitzer-only best-fit, and NIRSPEC+Spitzer best-fit planet models for KELT-2Ab in red, black, and blue, respectively. The grey shading represents the jackknifed error bars and the vertical dashed black line represents the detection of the planet's velocity at 148 ± 7 km/s. The vertical blue dashed line represents the measurements made by Beatty et al. (2012).

We determine the significance of the detection by comparing the likelihood of a Gaussian fit (indicating a planetary signal) and a linear fit (indicating no planetary signal) to the likelihood peak at 148 km/s. We calculate the Bayes factor B as the ratio of likelihoods for the two fits. If $2\ln B$ is greater than ten, then the Gaussian fit is strongly preferred.

Using the jackknifed error bars, we find that $2\ln B$ is 11.6, suggesting that the planet detection is made at 3.8σ (Kass & Raftery 1995). For sufficiently deep integrations, this significance is determined by structure in the cross-correlation space and not by the aggregate shot noise.

NIRSPEC Constraints on KELT-2Ab's Atmosphere

At L band wavelengths, the planet model is dominated by water vapor and the source of the correlation signal presented here is water. Therefore, our NIRSPEC L band data allows us to report the presence of water vapor in the atmosphere of KELT-2Ab at 3.8σ.

For each ScCHIMERA grid point, we record the unnormalized maximum value of

Data Set	Parameter	16% CI	50% CI	84% CI	Best-fit
Spitzer,	$\log z$	-0.10	1.05	1.73	1.536
alone	C/O	0.34	0.53	0.74	0.403
	f	0.87	0.97	1.08	1.060
Spitzer with	$\log z$	-0.11	1.06	1.73	1.538
NIRSPEC	C/O	0.34	0.53	0.74	0.501
prior	f	0.87	0.97	1.08	1.060

Table 6.4: Best-Fit Values and Confidence Intervals for KELT-2A b Atmospheric Measurements

the maximum likelihood curve at K_P = 150 km/s. To get an idea of the underlying structure of our calculated maximum likelihood grid, we marginalize the grid along each axis (Figure 6.11). The NIRSPEC data alone has preference for high metallicity, C/O < 0.75, and low redistribution values. Specifically, the ScCHIMERA model that best fits the NIRSPEC data has $\log z$ = 1.5, C/O = 0.5, and f = 1.0. In Section 6.6, we use the grid of maximum likelihood values as a prior on the broadband Spitzer analysis of KELT-2Ab.

6.6 Joint Spitzer and NIRSPEC Constraints on KELT-2Ab's Atmosphere

Next we turn to the Spitzer secondary eclipse data introduced in Section 6.2 to further investigate KELT-2Ab's atmosphere.

We use the ScCHIMERA model grid for KELT-2Ab discussed in Section 6.5 at a resolution R=100 to fit the Spitzer transit depths. We use the Markov-Chain Monte Carlo technique implemented in `emcee` (Foreman-Mackey 2013). The likelihood function is

$$L = \exp\left(\frac{-(t_{obs} - t_{mod})^2}{2\sigma^2}\right), \tag{6.2}$$

where t_{obs} is the observed transit depths, t_{mod} is the transit depths of the model integrated over the Spitzer filters, and σ is the error on the observed transit depth. Confined to the model grid, we initialize 50 chains, perform a burn-in of 2000 steps, and run each chain for an additional 10,000 steps.

We run this MCMC analysis twice: once with a uniform prior and once with a prior informed by the NIRSPEC cross-correlation analysis in Section 6.5, resulting in the corner plot shown in Figure 6.12 (Foreman-Mackey 2016). The best fit values and confidence intervals for both versions of the data fits are given in Table 6.4.

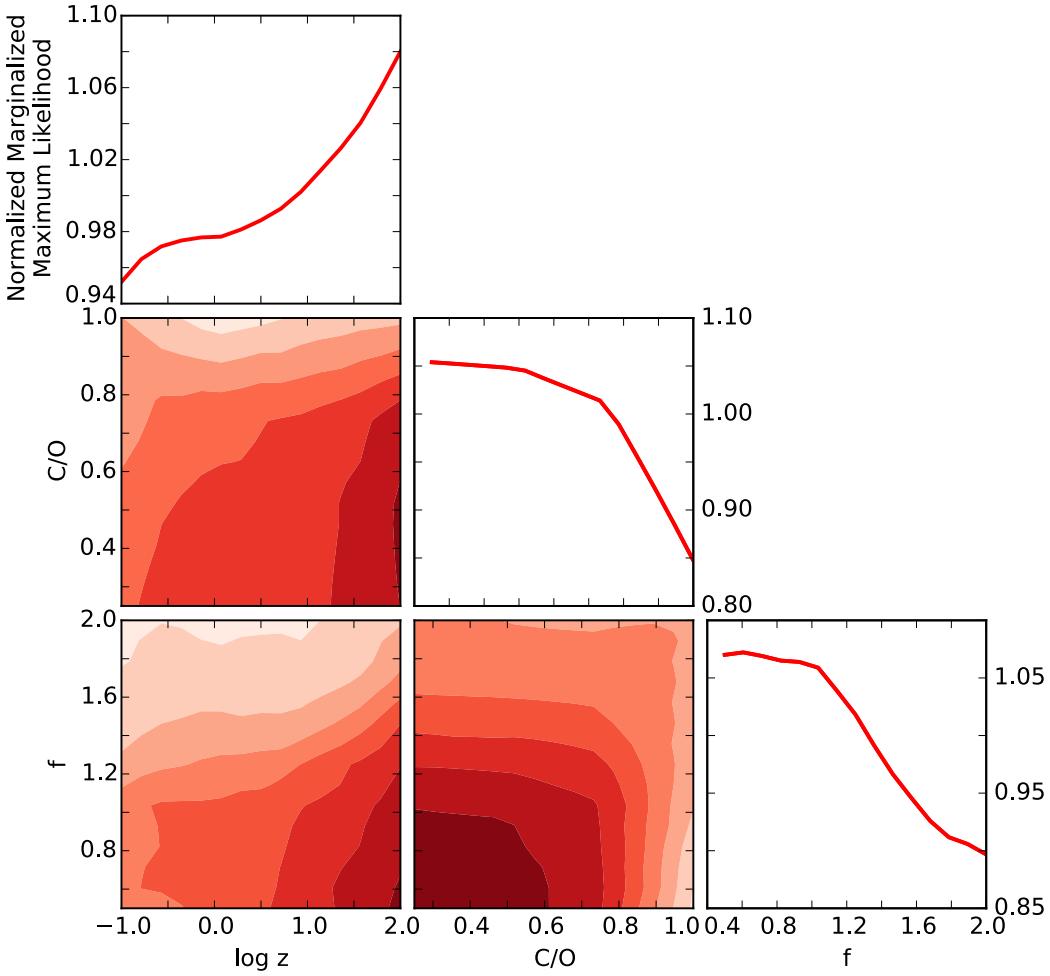

Figure 6.11: NIRSPEC-only atmospheric fits results. The marginalized grid of ScCHIMERA models cross-correlated with NIRSPEC data is shown with regions of darker red indicating a higher likelihood. The line plots are the marginalized, normalized likelihood values for each parameter. The grid of likelihoods serves as the NIRSPEC-informed prior applied to the Spitzer MCMC analysis.

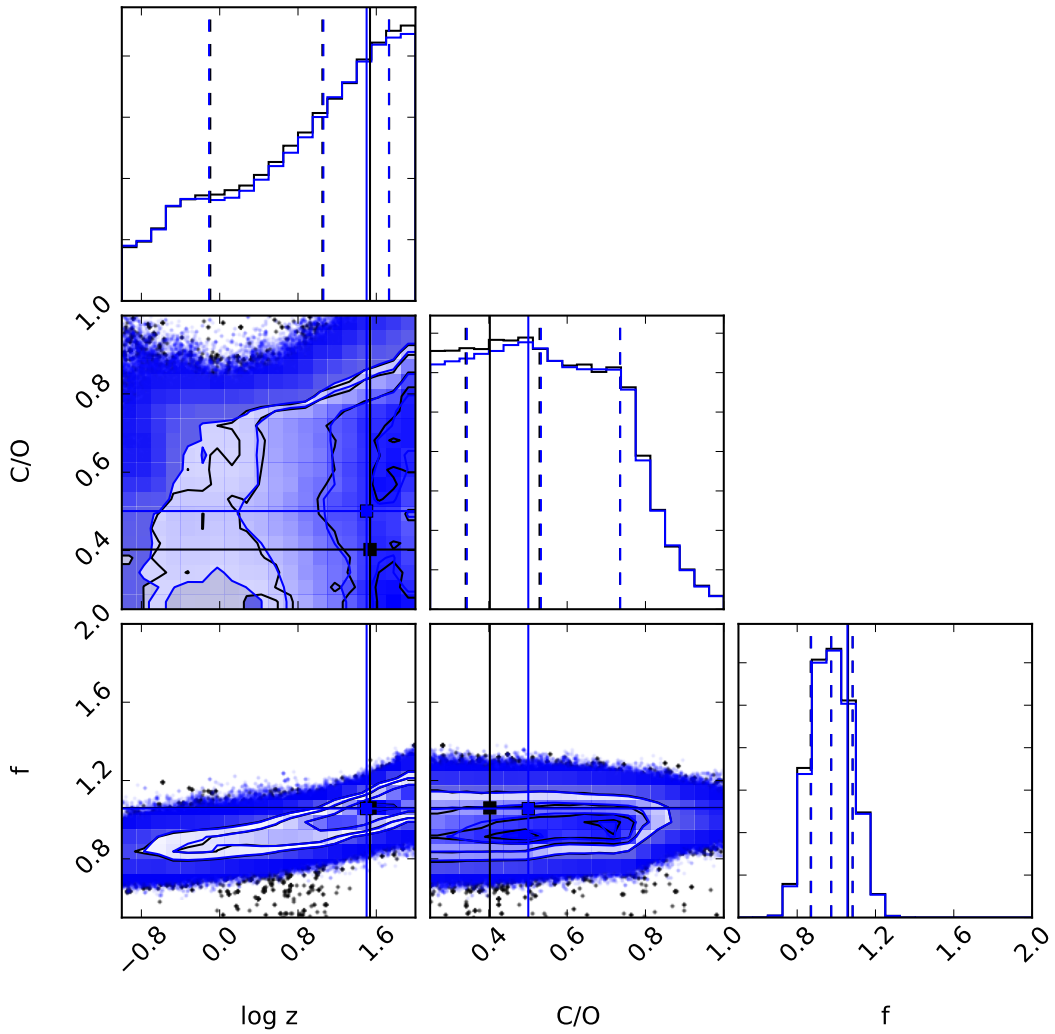

Figure 6.12: Comparison of Spitzer-only and combined Spitzer-NIRSPEC atmospheric fits results. Black shows the results of an MCMC analysis of the Spitzer IRAC data points when fit with the ScCHIMERA models and a uniform prior. Blue shows the results of an MCMC analysis of the Spitzer IRAC data points when fit with the ScCHIMERA models and a NIRSPEC-informed prior (which is essentially the likelihood grid illustrated in Figure 6.11). Points are the best-fit models and the dashed lines are the 16, 50, and 84% confidence intervals for each analysis.

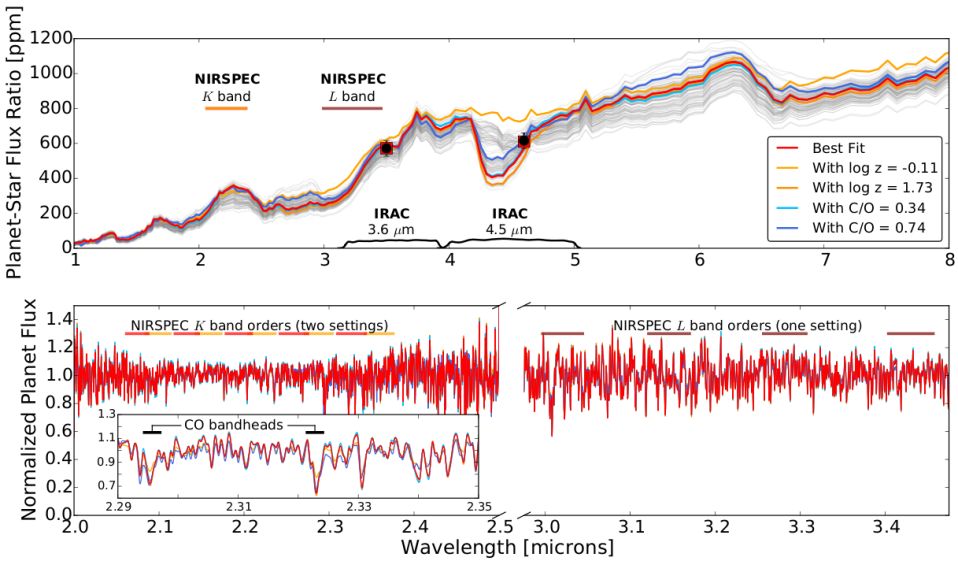

Figure 6.13: Model spectra plotted at probed wavelengths. Colored model spectra represent the best-fit spectrum based on the NIRSPEC-informed Spitzer MCMC analysis, and spectra generated at the 16 and 84% confidence intervals for metallicity and C/O. In the top panel, grey models represent random draws from the MCMC posterior. The Spitzer measurements and the Spitzer IRAC bandpasses are shown in black and the band-integrated best fit model fluxes are shown as red squares. The wavelength ranges of the NIRSPEC *L* and *K* bands are shown as well. The lower panel shows model planet spectra at NIRSPEC instrument resolution in the *L* and *K* bands. The *L* band wavelength ranges observed, *K* band wavelength ranges observed in Piskorz et al. (2017), and CO bandheads are indicated with horizontal bars. The inset shows a wavelength region where absorption is due to CO. All other absorption is due to H_2O.

6.7 Discussion

The shape of the NIRSPEC prior (Figure 6.11) largely matches the shape of the uniform-prior MCMC fit to the Spitzer data (black curves in Figure 6.12). Both data sets examined with uniform priors show preference for high metallicity and medium C/O ratios. The main difference in information content provided by the NIRSPEC and Spitzer data sets is at low values of redistribution. Figure 6.13 shows the Spitzer measurements and best-fit low- and high-resolution models at the Spitzer and NIRSPEC wavelengths investigated.

The lack of constraint on C/O is due to the opacity sources at the observed wavelengths: NIRSPEC data is dominated by water vapor and Spitzer by water vapor, CO, and CO_2. Neither data set on its own can constrain C/O and the application of the NIRSPEC-prior to the Spitzer analysis can provide no further constraint. How-

ever the strong disagreement with models having C/O = 1 emphasizes the detection of water vapor.

We find that our three model parameters are uncorrelated, except for $\log z$ and f at high metallicity. This might result from the fact that as metallicity increases CO and CO_2 abundances increase, creating more absorption at 4.5 μm. Then, to accommodate the larger eclipse depth, the temperature of the atmosphere has to increase, which is essentially an increase in redistribution f.

This analysis is only for clear atmospheric models produced by the ScCHIMERA framework. We do not attempt to study clouds or hazes; this would likely require high precision data from the near-UV to mid-IR to constrain well. Thus, we are not looking at variations in the temperature profile versus molecular abundances. The lapse rate (and therefore atmospheric composition, once C/O is set) is determined by the clear atmosphere assumption and stellar spectrum/orbital distance, and not varied.

When Spitzer photometry is already in hand, L band observations provide little new information. However, it is the case that Spitzer and NIRSPEC measurements can provide the same information independently. This implies that multi-epoch NIRSPEC data of non-transiting planets is roughly equivalent to Spitzer data. With a grid of self-consistent atmospheric models and multi-epoch NIRSPEC data sets on non-transiting hot Jupiters, we may begin to constrain their line-of-sight orbital velocities, masses, inclinations, and atmospheres more rigorously than in Piskorz et al. (2016, 2017).

There are two scenarios where NIRSPEC data may be able to provide more constraints on a hot Jupiter's atmosphere, both independently of and in tandem with Spitzer data. First, a NIRSPEC data set produced at higher signal-to-noise may provide better statistical measurements of the atmosphere's constituents. Second, a NIRSPEC data set in the K band would encompass emission by carbon monoxide in the planet's atmosphere, potentially tightly pinning down the carbon-to-oxygen ratio. (See the high-resolution K band models shown in the bottom panel of Figure 6.13.) Some of the strongest CO features are near 4.6 - 5 μm as well as 2.3 - 2.5 μm (fundamental and overtone, respectively), and so observations at the K and/or M bands are needed to get better C/O constraints. The best observing wavelength would depend on the temperature of the planetary atmosphere. For hot Jupiters, K band data should suffice, but for more distant planets (where the multi-epoch method still works) observations of the fundamental in M band will likely be better.

6.8 Conclusion

We report the ground-based detection the thermal emission of the transiting exoplanet KELT-2Ab's by measuring the planet's Doppler shift at various orbital phases. We measure K_P = 148 ± 7 km/s and report the presence of water vapor in its atmosphere. The agreement of this measurement with transit and radial velocity measurements reinforces the conclusions from previous detections (e.g., Lockwood et al. (2014), Piskorz et al. (2016, 2017), etc.) regarding the utility of the cross-correlation technique. Rigorous exploration of the phase space near K_P = 148 km/s with a suite of planetary atmospheric spectra determines the atmospheric properties required to satisfy both the Spitzer and NIRSPEC data. In the future, we will observe this planet in the K and M bands at high resolution. The combination of ground-based data with space-based data will hopefully provide new constraints on the C/O ratio of the planet's atmosphere and provide additional insight into the planet's formation history.

6.9 References

Amundsen, D.S., Tremblin, P., Manners, J. et al. 2017, A&A, 598,A97

Batygin, K., Bodenheimer, P.H., & Laughlin, G.P. 2016

Beatty, T.G., Pepper, J., Siverd, R.J., et al. 2012, ApJL, 756, L39

Benneke, B. 2015, arXiv:1504.07655

Birkby, J. L., de Kok, R. J., & Brogi, M. et al. 2017, AJ, 153, 3

Boogert, A. C. A., Blake, G. A., & Tielens, A. G. G. M. 2002, ApJ, 577, 271

Borysow, A. 2002, A&A, 390, 4

Brogi, M., Snellen, I.A.G., de Kok, R.J., et al. 2012, Nature, 486, 502

Brogi, M., de Kok, R.J., Albrecht, S. et al. 2016, ApJ, 817, 2

Brogi, M., Line, M., Bean, J., et al. 2017, ApJL, 839, L2

Burrows, A., & Volobuyev, M. 2003, ApJ, 583, 985

Cutri R. M., Skrutskie, M. F., van Dyk, S. et al., 2003, VizieR Online Data Catalog

Deming, D., Knutson, H., Kammer, J. et al. 2015 ApJ, 805, 2

Esteves, L.J., de Mooij, E.J.W., Jayawardhana, R. et al. 2017, AJ, 153, 168

Fazio, G. G., Hora, J.L., Allen, L.E. et al. 2004, ApJS, 154, 10

Foreman-Mackey, D., Hogg, D.W., Lang, D., $ Goodman, J. 2013, PASP, 125, 925

Foreman-Mackey, D. 2016, JOSS, 24, DOI:10.21105/joss.00024

Freedman, R. S., Marley, M. S., Lodders, K. 2008, ApJS, 174, 504

Freedman, R. S., Lustig-Yaeger, J., Fortney, J. J., et al. 2014, ApJS, 214, 25

Gontcharov, G.A. 2006, AL, 32, 11

Gordon, S. & McBride, B. J. 1994, NASRP, 1311

Guillot, T. 2010, A&A, 520, A27

Husser, T.-O., Wende-von Berg, S., Dreizler, S., et al. 2013, A&A, 553, A6

Kammer, J.A., Knutson, H.A., Line, M.R. et al. 2015, ApJ 810, 2

Kass, R.E., & Raftery, A.E. 1995, JASA, 90,773

Knutson, H.A., Charbonneau, D., Allen, L.E., et al. 2008, ApJ, 673, 1

Knutson, H.A., Lewis, N., Fortney, J.L., et al. 2012, ApJ, 754, 1

Kreidberg, L. 2015, PASP, 127, 1161

Lacis, A.A. & Oinas, V. 1991, JGR-Atmospheres, 96, D5

Lewis, N.K., Knutson, H.A., Showman, A.P. et al. 2013, ApJ, 766, 2

Line, M.R., Wolf, A.S., Zhang, X., et al. 2013, ApJ, 775, 2

Lockwood, A.C., Johnson, J.A., Bender, C.F., et al. 2014, ApJ, 783, L29

Lodders, K. 2003. ApJ, 591, 2

Madhusudhan, N., Knutson, H.A., Fortney, J.J., & Barman, T. 2012, Exoplanetary atmospheres. In *Protostars and Planets VI* (H. Beuther et al., eds.), pp. 739-762. Univ. of Arizona, Tuscon.

Martins, J.H.C., Santos, N.C., Figueira, P., et al. 2015, A&A, 576, A134

McLean, I. S., Becklin, E. E., Bendiksen, O., et al. 1998, Proc. SPIE 3354, 566

McKay, C.P., Pollack, J.B., & Courtin, R.1989, Icarus, 80, 23

Molliere, P., van Boekel, R., Dullemond, et al. 2015 ApJ, 813, 47

Morley, C.V., Knutson, H.A., Line, M.R. et al. 2017, 153, 2

Oberg, K.I., Murray-Clay, R., & Bergin, E.A. 2011, ApJ, 743,1

Parmentier, V., Showman, A.P., & Lian, Y. 2013, A&A, 558, A91

Piskorz, D., Benneke, B., Crockett, N.C. et al. 2016, ApJ, 832, 2

Piskorz, D., Benneke, B., Crockett, N.C. et al. 2017, AJ, 154, 2

Piskunov, N. E., Kupka, F., Ryabchikova, T. A., Weiss, W. W., & Jeffery, C. S. 1995, A&A S, 112, 525

Rothman, L.S., Gordon, I.E., Barbe, A., et al. 2009, J. Quant. Spectrosc. Radiat. Transfer, 110, 533

Saumon, D.& Marley, M.A. 2008, ApJ, 689, 2

Sing D. K., Fortney J. J., Nikolov N. et al. 2016, Nature, 529, 59

Snellen, I. A.G., de Kok, R. J., de Mooij, E. J. W., & Albrecht, S. 2010, Nature, 465, 1049

Tennyson, J., & Yurchenko, S. N. 2012, MRNAS, 425, 21

Toon, O.B., McKay, C.P., Ackerman, T.P., & Santhanam, K. 1989, JGR-Atmospheres, 94, D13

Valenti, J. A., Butler, R. P., & Marcy, G. W. 1995, PASP, 107, 966

Werner, M. W., Roellig, T.L., Low, F.J. et al. 2004, ApJS, 154, 1

Wollert, M. & Brandner, W. 2015, A&A, 579, A129

Wu, Y., & Murray, N. 2003, ApJ, 589, 605

Zucker, S. & Mazeh, T. 1994, ApJ, 420, 806

Chapter 7

SUMMARY AND FUTURE WORK

7.1 Summary

In Chapter 2, we detailed our search for cool, stellar companions to hot Jupiter host stars with near-infrared spectra. Our goal was to determine the stellar multiplicity rate of hot Jupiter systems and to shed light on the dominant migration mechanism in those systems. We learned that there was little difference in the observed multiplicity rate of aligned and misaligned hot Jupiter systems, indicating that three-body dynamics are not wholly responsible for the migration of hot Jupiters. However, we also concluded that the stellar multiplicity rate for hot Jupiter systems was higher than for field stars, suggesting that the presence of a binary companion may aid the formation of a hot Jupiter. This method was also shown to be sensitive to spots on the surface of the host star.

In Chapter 3, we motivated and described our pipeline designed to detect the Doppler shift of a planet's spectrum buried within its star's spectrum, including the integration of principal component analysis into the pipeline. In Chapters 4-6, we applied these methods to four hot Jupiters, learning their masses, orbital inclinations, and atmospheric opacities in the infrared. We confirmed the earlier NIRSPEC detection of tau Boo b's atmosphere with the updated pipeline. The atmosphere of HD 88133 b was the first to be detected with NIRSPEC data in both the L and K bands. The detection of ups And b's atmosphere provided the opportunity to uniquely characterize the orbital elements of each planet in the multi-planet system, allowing dynamicists to explore the system's origin and stability. KELT-2Ab is a transiting planet and the detection of its atmosphere with NIRSPEC was paired with Spitzer secondary eclipse data to confirm the pipeline's fidelity and to place constraints on the planet's atmospheric composition.

These two projects not only endeavour to illuminate the circumstances of hot Jupiters but also to distinguish signal from noise. In the Friends of Hot Jupiters project, the desired signal was from a hidden binary companion buried in stellar noise down to 10^{-2}. In the Direct Detection project, the desired signal was from a hot Jupiter buried in stellar noise down to 10^{-5}. Both projects battled instrument noise, photon noise, and telluric contamination. The different desired signal strengths for the two

projects proscribed the observing strategy and the telluric removal procedure. For the Friends of Hot Jupiters project, a fifteen to thirty minute integration per target was adequate. Telluric removal by dividing the target spectrum by a calibrator A star spectrum was effective. In contrast, for the Direct Detection project, to confidently acquire the hot Jupiter signal, many hours of integration per target over many nights was required. Telluric removal was performed with a model-guided principal component analysis. These observing strategies and data reduction techniques pave the way for future ground-based investigation of exoplanets, made more promising by an upgraded NIRSPEC instrument at Keck Observatory.

7.2 Capabilities enabled by the NIRSPEC upgrade

The NIRSPEC instrument will be taken off the Keck II Telescope in mid-2018 and reinstalled approximately six months later. There are three main aspects of the NIRSPEC upgrade, detailed in Martin et al. (2014).

First, the science detector will be replaced and will have higher throughput, smaller pixels, larger array size, and fewer hot pixels. In all, this results in higher instrument resolution and shorter integration times to reach a given photon count with better spectral sampling over a larger spectral range. Better sampling means longer target integration times before reaching the background limit.

Second, the slit-viewing camera will be replaced and will operate in the same wavelength range as the spectrometer camera. Currently, the slit-viewing camera is only sensitive to wavelengths out to the K band. Observations in other bands requires switching filters to the K band to ensure that the target is on the slit. This decreases observing efficiency by about 50%.

Third, the readout control and electronics will be replaced. The upgraded system will have less readout and systematic noise. The control hardware will be consistent with other infrared instruments on Keck (MOSFIRE, OSIRIS) and will be able to be more easily repaired.

The improvements in efficiency and resolution are beneficial to both projects described in this thesis. Both projects benefit from deeper observations at higher resolution. Especially for the direct detection project, higher throughput means two or three hour-long observations become one hour observations per target. High resolution means more spectral lines can be accessed, enhancing our ability to detect faint cool star or planet lines. The ability to observe targets in M band allows observers to take advantage of the higher photometric contrast between planet (or cool

star) and host star. For the direct detection, *M* band observations allow the detection of carbon monoxide and water vapor in a hot Jupiter's atmosphere simultaneously.

These capabilities, especially when paired with space-based capabilities (be they on the Hubble Space Telescope, the Spitzer Space telescope, or the James Webb Space Telescope), provide a great opportunity to study the spectra of distant worlds. Other upcoming spectrometers with enhanced capabilities include CRIRES+, ESPRESSO, SPIRou, and CARMENES (Oliva et al. 2014; Mégevand et al., 2014; Artigau et al., 2014; Quirrenbach et al., 2014). At Keck Observatory, the combination of adaptive optics, the new *L* band vortex coronagraph, and the upgraded NIRSPEC would provide an unprecedented capability to measure the spectra of cool companions and exoplanets (Mawet et al. 2017).

7.3 Continuing the search for companions to hot Jupiter hosts

The spectroscopic model comparison method described in Chapter 2 served to explore a region of semi-major axis space previously inaccessible to traditional radial velocity and adaptive optics techniques. In the past few years, long-term radial velocity observations have increased their observation baselines, allowing for more distant companions to hot Jupiters hosts to be uncovered. Direct imaging has capitalized on angular differential imaging and coronagraphs with small inner working angles to uncover companions at small projected separations. Examples of these efforts include Bryan et al. (2016) and Ngo et al. (2016).

Through the detection of new stellar companions, these works, in addition to that discussed in Chapter 2, have provided many illustrative conclusions and questions about the migration of hot Jupiters. Only about 20% of the stellar companions detected in Ngo et al. (2016) are capable of causing Kozai-Lidov migration. Between 50 and 2000 AU, hot Jupiters tend to have three times as many companions than field stars, but between 1-50 AU hot Jupiters lack companions. This suggests that there is *some* correlation between stellar multiplicty rates and hot Jupiter occurrence rates. Bryan et al. (2016) found that hot Jupiters with planetary companions have higher average eccentricities than single planet systems, suggesting that three-body dynamics (which pumps eccentricities) may have played a role in hot Jupiter migration.

In addition, the dispostive null detections listed in Table 2.2 play an important role in future transit and transit spectroscopy measurements of hot Jupiters. For example, the confirmation of clouds and hazes in the atmosphere of HAT-P-32b with the

Large Binocular Telescope was in part made possible by the disallowing of a stellar companion at cool temperatures in the system (Mallonn & Strassmeier, 2016).

7.4 Continuing exploration of exoplanetary atmospheres

As illustrated in Table 3.1, the arena of studying planetary atmospheres from the ground is burgeoning. Pending tasks for the direct detection of exoplanet atmospheres with current and future NIRSPEC data include:

- **Publication of remaining data sets,** including 51 Peg b, HD 187123 b, HD 102195 b, and HD 189733 b (transiting). A NIRSPEC study of 51 Peg b would be especially illuminating, as it would allow an opportunity to validate the CRIRES detection of water vapor in the planet's atmosphere (Birkby et al. 2017).

- **Optimization of experimental setup and observing strategy**, similar to the work done by deKok et al. (2014) for the CRIRES instrument. Such an analysis would aid in preparing for observations with the upgraded NIRSPEC instrument. It would also reveal ideal echelle and cross-disperser settings that would encompasses the most information on the planet's atmosphere. This analysis also involves modeling Doppler shifts at various orbital phases to ensure that relevant planet lines are not engulfed in stellar or telluric features. It is likely this analysis (as well as the NIRSPEC upgrade) will motivate observing hot Jupiters and warm Neptunes in the *M* band where water vapor and carbon monoxide can be simultaneously targeted.

- **Combination of the cross-correlation algorithm with an atmosphere retrieval algorithm** similar to SCARLET (Benneke 2015) or ScCHIMERA (Chapter 6). This will allow the robust exploration of phase space near the peak of the planetary velocity maximum likelihood curve. In addition, such a union would provide the opportunity to more accurately determine water vapor and other molecular abundances.

- **Simultaneous analysis of ground- and space-based data.** We present the NIRSPEC and Spitzer infrared data for the hot Jupiter KELT-2Ab in Chapter 6 and suggest a preliminary method for combining the two datasets to measure the carbon-to-oxygen ratio and metallicity. A similar analysis for the hot Jupiter HD 209458 b was performed by Brogi et al. (2017). This work iteratively solved for the C/O ratio of the planet's atmosphere given CRIRES,

Hubble WFC3, and Spitzer IRAC data given the outputs of the CHIMERA emission forward model (Line et al. 2013).

- **Calculation of stellar spectra using a variation of principal component analysis.** With either a variation of PCA as presented in Chapter 3 or with spectral match filtering, it is possible to isolate the stellar signal and the components that vary with the stellar signal. This pursuit would eliminate the necessity of using theoretical stellar models from the PHOENIX stellar library. It would also produce stellar spectra with attributes not necessarily predicted by theory, such as star spots. As discussed in Chapter 2, star spots are prevalent on cooler stars, often contain water, and radiate at temperatures between 500 and 1000 K cooler than the star. Accurate models and interpretations of star spots are critical if we wish to be able to reliably detect water in the atmospheres of planets orbiting cooler stars (e.g., Proxima Centauri b in Anglada-Escudé et al. 2016 and the TRAPPIST-1 planets in Gillon et al. 2017).

  A simpler iteration of this task would be to generate a coadded stellar spectrum based on cleaned spectra shifted to the rest frame. This concept is similar to white light curves generated for transit studies and would yield a high S/N stellar spectrum. Such a spectrum would allow the measurement of stellar CH and OH lines and ultimately a calculation of stellar C/O.

- **Three-dimensional cross-correlation of NIRSPEC data with stellar, star spot, and planetary models.** This involves the combination of the star spot characterization aspect of the Friends of Hot Jupiters project with the TODCOR algorithm of the Direct Detection project. This would in effect result in a three-dimensional cross-correlation, where the three components are the stellar spectrum, the spectrum of the star spots (about 10^{-2} of the stellar signal), and the planetary spectrum (about 10^{-5} of the stellar signal). Many of the stars in our sample are hot and quickly rotating, making them unlikely to be active and have starspots. However, as discussed above, some of the most interesting targets for study orbit cooler, more slowly rotating stars, requiring a formalism for starspot contamination.

With the further refinement of this technique and implementation of next-generation spectrometers and coronagraphs, especially on the largest optical/infrared telescopes, we are optimistic that the direct detection method can be used to accurately

constrain the atmospheres (and therefore the formation) of hot Jupiters. The opportunity to combine high-dispersion spectroscopy with high-contrast imaging on large, ground-based telescope opens up many possibilities for future discoveries. For example, the European Extremely Large Telescope (E-ELT) in Chile has a 40-meter aperture, should see first light in 2024, and is planned to have a Mid-infrared E-ELT Imager and Spectrograph (METIS). METIS pairs extreme adaptive optics and a high resolution integral field spectrometer (R=100,000). With this configuration, it is possible to detect the atmosphere of a $1.5R_E$-sized planet with T_{eq}=300 K at 4.8 μm (Snellen et al. 2015). Such observations will need to adapt the multi-epoch approach adapted here.

It will not be long before the characterization of terrestrial atmospheres at Earth-like semi-major axes is a reality. Many new space-based mission are being revised and proposed for the 2020 Decadal Survey (Origins Space Telescope, LUVOIR, etc.) that will target the atmospheres of transiting planets, but telescopes on the ground will continue to provide avenues for the study of non-transiting planets.

7.5 References

Anglada-Escudé, G., Amado, P.J., Barnes, J. et al. 2016, Nature, 536, 437

Artigau, E., Kouach, D., Donati, J-F. et al. 2014, Proc. SPIE 9147

Benneke, B. 2015, arXiv:1504.07655

Birkby, J.L., de Kok, R.J., Brogi, M. et al. 2017, AJ, 153, 3

Brogi, M., Line, M.R., Bean, J.,et al. 2017, ApJL 839 L2

Bryan, M.L., Knutson, H.A., Howard, A.W., et al. 2016, ApJ, 821, 2

de Kok, R.J., Birkby, J., Brogi, M. et al. 2014, A&A 561, A150

Gillon, M., Triaud, A.H.M.J., Demory, B-O., et al. 2017, Nature, 542, 456

Line, M. R., Knutson, H., Deming, D., et al. 2013, ApJ, 778, 183

Mallonn, M. and Strassmeier, K.G. 2016, A&A, 590, A100

Martin, E.C., Fitzgerald, M.P., McLean, I.S. et al. 2014, Proc. SPIE 9147

Mawet, D., Ruane, G., Xuan, W et al. 2017, ApJ 838, 2

Mégevand, D., Zerbi, F.M., Di Marcantonio, P., et al. 2014 Proc. SPIE 9147

Ngo, H., Knutson, H.A., Hinkley, S., et al. 2016, ApJ, 827, 8

Oliva, E., Tozzi, A., Ferruzzi, D. et al. 2014, Proc. SPIE 9147

Quirrenbach, A., Amadob, P.J., Caballeroc, J.A., et al. 2014 Proc. SPIE 9147

Snellen, I., de Kok, R., Birkby, J.L., et al. 2015, A&A, 576, A59

Appendix A

NIRSPEC REDUCTION

This codebase was originally spearheaded by Klaus Pontoppidan and Nathan Crockett.

Locate raw fits files and logs

Data tends to be mounted on `viola.gps.caltech.edu:/Users/alock/Nirspec/Raw`. In order to be reduced, data is moved to `/home/gablakers/NirspecData`. Logs can be found at `/home/gablakers/NirspecLogs` or at the original google doc.

Set up initialization files

In the file named `nirspec_[date].ini`, copy the values for the filter, echelle, and cross-disperser from the logs and make sure they match the headers of the fits files. You can get good guesses for the minimum and maximum wavelengths, `wrange`, for each order by running `nirspec_simulate.pro` and inputting the echelle and cross-disperser positions for a given night. For the `yrange`, open the fits files for an A nod and a B nod in `ds9`. Choose minimum and maximum values for `yrange` such that both nods are fully included and such that the two nods are well-separated by the average value of `yrange`. For the first run through, leave the A, B, C coefficients for the wavelength solution as is.

Set up run file

The Python version of the reduction measures counts per pixel and fits a non-linear wavelength solution (unlike the IDL version, which used fixed lamp lines and linearly interpolated to find the wavelength solution). This version automatically fits the flux with a sky model to obtain a wavelength solution.

Run files are called `pl_[date].py`. Fill out the frame numbers for the flats, darks for flats, and science integrations. The darks for the observations are not important here. In the call to the reduction routine, input the name of the initialization file. `shift` is the number of pixels between science and standard before telluric division, `dtau` is change in optical depth to match standard to science target, and `holdplots` can be true or false. Set `holdplots` to `True` if you want the code to stop and wait

until you close the plot before continuing. Be sure the output folders are created before running the routine. For the exact flux count, normalize by exposure time and scale to the standard star.

Run all data at once to produce a single spectrum

In python, run `pl_[date].py`. Data is saved to the `WAVE` directory.

Calculate wavelength solution

The wavelength solution is calculated by `RunWaveCal.py`. The wavelength solution is more straightforward in L band than in K band. If you're reducing L band data, then import `WaveCal_orig_Lband.py`. If you're reducing K band data, then import `WaveCal_stelltell_Kband.py`. The K band version uses a more accurate telluric model for the night as well as a stellar model to help fit the lines.

In `RunWaveCal.py`, choose the band you're reducing. Write in the filepaths for the data you want to find the wavelength solutions for. If you're reducing K band data, input the v_{bary} on the night of the observation and the v_{rad} of the system. Confirm that the code is using the correct stellar model for the target.

In a python terminal, `run RunWaveCal.py`. This routine fits strongest telluric absorption lines (and stellar lines for K band data). Fit zero point (b) on the left and the linear term (m) on the right. Only try to fit the locations of the lines, the depths don't matter for this step. If you are having trouble, you can try changing between minimization routines ('powell' or 'least-sq') in the `FitDS` function (toward the end of `WaveCal_orig_Lband.py` and `WaveCal_stelltell_Kband.py`). Specifically, once `RunWaveCal.py` is running in Python, for each order of data the commands are as follows:

1. `pos`, b-value, m-value. Repeat until satisifed with fit.
2. `neg`, b-value, m-value. Repeat until satisfied with fit.
3. `fit`. Fits data with a least-squares minimization routine based on the most recent values of b and m for both positive (A) and negative (B) nods.
4. `pf` for print fit. Copy values for A, B, and C times 10^{-6} coefficients into NIRSPEC initilization file. Copy and save values for D and E as well for K band data.
5. `quit` to escape. Repeat on all orders of data.

Run data in AB pairs

In `pl_[date].py`, change the array of science integrations so that it reads ([A1, B1], [A2, B2], etc.). For *L* band data, the reduction pipeline will automatically refit the wavelength solution based on the first three coefficients. For *K* band data, hard code all five coefficients given by `RunWaveCal.py` and turn off the wavelength fitting function.

In python, run `pl_[date].py`. Data is saved to the `WAVE` directory.

Appendix B

TELLURIC REMOVAL WITH PRINCIPAL COMPONENT ANALYSIS

This code base was originally spearheaded by Nathan Crockett.

There are two versions of the principal component analysis (PCA) pipeline, one for *L* band data (`TelCorPCA_dp_fitmod.py`) and one for *K* band data (`TelCorPCA_dp_fitmod_K.py`).

The *L* band version uses the A,B, and C wavelength coefficients (copied from the initialization file used in the reduction) to fit for the wavelength solution.

The *K* band version uses the A, B, C, D, and E wavelength coefficients to recalculate the wavelength solution. There are also slight differences in how the telluric model is fit to the data.

Be sure to check and change all the directories where files are saved.

Set up run file

Run files contain relevant directories, frame numbers, initial guesses for telluric molecular abundances, etc., for each night and band of data reduced. Example run files are are `tc_08apr2015.py` (for *L* band data) and `tc_21nov2015.py` (for *K* band data).

Import either `TelCorPCA_dp_fitmod.py` for *L* band data and `TelCorPCA_dp_fitmod_K.py` for *K* band data. Check and change home, input data, and output data directories as needed. Write the frames numbers of the files you reduced as AB pairs. Fill out the section for the Calibrator Data, though it isn't used. The molecular abundance for the "Night Info" section either comes from online databases or best-fit to spectrum. Input radial and barycentric velocities for your system on the night that you observed. (These values are used for overplotting stellar spectrum in the final output.) Copy values from the NIRSPEC reduction initialization file into the `WaveArray` (`wavemin`, `wavemax`) and `WaveCalCoefsArray` (A, B, C for *L* and A, B, C, D, E for *K*). Note that a few old TERRASPEC files are pointed to in the "For TERRASPEC Comparison section." These are intended to help determine the quality of telluric removal with PCA.

Check time series of data

In `TelCorPCA_dp_fitmod.py` (for L or K), insert `assert(0==1)` statement after `self.CheckTimeSeries()` (around line 67).

In python, `run tc_08apr2015.py`.

Look at output of `CheckTimeSeries`. Pick out any spectra which are obviously wrong (unusual absorptions, erratic continua).

In `tc_08apr2015.py`, remove the AB pairs that don't match the others by deleting the relevant index from `good_order`.

Do this for each order of data.

Full run-through

In `TelCorPCA_dp_fitmod.py` (for L or K), remove `assert(0==1)` statement after `self.CheckTimeSeries()`(around line 67).

In python, run `tc_08apr2015.py`.. This routine will

1. Refit or recalculate the wavelength solution.
2. Use initial guesses for molecular abundances to fit atmospheric abundances.
3. Use fitted atmosphere to fit instrument profile.
4. Apply that instrument profile to the stellar model.
5. Shift stellar model to correct velocity in `RemoveStar`.
6. Use fitted atmosphere to guide the PCA analysis.
7. Pass PCA components back out to `tc_08apr2015.py`.
8. It is `tc_08apr2015.py` that removes the components from the data. The `for` loop goes through each order, runs PCA, then removes 0-15 components, removes 0, 5, 10, or 15 fringes and saves them to the current directory and to the cross-correlation directory. It also makes plots of the output (corrected spectra compared to models, corrected spectra stacked, components, percent variance removed).
9. Output is saved to your specific output directory.

Appendix C

TWO-DIMENSIONAL CROSS-CORRELATION

This code base was originally spearheaded by Chad Bender. The GUI has been cut out, and run files are substituted for it. Within the *Exoplanets* directory are the:

Routine directory: Contains `master.pro` and dependent routines. Contains folder (e.g., *HD88133_C5*) with reduced and cleaned data, stellar model, and planetary model. Output of `master.pro` is saved here.

and

Targets directory: Contains three run files (detailed below) with names matching the name of the folder containing the data.

Set up run file #1

This file is named, for example, `HD88133_C5.dat`.

This run file begins with the locations of the data and models. The first few (`n_order` x `n_nights`) lines are the filenames of the reduced spectra. The next line is the filename of the stellar model spectrum, and the next is the filename of the planetary model spectrum.

The file ends with inputs for the cross-correlation routine. The following line encodes the units of the data spectra, the stellar spectrum, and the planetary spectrum where `0` implies angstroms, `1` implies microns, and `2` implies wavenumbers. It is best to write the input files in wavenumbers. The next line is the lower and upper bounds on the velocity of the star in km/s (best to use -100 and 100). The penultimate line is the lower and upper bounds on the velocity of the planet in km/s (best to use -200 and 200, but can use larger bounds). The final line is two instances of the spectroscopic contrast α_{spec}.

Set up run file #2 with instrument profiles

This file is named, for example, `HD88133_C5_ip.dat`. The contents of this file comes from the instrumental profiles calculated for each order of data during the PCA step.

Matching the file list in the first run file, this file only contains `n_order` x `n_nights`

lines. Each line contains the width of the instrumental profile, locations of the four left satellite Gaussians, and locations of the four right satellite Gaussians. All units are in wavenumbers.

Set up run file #3 with information on the nights observed

This file is named, for example, `HD88133_C5_nights.dat`.

The information in this file is only used in the maximum likelihood calculation. If you like, you could hardcode and double-check the values in the maximum likelihood code (`max_like_auto.pro`) instead of using this file. Such a procedure would be especially effective if the planet is on an eccentric orbit and the relevant orbital parameter is the free anomaly, not the mean anomaly (see the next section).

The first line is the period of the planet's orbit. The next is the start time, or the time of periastron. The third line is the Julian date of each observation. Be sure the units of the second and third lines are equivalent. These lines are used to calculate the mean anomaly M. The value in the second line controls from where the mean anomaly is measured (i.e., where $M = 0$.)

The fourth line is the barycentric velocity at the time of each observation. The final line is the systemic velocity of the exoplanetary system.

Calculate and double check the observation phases

The python script `plotorbit_v3_streamlined.py` draws the planet's orbit and calculates the mean, eccentric, and free anomalies (in `free_rad_obs`). The free anomalies can be hardcoded into `max_like_auto.pro`.

Run cross-correlation routine

In IDL, `master, 'target', 'n_nights', 'n_orders'`.

The cross-correlation routine is broken into three steps. Double check all directories where files and plots are saved.

1. `sxcorr_calc2d.pro`:Cross-correlates stellar and planet spectra with each order of data on a given night

2. `mlcombine2d.pro`: Combines cross-correlation surfaces for all orders on a single night into a maximum likelihood plot for the velocities of the planet and star on a given night

3. `max_like_auto.pro` or `max_like_auto_ecc.pro`: Combines all maximum likelihood curves from all nights to determine the most likely orbital velocity for the planet